Turbulence Modelling of Unsteady Separated Flow over an Airfoil

by

Barton Thomas Stockdill
B.Eng., University of Victoria, 2001

A Thesis Submitted in Partial Fulfillment of the
Requirements for the Degree of
MASTER OF APPLIED SCIENCE
in the
Department of Mechanical Engineering.

University of Victoria

Supervisors: Dr. Nedjib Djilali, Dr. Afzal Suleman

Abstract

Turbulent flow simulations are carried out for a NACA 0012 airfoil in steady and unsteady cases. The objective is to assess the performance of the research code SPARC such that it may be used for more complicated fluid structure interaction and airfoil optimization problems. Steady simulations are performed from a zero angle of attack up to stall at a chord Reynolds number of 3×10^6 using the Spalart Allmaras one equation turbulence model and the Speziale $k-\tau$ two equation turbulence model. An extensive grid study shows that lift and drag predictions are very sensitive to the near wall resolution; wall functions are not used. Lift, pressure drag and friction drag results are found to be in good agreement with experimental data up until the stall. Steady state simulations did not converge in the stalled regime. Unsteady simulations are carried out at an angle of attack of 20 degrees and a chord Reynolds number of 10^5; the Reynolds number is lowered to keep the computational requirements reasonable. Though conventional aircraft operate at Reynolds numbers over 10^6, there is much interest in low Reynolds number (10^5) airfoil data for gliders and unmanned aircraft operating at very high altitudes. The Spalart Allmaras and Speziale models are used again, along with the adaptive $k-\tau$ model of Magagnato. While the Spalart Allmaras model did not yield any unsteady phenomena, the Speziale model yielded a periodic lift and drag signal. The adaptive model yielded a more complex and irregular signal but also gave the most realistic results.

Table of Contents

List of Tables

List of Figures

Nomenclature

α	Airfoil angle of attack $[deg]$
C_d	Coefficient of drag
C_{df}	Coefficient of friction drag
C_{dp}	Coefficient of pressure drag
C_f	Shear stress coefficient
C_l	Coefficient of lift
C_p	Coefficient of pressure
$\hat{i}$	Unit vector in x direction $[m]$
$\hat{j}$	Unit vector in y direction $[m]$
$\hat{k}$	Unit vector in z direction $[m]$
k	Turbulent kinetic energy $[J/kg]$
μ	Laminar viscosity $[kg/(ms)]$
μ_t	Eddy viscosity $[kg/(ms)]$
ν	Kinematic viscosity (μ/ρ)
ν_t	Kinematic eddy viscosity (μ_t/ρ)
P	Pressure $[N/m^2]$
Re_c	Airfoil Reynolds number based on chord length c [-]
ρ	Density $[kg/m^3]$
τ_{ij}	Reynolds stress tensor $[N/m^2]$
U_∞	Free stream velocity $[m/s]$
$\vec{U}$	Velocity vector $= u\hat{i} + v\hat{j} + w\hat{k}$
u	Component of velocity in the x direction $[m/s]$
v	Component of velocity in the y direction $[m/s]$
w	Component of velocity in the z direction $[m/s]$

Spallart Allmaras Model

C_{b1}	Constant = 0.1355
C_{b2}	Constant = 0.622
C_{t1}	Constant = 1
C_{t2}	Constant = 2
C_{t3}	Constant = 1.1
C_{t4}	Constant = 2
C_{w1}	Constant = $C_{b1}/\kappa^2 + (1 + C_{b2})/\sigma$
C_{w2}	Constant = 0.3
C_{w3}	Constant = 2
d	Distance to wall [m]
ΔU	Difference between velocity at field and trip points [m/s]
κ	Constant = 0.41
ω_t	Magnitude of vorticity at wall trip point [$1/s$]
S	Magnitude of vorticity [$1/s$]
σ	Constant = 2/3
$\tilde{\nu}$	Working variable of eddy viscosity [m^2/s]
$\tilde{S}$	Working variable of vorticity [$1/s$]
$U_{i,j,k}$	Time averaged velocities [m/s]

Speziale $k - \tau$ Model

A_2	Constant = 4.9
$C_{\epsilon 1}$	Constant = 1.44
C_μ	Constant = 0.09
$\mathcal{D}$	Turbulent transport in turbulent kinetic energy equation
$\mathcal{D}_\epsilon$	Turbulent transport in turbulent dissipation rate equation
ϵ	Turbulent dissipation rate
k	Turbulent kinetic energy
$\mathcal{P}_\epsilon$	Production of turbulent dissipation
Φ_ϵ	Destruction of turbulent dissipation
σ_K	Constant = 1.36
$\sigma_{\tau 1}$	Constant = 1.36
σ_{τ_2}	Constant = 1.36
τ	Turbulent time scale [s]

Adaptive $k - \tau$ Model

C_1	Constant = -0.1
C_2	Constant = 0.1
C_3	Constant = 0.26
C_4	Constant = -0.081
C_5	Constant = 0
C_6	0.0405
C_7	-0.0405
$C_{\epsilon 1}$	Constant =1.44
C_μ	Constant = 0.09
k	Turbulent kinetic energy $[J/kg]$
$\overline{k}$	Resolved turbulent kinetic energy $[J/kg]$
k'	Unresolved turbulent kinetic energy $[J/kg]$
L_Δ	Filter length scale $[m]$
L_S	Spatial filter length scale $[m]$
L_t τ	Turbulent time scale $[s]$
$\overline{\tau}$	Resolved turbulent time scale $[s]$
τ'	Unresolved turbulent time scale $[s]$

Acronyms

AKT	Adaptive $k - \tau$ model of Magagnato/Gabi
DNS	Direct Numerical Simulation
KTS	$k - \tau$ model of Speziale/Abid/Anderson
LES	Large Eddy Simulation
NACA	National Advisory Committee for Aeronautics
RANS	Reynolds Averaged Navier Stokes
SA	Spalart Allmaras model
SPARC	Structured Parallel Research Code
URANS	Unsteady Reynolds Averaged Navier Stokes

Acknowledgements

Foremost, I would like to thank my supervisor Dr. Ned Djilali, whose personal interest and subtle encouragement prompted me to continue into graduate studies. It is difficult as an undergrad to absorb with any depth the various fields of engineering and gain enough exposure to learn where personal interests lie. I would also like to thank my co-supervisor, Dr. Afzal Suleman for his practical suggestions and direction in this project.

To my colleagues in the fluids lab, thank you for your helpful discussions and support. I am particularly indebted to Gonçalo Pedro for his many patient hours spent explaining our Linux computer systems and the intricacies of SPARC, which proved its value as a state of the art research code. Discussions with Marc Secanell were very useful, not only in developing my understanding of the code but also in providing moral support through mutual frustration! I would also like to thank Franco Magagnato of the University of Karlsruhe for his patient and straightforward explanations. Our week long visit with Franco was very productive; I realize now that it was the turning point at which the way forward became clear.

(to my parents)

Chapter 1

Introduction

Simulation of massively separated flow over an airfoil beyond stall is, along with prediction of stall itself, a very challenging problem. Prior to the use of CFD in aerodynamics, lift and drag were calculated using panel methods which approximate airfoils by a series of flat plates to which empirical boundary layer equations are applied [2]. Panel methods are not able to predict flow separation; extensive wind tunnel testing has traditionally been required to determine airfoil stall characteristics [3]. Inviscid Euler computations have, up until recently, been the work horse of aerodynamic design due to their low computational cost. Fine grids are not required since the boundary layer is not resolved [4]. As with panel methods, the Euler methods are unable to predict stall.

Navier-Stokes (NS) methods retain the viscous terms in the Navier-Stokes equations giving a balance between viscous, pressure and momentum forces. The computational cost of solving the NS equations is higher than the Euler equations since finer grids are required to resolve the boundary layer and the equations are further complicated by the viscous terms [4].

The full Navier-Stokes equations can not be in general solved directly in the turbulent regime. The practical limit of a Direct Numerical Simulation (DNS) is $Re_c = 10^4$, two orders of magnitude less than an airfoil in the landing configuration [5]. This limitation is imposed by the complexity of turbulent flow and the increasingly smaller scales present at higher Reynolds number that would need to be resolved in a DNS. Designers are seldom interested in all of the time dependent details of turbulence but rather in the time averages of shear stress, pressure and velocity.

In the Reynolds Averaged Navier Stokes (RANS) approach, the NS equations are averaged in time. This removes the unsteadiness of turbulence; all of the terms become steady. The cost of this simplification is the need to introduce model equations for the so-called Reynolds stresses. Engineering turbulence models, such as the classical $k-\epsilon$ model, often achieve this via a turbulent eddy viscosity. The eddy viscosity attempts to represent the physics of turbulence which are removed in the averaging process and must be modelled through semi-empirical relations and transport equations.

The present work has been developed in two parts. In the first part, the performance of RANS turbulence models is examined from a zero angle of attack up to stall. These simulations are carried out at a chord Reynolds number of $Re_c = 3 \times 10^6$ over a symmetric NACA 0012 airfoil for which there is a large database of experimental data in the literature. This permits close scrutiny of the results and enables the validation of turbulence modelling in SPARC.

For the second part of the work, the ability of the turbulence models to predict massively separated flows and vortex shedding in the post stall regime is investigated. To keep the computational requirements reasonable, and, in the interest of predicting NACA 0012 characteristics at a Reynolds number for which there is little experimental data, the second set of simulations is carried out at $Re_c = 10^5$. NACA 0012 airfoil flow is laminar at low angles of attack ($\alpha < 10^\circ$) for $Re_c = 10^5$; turbulence is induced by vortex shedding at post stall angles of attack ($\alpha > 16°$). The unsteady phenomena (vortex shedding and turbulence) in the post stall regime is studied at an angle of attack of $\alpha = 20°$.

The simulations in part 1 are done in steady state; no vortex shedding is allowed. For the second part, the models are run in unsteady mode. This implies that mean values of the time averaged Navier Stokes equations are allowed to fluctuate in time. Small scale turbulent fluctuations are still averaged out and accounted for by the turbulence model, but large scale fluctuations and coherent structures are resolved. There is a distinction here between turbulent fluctuations and the fluctuations of large scale vortex shedding. The mechanism of vortex shedding for the NACA 0012 at $\alpha = 20°$ and $Re_c = 10^5$ includes adverse pressure gradient and Kelvin Helmholtz instability [6].

The Spalart Allmaras one equation and Speziale $k - \tau$ two equation models are used for the steady state simulations in the first part; these are both RANS models. They are used in URANS (Unsteady Reynolds Averaged Navier Stokes) mode for the second part, along with the adaptive $k - \tau$ model of Magagnato [7]. The adaptive model of Magagnato is not a pure URANS model; it is a hybrid of URANS and DNS.

Simulations in the first part of this work are validated against quantitative experimental data. Simulations in the second part, while still providing quantitative data, are intended to provide a qualitative picture of vortex shedding at high angles of attack. All simulations are run in two dimensions. This is appropriate at low angles of attack where the mean flow is largely two-dimensional. Vortex shedding in the stalled regime is a three dimensional phenomena; vortices are stretched and twisted in all directions. By constraining the simulation to two dimensions, this interaction is limited. The simulations capture only part of the flow dynamics; the remainder, including span-wise three dimensional effects and small scale turbulence, is captured using a turbulence model.

A few comments should be made on the selection of Reynolds numbers for simulations in this work. The high Reynolds number used for steady simulations in the first part ($Re_c = 3 \times 10^6$) is typical of transport aircraft in the landing and takeoff configurations and of oscillating hydrofoil propulsion. A hydrofoil with a 1m chord travelling at 1.5 m/s has a chord Reynolds Number of $Re_c = 3 \times 10^6$. While it is possible to run unsteady simulations at $Re_c = 3 \times 10^6$, the computing time and the necessary grid refinement make it expensive. Unsteady simulations are therefore run at $Re_c = 10^5$. Small aerial vehicles such as gliders and very high altitude aircraft (greater than 30,000 m) operate in this regime [8] [9]. Low Reynolds number airfoil data is of interest since little experimental data is available at $Re_c = 10^5$, particularly in stall conditions.

1.1 Motivation

The purpose of this work is to set up the computational domain for an airfoil and evaluate the performance of the turbulence models in the research code SPARC (Structured PArallel Research Code) [10]. This is directed at research projects in underwater propulsion and airfoil optimization at the University of Victoria. The underwater propulsion work is being carried out by Pedro [11] and the airfoil optimization by Secanell [12]. Pedro is focusing on flapping hydrofoil propulsion and fluid-structure interaction [13]. Swim fin and small autonomous underwater vehicle flapping hydrofoils encounter chord Reynolds number of several million which is well into the turbulent regime. The computational domain, grid requirements and turbulence models should be verified in a simple configuration before attempting to solve problems with moving meshes and deformable bodies.

1.2 State of the Art CFD for Airfoils

Recent CFD airfoil validation projects include the European Initiative on Validation of CFD Codes (EUROVAL)[14], [15] and the European Computational Aerodynamics Research Project (ECARP). The goal of these projects was to determine the ability of various turbulence models to predict separation and maximum lift just before stall. Aerospatiale's *A-Airfoil*, for which there is extensive experimental data, was used for validation in both projects. A standard grid with 96,512 grid points was used for all simulations. High Reynolds number flow in these conditions is one of the most challenging cases for CFD. ECARP concluded that algebraic and standard eddy viscosity models fail to correctly predict separation and therefore maximum lift at high angles of attack.

Weber and Ducros [15] conducted RANS and LES simulations over the *A-Airfoil* near stall at $Re_c = 2.1 \times 10^6$. They found that LES results are quantitatively very close to Spalart Allmaras model results. LES simulations took 140 times more computer resources than the Spalart Allmaras model on the same grid. Convergence with RANS was not obtained at high angles of attack. The exact solution of the RANS equations in conjunction with a turbulence model is unsteady in this condition due to vortex shedding.

Weber and Ducros [15] used the ECARP C type grid with 512 points along the airfoil surface, 64 points in the cross stream direction and 498 points in the downstream direction. They allowed 10 chord lengths to far field boundaries in the upstream and cross stream directions. Wall functions were not used; the first grid point from the wall was located at approximately $y^+ = 2$. While the classic turbulence models were able to predict many features such as a laminar boundary layer close to the leading edge, separation at the trailing edge and the interaction of two shear layers in the wake, they failed to correctly predict the separation zone at high angles of attack. Both the RANS and LES simulations carried out in [15] did not provide boundary layer separation with the correct back flow characteristics.

Chaput [14] of Aerospatiale has carried out validation of turbulence models under ECARP using the EUROVAL Aerospatiale *A-Airfoil* grid. Sixteen partners are involved in the project, including BAe, DLR, Dornier/Dasa-LM and SAAB. The focus is a comparison between the performance of various turbulence models at maximum lift. The extensive database of numerical and experimental data from the EUROVAL project is used as a starting point. The project does not include the algebraic Baldwin Lomax and the standard $k - \epsilon$ models. While these models are widely used in industry, their widespread failure to predict separation is well documented. Examples include the papers by Davidson and Rizzi [16] as well as Rhie and Chow [17].

EUROVAL and ECARP found that Navier Stokes methods are capable of accurate prediction of boundary layer separation in pre-stall conditions but that accurate prediction of maximum lift is not achieved. Good results can be obtained by using turbulence models which take into account the strong nonlinear equilibrium processes at high angles of attack. Transition to turbulence near the leading edge is still problematic; turbulence models do not reliably predict transition on their own. Transition is often specified *a priori*, but this problem should be resolved before conclusions can be made about turbulence model performance [14].

1.2.1 Classification of Turbulence Models

The major categories of turbulence modelling in CFD are outlined below in order of increasing complexity and computational cost [18], [15], [19], [20]. Algebraic models are simple and computationally inexpensive; they solve the time averaged N-S equations by calculating an eddy viscosity algebraically from the mean flow field. Wall functions are used to apply an appropriate velocity profile near the wall and to determine the wall shear stresses. This removes the need for a fine near wall grid but also makes algebraic models inappropriate for complex separated flows. The one equation model of Spalart Allmaras [21] is the simplest model used in this work; it solves a single transport equation for eddy viscosity and does not use wall functions. The two equation model of Speziale Abid Anderson [22] is also used here; it solves transport equations for the turbulent kinetic energy k and the turbulent time scale τ. Reynolds stress models (RSM) solve several transport equations for the Reynolds stresses. Though they offer good accuracy, RSM models are expensive and have poor numerical properties [15], [23]. In order to properly predict turbo machinery pressure losses, Magagnato and Gabi [7] developed a hybrid RANS-LES model. This is similar to an LES except that it uses a much coarser grid. Two equation turbulence models are used for the sub-grid scales rather than an algebraic model. Though the adaptive model is more expensive than RANS, it is still much cheaper than LES.

1. Algebraic Models
    - Express eddy viscosity in terms of mean flow quantities
    - Robust and cheap
    - Limited to simple flows; not good for separation or shocks
    - Example: Baldwin-Lomax [24] and Cebeci-Smith
2. Half Equation Models
    - Use one simplified transport equation for eddy viscosity
    - Example: Johnson-King Model; difficult to extend to 3D applications
3. One Equation Models

- Use one transport equation for eddy viscosity μ_t
- Reasonable results and computational cost
- Compromise between algebraic and two equation models
- Example: Spalart-Allmaras [21] and Baldwin-Barth

4. Two Equation Models

    - Transport equations for turbulent kinetic energy and time scale or dissipation
    - Independent of an algebraic length scale (Prandtl's mixing length)
    - Account for history effects through transport equations
    - Do not predict anisotropy of turbulence
    - Difficulty with accurate prediction of separation and complex geometries
    - Example: $k - \tau$ model of Speziale-Abid-Anderson [22]

5. Reynolds Stress Models (RSM)

    - Multiple transport equations for Reynolds stress terms
    - Do not rely on eddy viscosity concepts
    - High computational cost relative to other models due to numerous transport equations

6. Adaptive LES-RANS Model

    - Hybrid between LES and RANS; use of a coarser grid than LES is possible by using better subgrid scale turbulence models
    - Similar to Very Large Eddy Simulation (VLES)

- Designed for separated, 3D unsteady turbo machinery flow with reasonable computational cost in mind
- Example: Magagnato-Gabi [7]

7. Large Eddy Simulation (LES)
    - Solves full N-S equations with filtering of small scales by grid size
    - Resolves 3D time dependent details for large and medium scales
    - Computationally expensive but only way to simulate complex flows where turbulence models are inadequate
    - Limited to flows where $Re < 10^5$
8. Direct Numerical Simulation (DNS)
    - Solves full N-S equations
    - Very computationally expensive; all details of turbulence are resolved
    - Limited to flows where $Re < 10^4$

Large eddy simulations are computationally expensive; they resolve the major details of the flow down to the Kolmogorov dissipation scales. They are appropriate for complex 3D separated flows [5], [25]. A DNS solves the full Navier Stokes equations and is even more expensive as all of the flow details are resolved. LES and DNS are not used in this work.

1.2.2 Prediction of Friction Drag

Accurate prediction of skin friction drag in the design of aerodynamic bodies has traditionally been, and continues to be, a difficult task. For a NACA 0012 airfoil at an angle of attack of $\alpha = 4°$, the coefficient of lift is $C_l = 0.44$, the total drag coefficient is $C_d = 0.0068$ and the friction drag coefficient is approximately $C_{df} = 0.0034$ (See Speziale $k-\tau$ simulations in Chapter 3). Measuring drag in a wind tunnel is challenging since it is two orders of magnitude smaller than lift. Experimental results are not readily available for friction drag on the NACA 0012 airfoil [1].

Inviscid solutions are only capable of predicting induced (pressure) drag. Viscous (friction) drag prediction requires resolution of the boundary layer. RANS is very good at predicting pressure distributions but friction predictions are more difficult. The usual approach has been to use wall functions (law of the wall)[26]. Wall functions allow the first grid point from the wall to be located at approximately $y^+ = 30$ since they assume a logarithmic velocity profile for $y^+ < 30$. Shear stress at the wall is proportional to the velocity gradient; this is determined by the wall function profile. Wall functions are appropriate for attached flow at low angles of attack. They are not appropriate for separated flows where the velocity at the wall is reversed. Lombardi [1] has done simulations for the NACA 0012 airfoil at $\alpha = 0°$ using wall functions with the standard $k - \epsilon$ turbulence model with approximately 37,000 grid points. In this work, drag is predicted without using wall functions; this requires that the first grid point from the wall be located at approximately $y^+ = 1$. The final grid used in this work for $Re_c = 3 \times 10^6$ has 130,368 grid points. With this approach, the friction is very sensitive to the near wall resolution and the type of turbulence model used. Inadequate grid resolution in the boundary layer can lead to inaccurate boundary layer development and therefore large errors in the friction and pressure forces [27].

1.3 Outline of Thesis

Chapter 2 presents the theoretical background of the thesis. The Navier Stokes equations and the time averaging process are given. Eddy viscosity and turbulence modelling are discussed and the major transport equations of the turbulence models are presented. SPARC and the computational setup are discussed along with the routines for calculating surface shear stresses. Chapter 3 presents the results of steady state simulations at $Re_c = 3 \times 10^6$ for various angles of attack. The results of a grid study are also given. Contour plots for the velocity, pressure, eddy viscosity, turbulent kinetic energy and turbulent time scale are presented for the various angles of attack, along with surface pressure distributions. Chapter 4 presents the results for unsteady simulations at $Re_c = 10^5$. Results for the Spalart Allmaras, Speziale $k - \tau$ and adaptive $k - \tau$ models are given. Contour plot snapshots are shown at various intervals so that the time evolution of the flow field can be tracked. Plots of time averaged results are given and compared between models. Conclusions and recommendations for future work are discussed in Chapter 5. Full details of the turbulence models are given in Appendix A; Appendix B has tabular data from the eddy viscosity study in Chapter 3.

Chapter 2

Theory

2.1 Aeronautical Nomenclature

2.1.1 Airfoil Dimensionless Parameters

The forces which act on an airfoil are functions of density ρ, molecular viscosity μ, free stream velocity U_∞ and chord length c. Through dimensional analysis, these variables can be combined into a single non-dimensional parameter, the chord Reynolds number Re_c which is a measure of the ratio of inertial to viscous forces:

$$Re_c = \frac{\rho U_\infty c}{\mu} = \frac{U_\infty c}{\nu} \tag{2.1}$$

where $\nu = \frac{\mu}{\rho}$ is the kinematic viscosity. In analogy to the Reynolds number, the lift, drag and friction forces can also be written as non-dimensional coefficients. These are the coefficient of lift C_l, the coefficient of drag C_d, the coefficient of pressure drag C_{dp}, the coefficient of friction drag C_{df} and the skin friction coefficient C_f. Forces are non-dimensionalized by the dynamic pressure $\frac{1}{2}(\rho U_\infty^2)$ and the wing area S. In this work S is set to 1 since the simulations are two dimensional.

$$C_l = \frac{\text{lift}}{\frac{1}{2}\rho U_\infty^2 S} \tag{2.2}$$

$$C_d = \frac{\text{drag}}{\frac{1}{2}\rho U_\infty^2 S} \tag{2.3}$$

$$C_{df} = \frac{\text{friction drag}}{\frac{1}{2}\rho U_\infty^2 S} \tag{2.4}$$

$$C_{dp} = \frac{\text{pressure drag}}{\frac{1}{2}\rho U_\infty^2 S} \tag{2.5}$$

$$C_f = \frac{\text{shear stress}}{\frac{1}{2}\rho U_\infty^2} \tag{2.6}$$

Pressure forces can also be non-dimensionalized using the difference between the local pressure P, the free stream pressure P_∞ and the dynamic pressure:

$$C_p = \frac{P - P_\infty}{\frac{1}{2}\rho U_\infty^2} \tag{2.7}$$

2.1.2 Aerofoil Geometry

Figure 2.1 shows the geometry of a symmetric NACA 0012 airfoil.

- Chord (c): straight line joining the leading and trailing edges.

- Leading Edge (LE): point at the front of the airfoil where the chord line intersects the airfoil surface.
- Trailing Edge (TE): point at the rear of the airfoil where the chord line intersects the airfoil surface
- Angle of Attack (α): Angle between the chord line and the free stream velocity vector U_∞.

Only the symmetric (zero camber) NACA 0012 airfoil is used in this work.

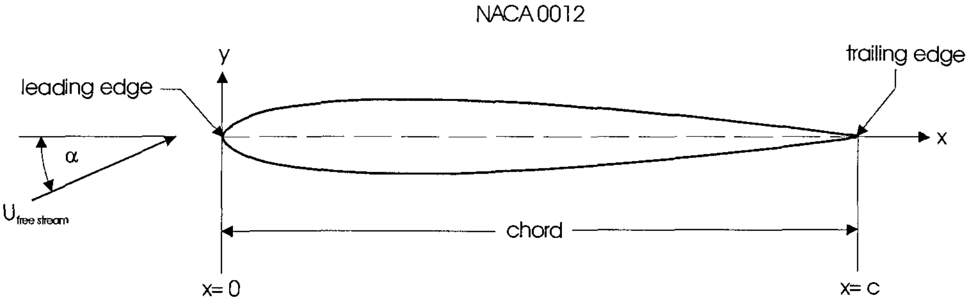

Figure 2.1: Layout of NACA 0012 Airfoil showing Chord, Leading Edge (LE) and Trailing Edge (TE)

The NACA 4 digit airfoil surface is defined by a fourth order polynomial as shown in equation (2.9). Here t is the maximum thickness in percent chord and x is the position on the chord line from the leading edge relative to the overall chord length c. The y-coordinates of the airfoil surface are found by adding the camber y_c and the thickness y_t. For the symmetric NACA 0012, only the thickness y_t is used.

$$\text{NACA}\ \underbrace{0}_{100m/c}\ \underbrace{0}_{10p/c}\ \underbrace{12}_{t/c} \tag{2.8}$$

$$\pm y_t = \frac{t}{0.20}\left(0.29690\sqrt{x} - 0.12600x - 0.35160x^2 + 0.28430x^3 - 0.10150x^4\right) \tag{2.9}$$

The forces acting on an airfoil are broken down into two components: lift and drag. Drag can be further decomposed into two components, the viscous drag due to viscous shearing forces and the pressure drag due to pressure forces. Pressure forces always act in a direction perpendicular to the airfoil surface while viscous forces act in a tangential direction as shown in figure 2.2:

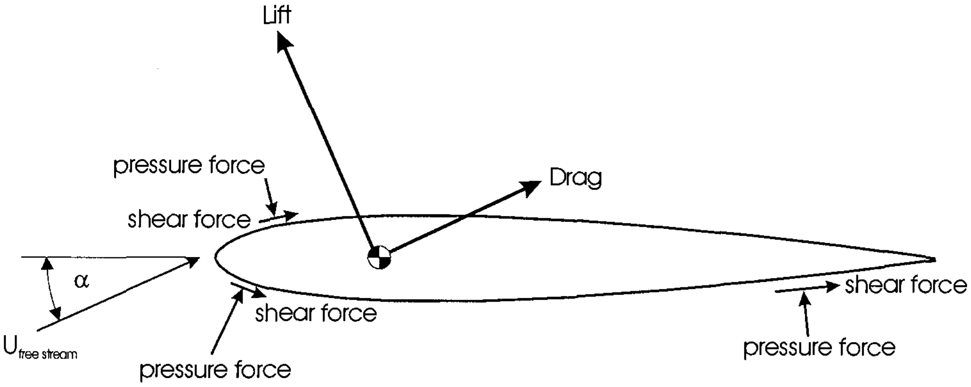

Figure 2.2: Schematic of Forces Acting on a NACA 0012 Airfoil

The the total lift and total drag are the sum of all the forces acting around the airfoil surfaces. Lift is always perpendicular to the free stream velocity and the drag is parallel to it.

2.2 Vortex Shedding and Stall

It is well established that all structures, particularly bluff bodies, shed vortices in subsonic flow [28]. Vortex street wakes tend to be very similar regardless of the body geometry. A well documented example of vortex shedding is the flow around circular cylinders. The aeolian tones of electrical transmission wires in a strong wind are caused by pressure induced vibration due to vortex shedding. In 1878 Strouhal found that the aeolian tones emitted from a wire of circular cross section were proportional to

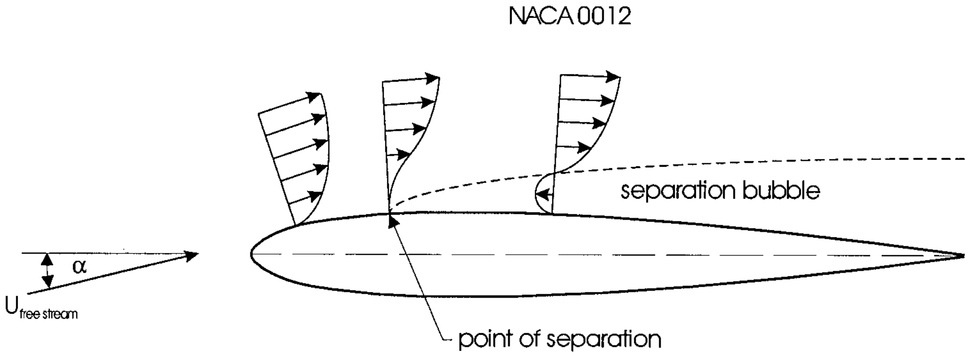

Figure 2.3: Nomenclature of Flow Separation and Associated Velocity Profiles

the wind speed and wire diameter [29]. The Strouhal number St is the dimensionless proportionality constant between the vortex shedding frequency f_s, wind speed U_∞ and cylinder diameter d:

$$f_s = \frac{StU_\infty}{d} \tag{2.10}$$

Vortex shedding is caused by flow separation, a viscous phenomenon[1] associated with either abrupt changes in geometry or adverse pressure gradient. There are two major separated flow regimes for the NACA 0012 airfoil. The first is a laminar separation bubble at the leading edge which appears at $C_l \cong 0.9$ and $\alpha \cong 9°$ for $Re_c \cong 3 \times 10^6$ [30]. Laminar flow at the leading edge separates due to the adverse pressure gradient caused by the high curvature of the airfoil from $x/c = 0$ to $x/c = 0.1$. Transition to turbulence usually occurs where the flow re-attaches to the airfoil surface.

The second separated flow regime occurs in the massively stalled region at $\alpha \approx 16°$; a large separation bubble begins to form at the trailing edge and gradually moves

---

[1] Inviscid flow theory often used for low angle of attack aerodynamics is not applicable to high angle of attack flows as it is incapable of predicting flow separation.

forward. This regime is associated with the shedding of large vortices.

Stall for the NACA 0012 section is difficult to quantify experimentally. Gregory [30] found that for $Re_c \cong 3 \times 10^6$, the stall may originate from the collapse of the leading edge laminar separation bubble. However, for higher Re_c, the stall appears to originate entirely from the forward propagation of the trailing edge separation bubble.

Vortex shedding for cylinders at low Reynolds numbers in the laminar regime is a steady, harmonic two-dimensional phenomena. This is not the case for turbulent flow. Vortex shedding at high Reynolds numbers occurs over a narrow band of shedding frequencies and is highly three dimensional.

Airfoils, in manner analogous to cylinders, form a vortex wake at a Strouhal number of $St \cong 0.2$ based on the width d of the boundary layers at the trailing edge [31], [29]. Further, if d is defined as the width between separation points, $St \cong 0.2$ applies over broad ranges of Reynolds numbers regardless of section geometry [29]. The characteristic dimension used in calculating the Strouhal number in this work is the chord length c.

2.3 Conservation Theorems

Three fundamental equations are solved in CFD: continuity (conservation of mass), Newton's Second Law (conservation of momentum) and the conservation of energy. Compressibility effects are negligible in this work (Mach number less than 0.1); the weakly compressible Navier Stokes equations are solved [32]. The energy equation is solved but as the flow field temperature variations are small (less than 1 Kelvin), it will not be considered further.

The continuity equation states that mass cannot be created or destroyed. It reads:

$$\frac{\partial \rho}{\partial t} = \frac{\partial}{\partial x}(\rho u) + \frac{\partial}{\partial y}(\rho v) + \frac{\partial}{\partial z}(\rho w) \tag{2.11}$$

The Navier-Stokes (NS) equations are an adaptation of Newton's Second Law for fluids. They are obtained using the constitutive relations for the viscous and pressure forces. The x, y and z components of the NS equations are:

$$\begin{aligned} \rho\frac{Du}{Dt} = &- \frac{\partial P}{\partial x} + \frac{\partial}{\partial x}\left[\mu\left(2\frac{\partial u}{\partial x} - \frac{2}{3}\nabla \cdot \vec{U}\right)\right] + \\ &+ \frac{\partial}{\partial y}\left[\mu\left(\frac{\partial u}{\partial y} + \frac{\partial v}{\partial x}\right)\right] + \frac{\partial}{\partial z}\left[\mu\left(\frac{\partial w}{\partial x} + \frac{\partial u}{\partial z}\right)\right] \end{aligned} \tag{2.12}$$

$$\begin{aligned} \rho\frac{Dv}{Dt} = &- \frac{\partial P}{\partial y} + \frac{\partial}{\partial y}\left[\mu\left(2\frac{\partial v}{\partial z} - \frac{2}{3}\nabla \cdot \vec{U}\right)\right] + \\ &+ \frac{\partial}{\partial z}\left[\mu\left(\frac{\partial v}{\partial z} + \frac{\partial w}{\partial y}\right)\right] + \frac{\partial}{\partial x}\left[\mu\left(\frac{\partial u}{\partial y} + \frac{\partial v}{\partial x}\right)\right] \end{aligned} \tag{2.13}$$

$$\begin{aligned} \rho\frac{Dw}{Dt} = &- \frac{\partial P}{\partial z} + \frac{\partial}{\partial z}\left[\mu\left(2\frac{\partial w}{\partial y} - \frac{2}{3}\nabla \cdot \vec{U}\right)\right] + \\ &+ \frac{\partial}{\partial x}\left[\mu\left(\frac{\partial w}{\partial x} + \frac{\partial u}{\partial z}\right)\right] + \frac{\partial}{\partial y}\left[\mu\left(\frac{\partial v}{\partial z} + \frac{\partial w}{\partial y}\right)\right] \end{aligned} \tag{2.14}$$

Using tensor notation, where repeated subscripts i, j or k imply summation over all values of the repeated subscript, the Navier-Stokes equations are written in compact form:

$$\rho\frac{Du_i}{Dt} = -\frac{\partial P}{\partial x_i} + \frac{\partial}{\partial x_j}\left\{\mu\left(\frac{\partial v_i}{\partial x_j} + \frac{\partial v_j}{\partial x_i} - \frac{2}{3}\delta_{ij}\frac{\partial v_k}{\partial x_k}\right)\right\} \qquad (i,j,k = 1,2,3) \qquad (2.15)$$

The Kronecker delta δ_{ij} is equal to 1 if $i = j$ and 0 if $i \neq j$. The substantial derivative is used here; it can be broken down as shown:

$$\frac{Du_i}{Dt} = \frac{\partial u_i}{\partial t} + u\frac{\partial u_i}{\partial x} + v\frac{\partial u_i}{\partial y} + w\frac{\partial u_i}{\partial z} \qquad (2.16)$$

2.4 Turbulence

> "Most flows which occur in practical applications are turbulent, the term denoting a motion in which an irregular fluctuation (mixing, or eddying motion) is superimposed on the main stream." Schlichting [33]

Turbulence is one of the most difficult problems of fluids engineering. It is characterized by a chaotic, tumbling, unsteady pattern of vortices and flow structures which are continually interacting with each other in three dimensions. The scales of motion, that is, the diameter and length of vortices in a flow, can vary over many orders of magnitude.

Consider turbulent flow in a pipe. While the mass flow rate may be constant with time, the velocity at a fixed point fluctuates. The time average of this velocity is constant as long as the total mass flow rate is constant. Osborne Reynolds introduced this concept in 1895 by writing velocity and pressure in terms of mean and fluctuating components:

$$u = \overline{u} + u', \qquad v = \overline{v} + v', \qquad w = \overline{w} + w', \qquad p = \overline{p} + p' \qquad (2.17)$$

The mean, where T is the averaging period, is defined as:

$$\overline{u} = \frac{1}{T}\int_0^T u\,dt \tag{2.18}$$

The fluctuating component of the stream wise velocity u' is the difference between the total velocity u and the mean velocity $\overline{u}$ and has a zero mean (time averaged) value. The mean of the product of two fluctuating variables is generally non-zero.

$$\overline{u'^2} \neq 0, \qquad \overline{u'v'} \neq 0 \tag{2.19}$$

Decomposition of a turbulent variable into mean and fluctuating components can now be applied to the Navier-Stokes equations. Writing the NS equations in the time averaged form makes them mathematically tractable for modelling turbulent flows at the expense of resolving all of the flow detail.

The time averaging process gives rise to additional terms known as the Reynolds stresses. These terms must be modelled in order to solve the time averaged NS equations since they are additional variables for which there are no further equations from physical laws or constitutive relations. Turbulence modelling is the derivation of semi-empirical relations that try to simulate the physics of turbulence and exert its influence through the Reynolds stress terms in the time averaged NS equations.

The incompressible time averaged continuity and Navier-Stokes equations are:

$$\frac{\partial \overline{u}}{\partial x} + \frac{\partial \overline{v}}{\partial y} + \frac{\partial \overline{w}}{\partial z} = 0 \qquad \text{incompressible continuity} \tag{2.20}$$

$$\begin{aligned}\rho\frac{D\overline{u}}{Dt} &= -\frac{\partial\overline{p}}{\partial x}+\frac{\partial}{\partial x}\left(\mu\frac{\partial\overline{u}}{\partial x}-\rho\overline{u'^2}\right)+\frac{\partial}{\partial y}\left(\mu\frac{\partial\overline{u}}{\partial y}-\rho\overline{u'v'}\right)+\\ &\quad\frac{\partial}{\partial z}\left(\mu\frac{\partial\overline{u}}{\partial z}-\rho\overline{u'w'}\right)\qquad x \text{ direction}\end{aligned}\tag{2.21}$$

$$\begin{aligned}\rho\frac{D\overline{v}}{Dt} &= -\frac{\partial\overline{p}}{\partial y}+\frac{\partial}{\partial x}\left(\mu\frac{\partial\overline{v}}{\partial x}-\rho\overline{u'v'}\right)+\frac{\partial}{\partial y}\left(\mu\frac{\partial\overline{v}}{\partial y}-\rho\overline{v'^2}\right)+\\ &\quad\frac{\partial}{\partial z}\left(\mu\frac{\partial\overline{v}}{\partial z}-\rho\overline{v'w'}\right)\qquad y \text{ direction}\end{aligned}\tag{2.22}$$

$$\begin{aligned}\rho\frac{D\overline{w}}{Dt} &= -\frac{\partial\overline{p}}{\partial z}+\frac{\partial}{\partial x}\left(\mu\frac{\partial\overline{w}}{\partial x}-\rho\overline{u'w'}\right)+\frac{\partial}{\partial y}\left(\mu\frac{\partial\overline{w}}{\partial y}-\rho\overline{v'w'}\right)+\\ &\quad\frac{\partial}{\partial z}\left(\mu\frac{\partial\overline{w}}{\partial z}-\rho\overline{w'^2}\right)\qquad z \text{ direction}\end{aligned}\tag{2.23}$$

The fluctuation of velocity, the stretching and tumbling of eddies and the random movement of packets of fluid are very effective at mixing the flow. Heat, mass and momentum are transported in the flow field in a very thorough manner by the turbulent motions. In a boundary layer, turbulent mixing transfers momentum from the high mean velocity area outside the boundary layer toward the wall. This transfer of momentum from the free stream causes a momentum deficit. This deficit will be larger than in the laminar case where molecular diffusion is the only mechanism of momentum transfer. The additional momentum deficit for the turbulent flow imparts a greater drag on the free stream. If the flow field is solved only in terms of the mean values, which are usually of interest in engineering, these values must still reflect the greater drag caused by the transfer of momentum through turbulent fluctuations. Prandtl's eddy viscosity attempts to do this by solving a mean where the fluctuating motions have been removed, but their effects have been accounted for by adding an eddy viscosity. The total viscosity is then the sum of the laminar (molecular) and turbulent components where the additional drag on the wall and the additional momentum deficit to the free stream due to turbulence are accounted for by the so called eddy viscosity.

Sir Issac Newton proposed a linear resistance law for laminar flow in 1687 [34]. The viscous stress τ is proportional to the laminar viscosity μ and the velocity gradient $\partial u/\partial y$ as shown in equation (2.24). For a wall u is the tangential velocity and y is the distance from the wall. Most fluids of engineering interest, particularly air and water, obey equation (2.24) and are therefore classified as Newtonian fluids.

$$\tau_{ij} = \mu \left(\frac{\partial \overline{u_i}}{\partial x_j} + \frac{\partial \overline{u_j}}{\partial x_i} \right) \quad \text{laminar shear stress} \tag{2.24}$$

Boussinesq proposed an analogy to the laminar shearing stress equation for turbulent flows [33]:

$$\tau_{ij}^t = -\rho \overline{u_i' u_j'} \quad \text{turbulent shear stress} \tag{2.25}$$

Prandtl suggested that the turbulent shear stress could be related to the mean flow field through the eddy viscosity in a manner analogous to the laminar viscosity and laminar shear stress. The eddy viscosity approximates the Reynolds stresses from gradients of the mean flow:

$$\tau_{ij}^t = \mu_t \left(\frac{\partial \overline{u_i}}{\partial x_j} + \frac{\partial \overline{u_j}}{\partial x_i} \right) - \frac{2}{3} \rho k \delta_{ij} \tag{2.26}$$

Where μ_t is the eddy viscosity proposed by Prandtl and k is the turbulent kinetic energy. While the laminar viscosity μ is a function of the chemical properties of the fluid and of temperature, the eddy viscosity depends on flow field properties such as velocity and time.

Note that in RANS simulations, the time averaged NS equations are being solved. Since the turbulent fluctuations have been removed be the time averaging process, the equations yield a steady solution. The solution complexity is then similar to a laminar flow except that the physics of the turbulence are accounted for through an increased viscosity by the addition of the eddy viscosity.

2.5 Turbulence Models

This section presents three turbulence models, in order of increasing complexity, which define the eddy viscosity term. As discussed earlier, it is necessary to model the eddy viscosity through semi-empirical methods as there are no further physical laws or constitutive relations that can be used to define it.

2.5.1 Spalart Allmaras One Equation Model

The Spalart Allmaras One Equation Model (SA) solves the Reynolds averaged Navier Stokes equations and a single transport equation for eddy viscosity. The eddy viscosity transport equation is based on empiricism, dimensional analysis, Galilean invariance and molecular viscosity μ where appropriate [21]. The model is local; the equation at one point does not depend on the solution at another point. The model is designed to be compatible with grids of any structure and can be used for 2D and 3D problems. It is calibrated for aerodynamic flows such as flat plate boundary layers, boundary layers with pressure gradient, mixing layers and wakes. The Spalart Allmaras model is based on the Baldwin Barth model, but is claimed more accurate and better able to accept zero values of eddy viscosity in the free stream. Spalart [21] notes that while two equation models are quite sensitive to upstream and free stream turbulent parameters of length scale and turbulent intensity, the SA model can deal with zero values making it easier to set boundary conditions. SPARC does not allow a zero eddy viscosity in the free stream. The results of a parametric eddy viscosity study are presented later.

Spalart claims that the lack of a turbulent kinetic energy transport equation does not have any significant effect for thin shear layer flows. Equation (2.27) is the transport equation for the eddy viscosity working variable $\tilde{\nu}$ in the SA model. $\tilde{\nu}$ is equal to the eddy viscosity ν_t except in the viscous region where it is damped by the viscous damping function f_{v1}. The various terms in equation (2.27) are explained by the bracketed terms. $\tilde{S}$ is the magnitude of the vorticity and d is the distance from the nearest wall. The full set of ancillary equations, constants and damping functions is given in Appendix A.

$$\begin{aligned}\underbrace{\frac{D\tilde{\nu}}{Dt}}_{\text{material derivative}} &= \underbrace{C_{b1}\left[1-f_{t2}\right]\tilde{S}\tilde{\nu}}_{\text{production}} + \\ &+ \underbrace{\frac{1}{\sigma}\left[\nabla\cdot(\nu+\tilde{\nu})\nabla\tilde{\nu}+C_{b2}(\nabla\tilde{\nu})^2\right]}_{\text{diffusion}} + \\ &- \underbrace{\left[C_{w1}f_w-\frac{C_{b1}}{\kappa^2}f_{t2}\right]\left[\frac{\tilde{\nu}}{d}\right]^2}_{\text{near wall dissipation and re-laminarization}} + \underbrace{f_{t1}\Delta U^2}_{\text{tripping source term}}\end{aligned} \tag{2.27}$$

The near wall dissipation term allows for an accurate logarithmic velocity profile in the boundary layer. The re-laminarization terms allow the eddy viscosity to be reduced to zero in regions where re-laminarization might occur.

The implementation of the SA model in SPARC uses equation (2.27) but lacks the tripping source term. This term is designed to artificially increase the eddy viscosity in a near wall region around a turbulent transition point specified by the user. According to Spalart [21] "On no account should the turbulence model be trusted to predict the transition location." The tripping point is not specified in this work; its importance is minimized by running simulations at either high Reynolds numbers where the transition occurs essentially at the leading edge, shown later in shear stress plots, or at high angles of attack where the separation point is very near the leading edge and the location of the transition point is not expected to have much influence on the lift and drag coefficients. Though beyond the scope of this work, the tripping function should be implemented in order to properly predict laminar separation bubbles and transition at lower angles of attack and lower Reynolds numbers. Further details are available in the paper by Spalart and Allmaras [21].

2.5.2 Speziale Two Equation $k - \tau$ Model

The two equation $k - \tau$ model of Speziale/Abid/Anderson [22] was developed to overcome difficulties encountered with popular $k - \epsilon$ models. Two equation models are suitable for a wider range of applications than algebraic and one equation models. One of the most widely used two equation models is the $k - \epsilon$ model. This is a robust model that provides reasonable predictions for boundary layer and shear layer flows. The performance of the $k - \epsilon$ models is however unsatisfactory in many respects for separated flows [25]. Another aspect of the standard $k - \epsilon$ is its inability to account for low Reynolds number near-wall transport. Wall functions are required which again are not entirely appropriate for separated flows. There is no natural wall boundary condition for ϵ. This leads to derived or postulated boundary conditions that are not always physically correct [22]. Both the $k - \epsilon$ and $k - \tau$ models use transport equations for turbulent kinetic energy but rather than using the dissipation ϵ for a second transport equation, the $k - \tau$ model uses the turbulent time scale $\tau \equiv k/\epsilon$.

The transport equations have the following form:

$$\frac{Dk}{Dt} = \tau_{ij}\frac{\partial \overline{u_i}}{\partial x_j} - \epsilon - \mathcal{D} + \nu\nabla^2 k \tag{2.28}$$

$$\begin{aligned} \frac{D\tau}{Dt} = & \frac{\tau}{k}\tau_{ij}\frac{\partial \overline{u_i}}{\partial x_j} - 1 - \frac{\tau}{k}\mathcal{D}\frac{\tau^2}{k}\mathcal{P}_\epsilon + \frac{\tau^2}{k}\Phi_\epsilon + \frac{\tau^2}{k}\mathcal{D}_\epsilon + \\ & + \frac{2\nu}{k}\frac{\partial k}{\partial x_i}\frac{\partial \tau}{\partial x_i} - \frac{2\nu}{\tau}\frac{\partial \tau}{\partial x_i}\frac{\partial \tau}{\partial x_i} + \nu\nabla^2\tau \end{aligned} \tag{2.29}$$

Here $\mathcal{D}$ is the turbulent transport term of turbulent kinetic energy k, $\mathcal{D}_\epsilon$ is the turbulent transport term of turbulent dissipation and $\mathcal{P}_\epsilon$ and Φ_ϵ are production and destruction of turbulent dissipation terms. The final form of the transport equations for the turbulent kinetic energy k and the turbulent time scale τ are:

$$\frac{Dk}{Dt} = \tau_{ij}\frac{\partial \overline{u}_i}{\partial x_j} - \frac{k}{\tau} + \frac{\partial}{\partial x_i}\left[\left(\nu + \frac{\nu_t}{\sigma_k}\right)\frac{\partial k}{\partial x_i}\right] \tag{2.30}$$

$$\begin{aligned} \frac{D\tau}{Dt} = & (1 - C_{\epsilon 1})\frac{\tau}{k}\tau_{ij}\frac{\partial \overline{u}_i}{\partial x_j} + (C_{\epsilon 2} f_2 - 1) + \\ & + \frac{2}{k}\left(\nu + \frac{\nu_t}{\sigma_{\tau 1}}\right)\frac{\partial k}{\partial x_i}\frac{\partial \tau}{\partial x_i} - \frac{2}{\tau}\left(\nu + \frac{\nu_t}{\sigma_{\tau 2}}\right)\frac{\partial \tau}{\partial x_i}\frac{\partial \tau}{\partial x_i} + \\ & + \frac{\partial}{\partial x_i}\left[\left(\nu + \frac{\nu_t}{\sigma_{\tau 2}}\right)\frac{\partial \tau}{\partial x_i}\right] \end{aligned} \tag{2.31}$$

The full set of ancillary equations, constants and damping functions is given in Appendix A and in the paper by Speziale/Abid/Anderson [22].

2.5.3 Adaptive $k-\tau$ Model

Reynolds Averaged Navier Stokes (RANS) models are designed to capture all of the unsteady effects of turbulence; a steady state RANS calculation cannot resolve any fluctuations. In unsteady calculations, a fraction of the large scale unsteadiness must be resolved by the simulations; the turbulence model accounts only for the unresolved part of the turbulence.

Large Eddy Simulations (LES) model only a small part of the turbulent fluctuations and resolve the rest. The level of resolution is determined by the grid size and time step; fluctuations which have length and time scales smaller than the grid are accounted for by a subgrid scale model [35].

Magagnato and Gabi [7] have proposed a new adaptive $k-\tau$ model that can be used for any grid resolution in the unsteady case. The model reduces to a standard two equation model in steady state and adapts to resolvable fluctuations based on grid size in unsteady calculations. The model is designed for highly unsteady and three dimensional turbo machinery flows. RANS models are unable to adequately predict pressure losses for turbo machinery and DNS and LES are too expensive for these high Reynolds number flows. The adaptive $k-\tau$ model is a compromise between URANS and LES methods. Algebraic subgrid scale models are used to model the unresolved turbulence in LES. By using a non-linear two equation turbulence model based on the model of Craft/Launder/Suga [36],[37] rather than an algebraic model, the adaptive $k-\tau$ model can model a broader range of subgrid scale turbulence. Accordingly, coarser meshes may be used which reduces computational cost.

In the limit of a very coarse grid, the adaptive $k-\tau$ model approaches a RANS simulation. In the limit of a very fine grid in three dimensions with cell Reynolds number length scales approaching the Kolmogorov length scales, it approaches a DNS

[7].

The filtering process in LES and RANS is in principle different; LES filtering is based on a spatial scale determined by the grid (implicit) while RANS filtering is done by time averaging. The adaptive $k-\tau$ model assumes that the implicit filtering in LES becomes, in the limit of high cell Reynolds numbers, similar to the Reynolds time averaging process [7].

The adaptive model breaks the turbulent kinetic energy k and turbulent time scale τ into resolved and unresolved parts:

$$\tau = \tau' + \overline{\tau}, \qquad k = k' + \overline{k} \tag{2.32}$$

The resolved part of the turbulent kinetic energy $\overline{k}$ is part of the numerical solution. The unresolved part k' is modelled with an additional transport equation. The resolved time scale is obtained *a posteriori* using a model for isotropic high Reynolds number flows where $\overline{\tau}$ is determined by the unresolved turbulent kinetic energy k' and the filter length scale L_Δ:

$$\overline{\tau} = \frac{L_\Delta}{\sqrt{k'}} \tag{2.33}$$

The filter length scale (L_Δ) is determined by taking the maximum of the grid length scale (L_S) and the time step or temporal length scale (L_t):

$$L_S = 2 \cdot \sqrt{\Delta x \cdot \Delta y \cdot \Delta z}, \quad L_t = |u| \cdot \Delta t \tag{2.34}$$

$$L_\Delta = \max(L_S, L_t) \tag{2.35}$$

The transport equations for k and τ and the ancillary functions and constants are given in Appendix A. Details of the model can be found in the paper by Magagnato and Gabi [7].

2.6 SPARC and Computational Procedure

The research code SPARC (Structured PArallel Research Code) is used here; the source code is available in exchange for further development and debugging. Though very few modifications are made to the source code in this work, it is being adapted for fluid structure interaction and optimization problems at the University of Victoria. In the spirit of a research code, little documentation is available for SPARC nor are all of its models free of coding errors. This requires that SPARC be thoroughly evaluated in test cases for which there is extensive experimental and numerical data available.

SPARC has been developed by the group of Magagnato [10] at the Department of Fluid Machinery, University of Karlsruhe, Germany. It is intended primarily for turbo machinery flows which are highly turbulent, three-dimensional and unsteady. SPARC is intended to serve as a platform for developing faster and more accurate numerical schemes and better physical models in addition to serving as an engineering tool. This is achieved through the use of parallel computing techniques with multi-block structured grids. SPARC has an extensive set of turbulence models which make it an ideal candidate for many high Reynolds number fluids problems.

SPARC solves the weakly compressible RANS equations for the Spalart Allmaras and Speziale $k-\tau$ turbulence models [32]. The full weakly compressible Navier Stokes equations with implicit filtering set by the grid resolution are solved for the adaptive $k-\tau$ model. The discretization process is a semi-discrete method; discretization is done in two stages. The first stage is a central difference finite volume discretization in space and the second stage is an explicit Runge-Kutta discretization in time. Discretization in space reduces partial differential equations to a set of ordinary differential equations continuous in time.

2.6.1 Artificial Dissipation

When discrete methods are used for high Reynolds number behaviour, scales of motion appear which can not be resolved numerically. These very small scales of motion are caused by non-linear interactions of convection terms in the momentum equations [10]. Representing the scales of motion by frequency, it can be seen that two interacting waves of moderate frequency can multiply to produce a wave of higher frequency (sum of the two original waves) and a wave of lower frequency (difference of the two original waves). While the lower frequency waves are not a problem, the higher frequency waves may represent scales of motion that are too small to be resolved by the grid. Physically, continued cascading of motions into higher and higher frequencies is accounted for by viscous dissipation at very high wave numbers. Numerically, cascading to high frequencies eventually exceeds the grid resolution at which point there may be aliasing back to lower frequencies or piling up of motions at the limit of grid resolution. If uncontrolled, serious inaccuracies or instability can occur [7].

A numerical dissipation term is introduced in the central differencing scheme to account for high frequency cascading. The dissipation term is a blend of second and fourth order differences where the second order differences are designed to prevent oscillations at shock waves in compressible flow and the fourth order terms are designed to improve stability and steady state convergence [10].

For the RANS computations carried out in the first part of this work at $Re_c = 3 \times 10^6$, the artificial dissipation is set to a default value of 1. This is appropriate since these are high Reynolds number steady state simulations. In the second part of the work, unsteady simulations are carried out at $Re_c = 10^5$. Here the artificial dissipation is reduced to 0.3 to obtain unsteady phenomena which were not obtained with the default artificial dissipation of 1. Stability problems are encountered for an artificial dissipation less than 0.3.

2.6.2 Time Stepping

For explicit schemes, the time step is limited by the Courant Friedrich Lewy (CFL) condition. It requires that the domain of dependence of the numerical scheme must at least contain the domain of dependence of the original differential equation. This means that the maximum allowable time step is a function of cell size. For high Reynolds number flows where the viscous phenomena in the boundary layer are resolved, the size ratio between the smallest and largest cells in the computational domain may be of order 10^8 or more. It is very costly then to set the time step based on the smallest cells. In SPARC, local time stepping is used where each cell is advanced in time within its own stability limits [7].

2.6.3 Multigrid

SPARC makes use of multigrid techniques where the solution is transfered to successively coarser grids in order to reduce computational effort per time step and to track the solution evolution on a larger scale so that global equilibrium may be obtained more quickly. Multigrid techniques are found to reduce computing time by a factor of up to ten [7].

The coarser grids are obtained by eliminating every other line in the i, j and k directions in 3D, and in 2D, as used here, in the i and j directions only. A V cycle with the following steps is used to move between the grid levels in SPARC [7]:

- *Smooth* the error on the fine grid.
- Transfer this *solution* and the *residuals* to a coarser grid (*restriction*) and solve on the coarser grid.
- Transfer back the *corrections*, the difference between the transferred solution from the finer grid and and the solution obtained on the coarser grid, to the finer grid by interpolation (*prolongation*).

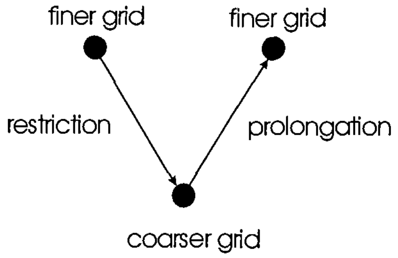

Figure 2.4: Multigrid V Cycle

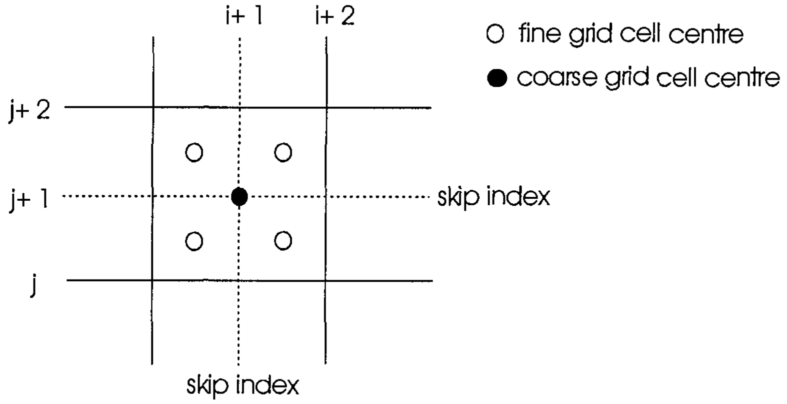

Figure 2.5: Grid coarsening by removal of every other i and j index

2.6.4 Multiblock

SPARC uses the multiblock method. This allows the computational domain to be subdivided into contiguous blocks such that the problem can be tackled by multiple processors. While the computing efficiency is slightly reduced (a few percent) by running in parallel since extra resources are required for information passing between processors, simulations can be completed more quickly. Steady simulation runs with four processors were found to have an efficiency of 95% meaning the solution was completed in about 26% of the time required for a stand alone processor. The grids for steady and unsteady cases in this work are contain 45 blocks which allows simualtions to be run with up to six 1.8 GHz processors.

2.6.5 Shear Stress on the Airfoil Surface

As SPARC does not explicitly calculate the wall shear stresses on the airfoil, it was necessary to write a shear stress calculation routine. Shear stress is proportional to velocity gradient and viscosity at the wall:

$$\tau = (\mu + \mu_t)\frac{\partial u_w}{\partial y_n} \tag{2.36}$$

Here u_w is the velocity along the wall and y_n is the distance normal to the wall. Velocity components for each node are stored in their cartesian components in SPARC, that is, the velocities at a wall node are given in x, y and z components. The coordinates of each node are also stored in this way. To calculate the shear stress, it is necessary to determine the velocity tangential to the wall. This is done by calculating the magnitude of the velocity vector at the first grid point away from the wall. By assuming that the velocity near the wall is tangential to the wall (the flow can not travel into the wall), the magnitude of the velocity vector near the wall should be equal to the tangential velocity. It is straightforward to calculate the normal distance from the wall to the first grid point. Given the tangential velocity at the first node from the wall and the normal distance to the wall, the velocity gradient at the wall can be approximated. The viscosity is calculated as $\mu = \mu + \mu_t$. Because the first node from the wall was usually located at $y^+ < 1$, which is well inside the laminar sublayer, the total viscosity is equal to the laminar viscosity.

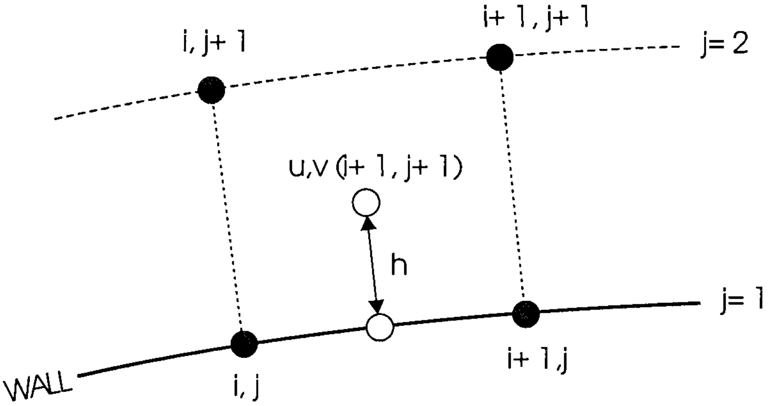

Figure 2.6: Calculation of wall shear stresses

Figure 2.6 shows the grid arrangement near the wall. The velocity components are calculated at the centre of each cell; the grid points define the corners of each cell. To determine the coordinates of the cell centre, it is necessary to interpolate the coordinates of the cell corners. The cell centre coordinates are given as:

$$\begin{aligned} x_{cc} &= \frac{1}{4}\left[x(i,j) + x(i+1,j) + x(i,j+1) + x(i+1,j+1)\right] \\ y_{cc} &= \frac{1}{4}\left[y(i,j) + y(i+1,j) + y(i,j+1) + y(i+1,j+1)\right] \end{aligned} \tag{2.37}$$

The coordinates of the point on the wall perpendicular to the cell centre are:

$$
\begin{aligned}
x_{wc} &= \frac{1}{2}\left[x(i,j) + x(i+1,j)\right] \\
y_{wc} &= \frac{1}{2}\left[y(i,j) + y(i+1,j)\right]
\end{aligned}
\tag{2.38}
$$

The distance h can then be calculated and the total velocity at the cell centre is known such that the shear stress can be approximated as:

$$
h = \sqrt{(x_{cc} - x_{wc})^2 + (y_{cc} - y_{wc})^2}
\tag{2.39}
$$

$$
\tau_{\text{wall}} = (\mu + \mu_t)\frac{\sqrt{u_{i+1,j+1}^2 + v_{i+1,j+1}^2}}{h}
\tag{2.40}
$$

2.7 Summary

In this chapter the Navier Stokes equations and the turbulent time averaging process are presented. Time averaging leads to an additional terms known as the Reynolds stresses which are accounted for by turbulence modelling. The Spalart Allmaras (SA), Speziale $k - \tau$ and adaptive $k - \tau$ turbulence models are presented with their major transport equations. Airfoil nomenclature and the non-dimensional forces such as lift and drag are defined. The research code SPARC is presented, including its parallel multigrid and multiblock methodologies. Airfoil surface shear stress calculations are also discussed.

Chapter 3

Steady Flow Simulations

3.1 Effect of Prescribed Eddy Viscosity

The Spalart Allmaras model has one transport equation for eddy viscosity. It is necessary to determine an appropriate eddy viscosity value for initializing the flow field and for the free stream boundary conditions. In a wind tunnel air is moving before it reaches the airfoil. It has, in addition to the kinetic energy from mean motion, turbulent kinetic energy imposed by the fan; eddy viscosity is thus non-negligible. For an aircraft wing flying through the atmosphere the air is still and the turbulence negligible; it follows that eddy viscosity is also negligible. SPARC does not allow zero values of eddy viscosity. A parametric study is carried out to determine the effect of eddy viscosity on the lift and drag coefficients as well as the shear stress distribution.

Figures 3.1 and 3.2 show the effect of eddy viscosity variation on the pressure distribution C_p along the airfoil surface. Note that for eddy viscosity ratios below 10^{-1}, there is no appreciable difference in the C_p curves. Even for the eddy viscosity

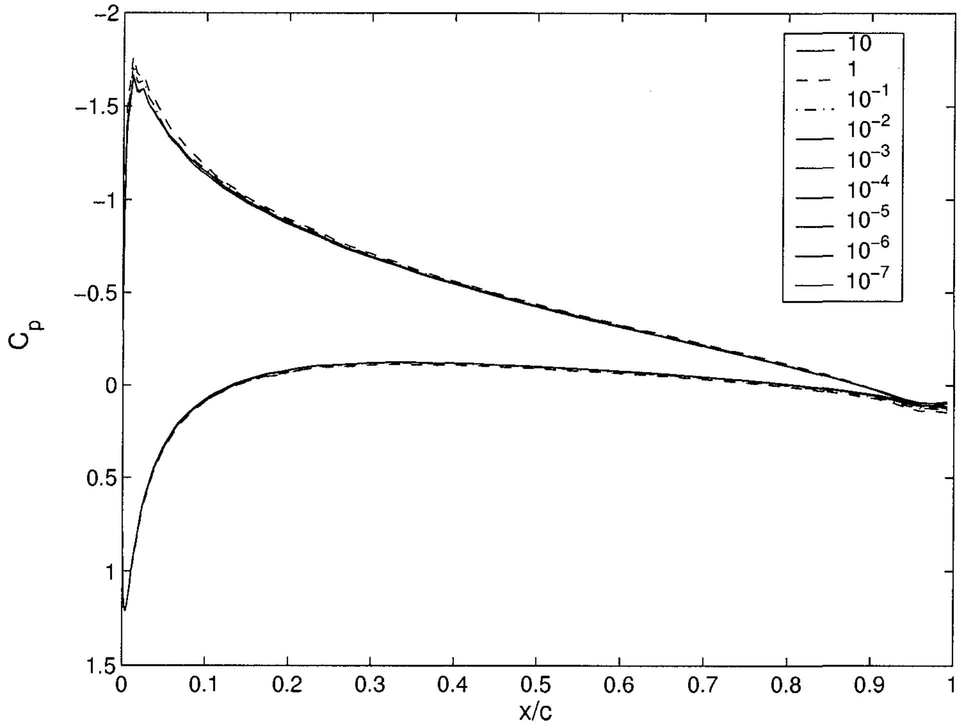

Figure 3.1: Effect of Eddy Viscosity Ratio $\frac{\mu_t}{\mu}$ on NACA 0012 Pressure Distribution for Spalart Allmaras Model at $Re_c = 3 \times 10^6$, $\alpha = 4°$

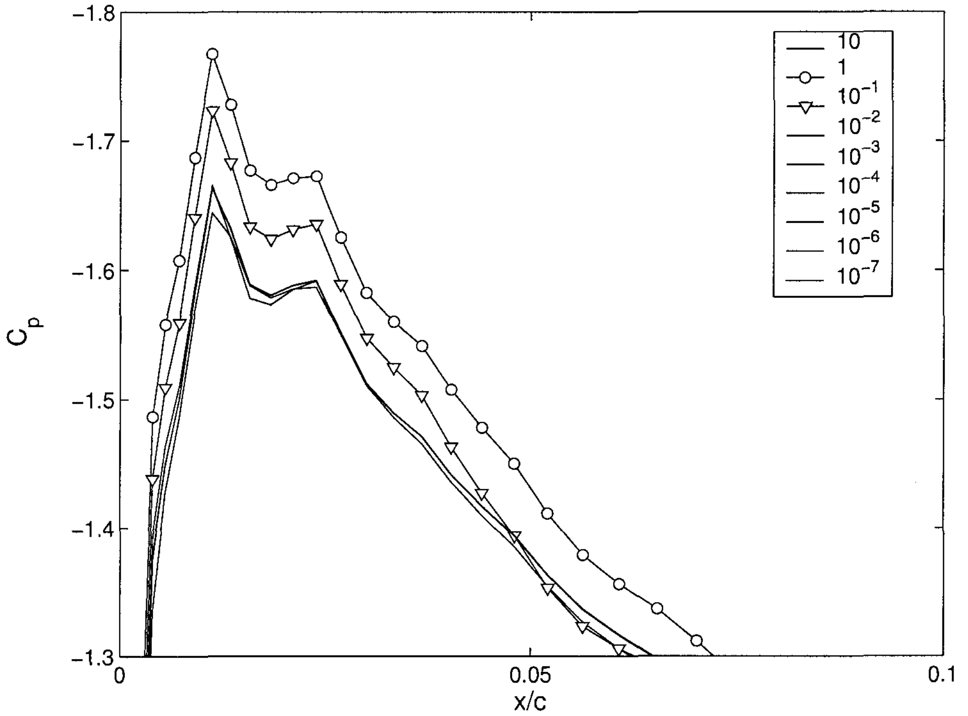

Figure 3.2: Effect of Eddy Viscosity Ratio $\frac{\mu_t}{\mu}$ on NACA 0012 Pressure Distribution for Spalart Allmaras Model at $Re_c = 3 \times 10^6$, $\alpha = 4°$; detail near leading edge on suction side

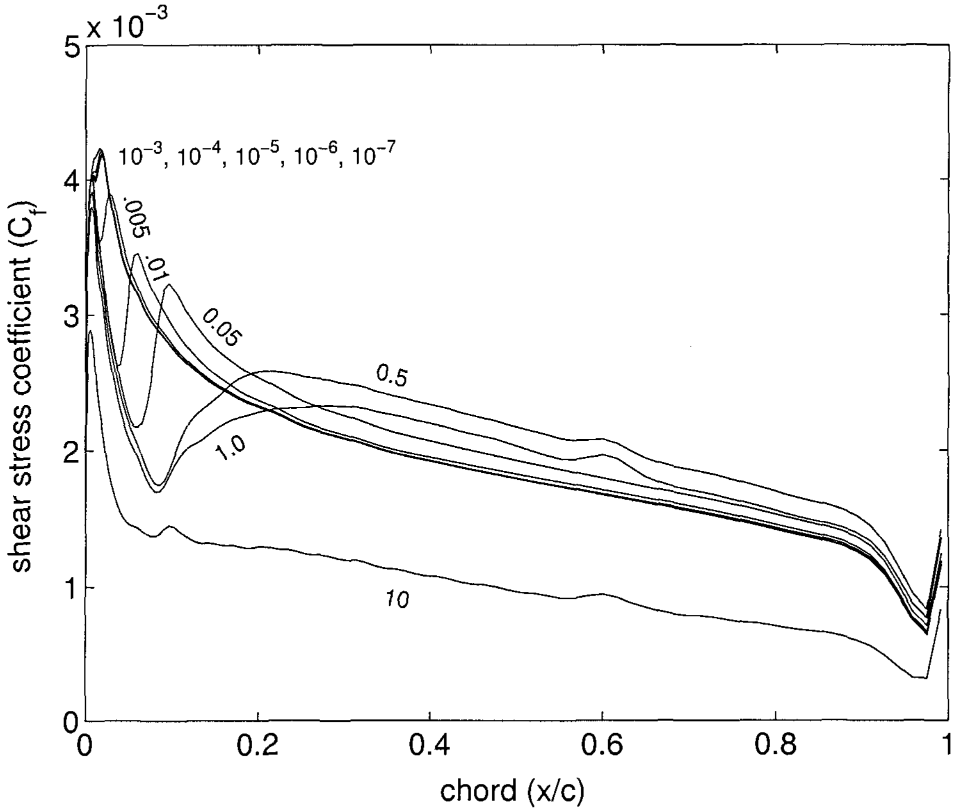

Figure 3.3: Effect of Eddy Viscosity Ratio $\frac{\mu_t}{\mu}$ on NACA 0012 Shear Stress Distribution for Spalart Allmaras Model at $Re_c = 3 \times 10^6$, $\alpha = 0°$. Eddy Viscosity Ratio is shown by number near each curve.

ratios of 1 and 0.1, the only variation in the C_p curves occurs at the leading edge around the suction peak. The small variations in this region are likely associated with the turbulent transition point shown in figures 3.3 through 3.6. Since the pressure distribution is independent of eddy viscosity for $\frac{\mu_t}{\mu} < 0.1$, the coefficients of lift C_l and pressure drag C_{dp} should not be affected in that range. See eddy viscosity study tabular results in Appendix B.

Figures (3.3) and (3.4) show the shear stress distribution for a NACA0012 airfoil at zero and four degree angles of attack at $Re_c = 3 \times 10^6$ for a range of eddy viscosity values. For the low eddy viscosities, transition is very close to $(x/c < 0.05)$ the

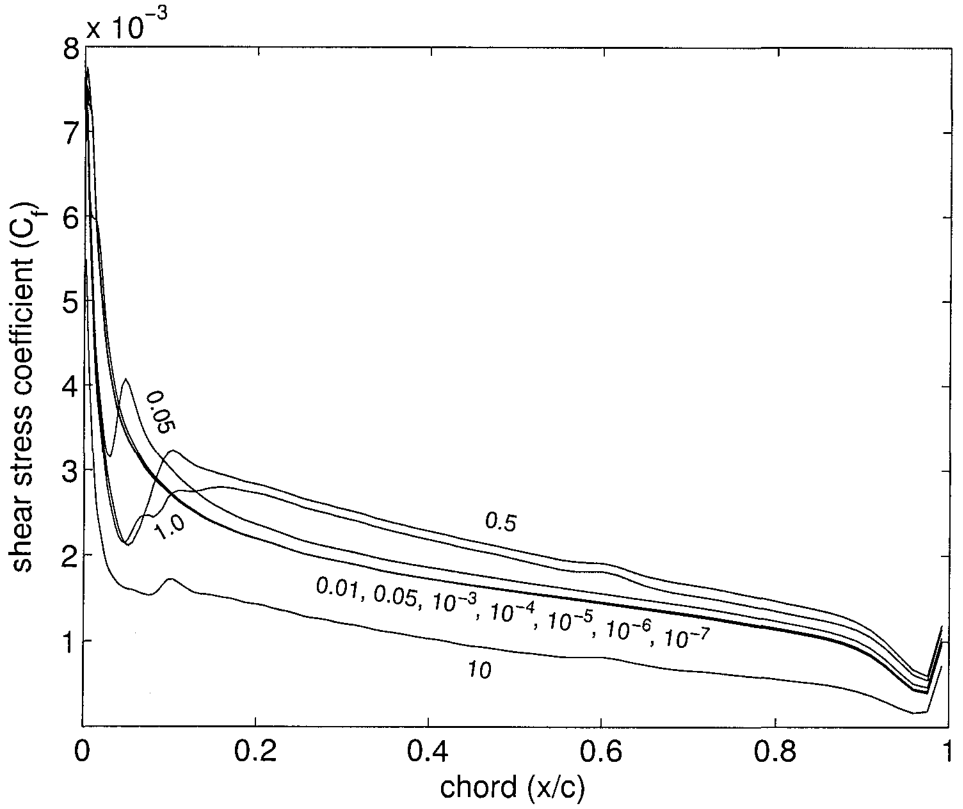

Figure 3.4: Effect of Eddy Viscosity Ratio $\frac{\mu_t}{\mu}$ on NACA 0012 Shear Stress Distribution for Spalart Allmaras Model at $Re_c = 3 \times 10^6$, $\alpha = 4°$. Eddy Viscosity Ratio is shown by number near each curve.

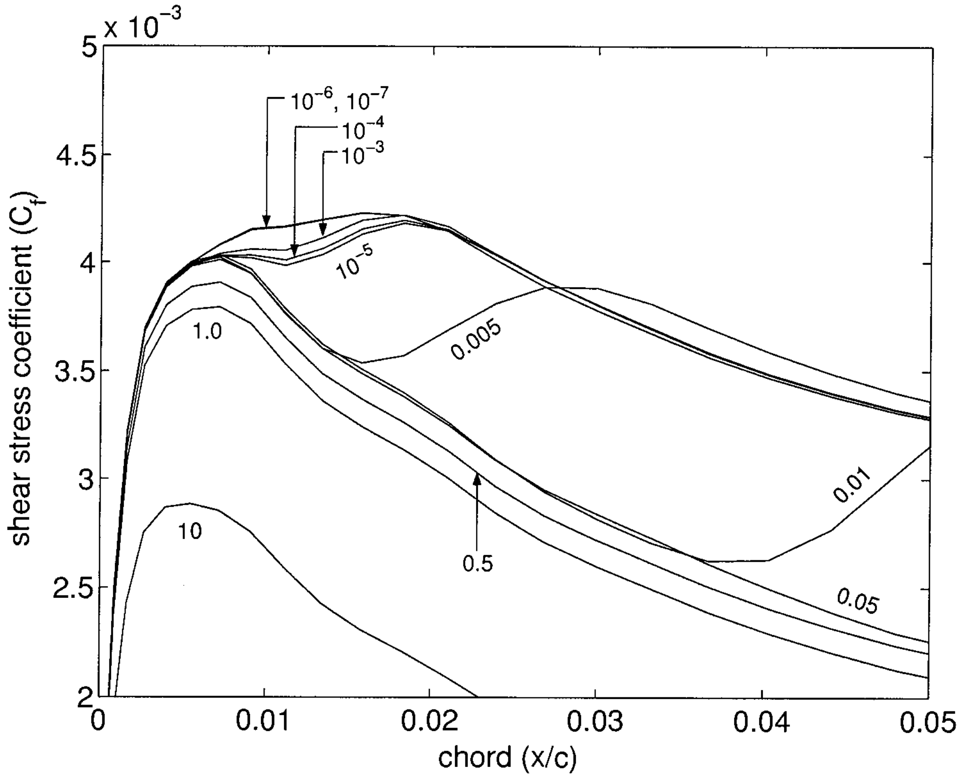

Figure 3.5: Effect of Eddy Viscosity Ratio $\frac{\mu_t}{\mu}$ on NACA 0012 Shear Stress Distribution for Spalart Allmaras Model at $Re_c = 3 \times 10^6$, $\alpha = 0°$; detail near leading edge. Eddy Viscosity Ratio is shown by number near each curve.

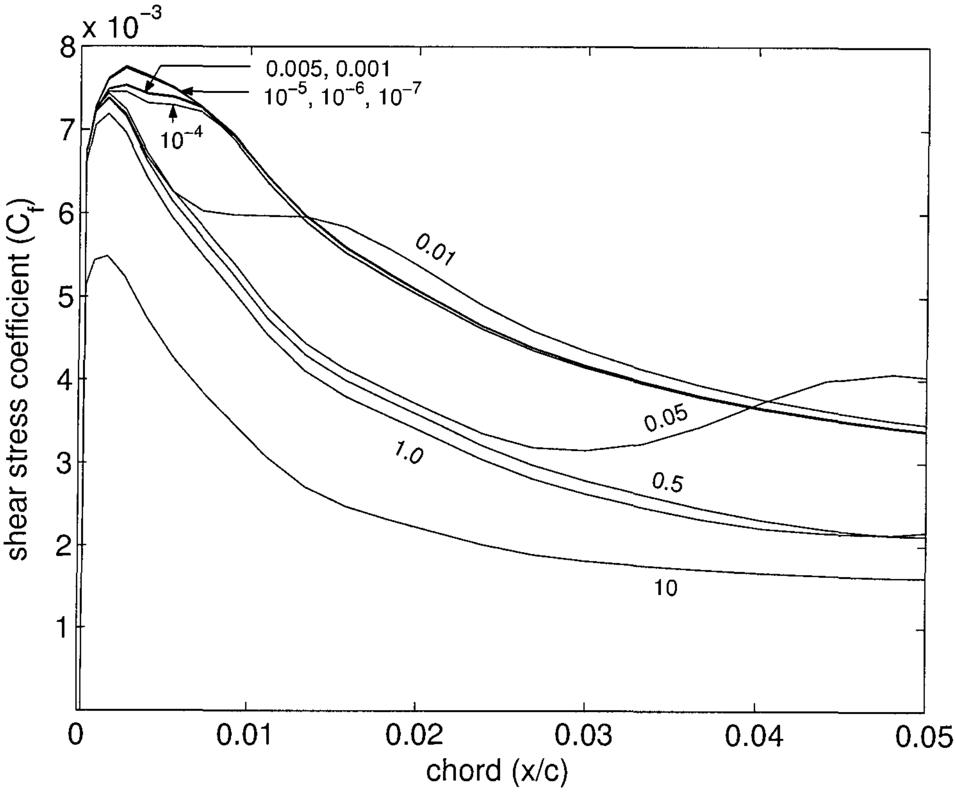

Figure 3.6: Effect of Eddy Viscosity Ratio $\frac{\mu_t}{\mu}$ on NACA 0012 Shear Stress Distribution for Spalart Allmaras Model at $Re_c = 3 \times 10^6$, $\alpha = 4°$; detail near leading edge. Eddy Viscosity Ratio is shown by number near each curve.

leading edge. Transition is difficult to see for the eddy viscosity of 0.001; it is a slight indentation in the upper curve just before it peaks at about $x/c = 0.01$. The transition point is more easily distinguished for the eddy viscosity ratios of 0.005, 0.01 and 0.05; it occurs at the bottom of the trough from $x/c = 0.02$ to $x/c = 0.1$. Transition to turbulence causes an increase in shear stress. The initial peak in shear stress occurs for all of the eddy viscosities at the leading edge; this is due to the high velocity gradients in this region. At the stagnation point where $x = 0$, $y = 0$, the velocity must be zero for $\alpha = 0°$. There is a strong favourable pressure gradient in this region due to the high curvature near the leading edge; the velocity near the wall quickly increases when moving along the wall away from the stagnation point. Continuing along the wall, the curvature decreases and the pressure gradient becomes adverse.

If the flow were to remain laminar to the trailing edge, the shear stress would gradually slope down with increasing chord due to the increasing width of the boundary layer and very slight adverse pressure gradient. This behaviour is shown by the curve for $\frac{\mu_t}{\mu} = 10$. Intuitively, the shear stress could be expected to increase with increasing eddy viscosity; a high eddy viscosity implies that there is a large amount of turbulence present. The total viscosity is the sum of the laminar and turbulent viscosities: $\mu = \mu + \mu_t$. Setting an artificially high eddy viscosity ratio at the boundaries effectively lowers the Reynolds number $Re_c = \frac{\rho U c}{\mu}$ and therefore stabilizes the flow. This may explain why there is no apparent transition to turbulence and the shear stress is lower for an eddy viscosity ratio of 10.

For either $\alpha = 0°$ or $\alpha = 4°$, decreasing the inlet eddy viscosity ratio below 10^{-6} has no appreciable effect on the shear stress curve. Even the eddy viscosity curve for 10^{-3} shows only minor differences from the 10^{-6} curve at the shear stress peak near the leading edge.

Spalart and Allmaras [21] recommend that the free stream eddy viscosity and the initial eddy viscosity be set to zero, or, if this is not possible, as it is not in SPARC, they recommend setting the working variable in Spalart Allmaras (SA) model eddy viscosity transport equation to $\tilde{\nu} < \frac{\nu}{10}$. Working backward, the appropriate restriction on the eddy viscosity ratio $\frac{\nu_t}{\nu}$ for the initial and free stream conditions can be determined. In the SA model, the eddy viscosity is given as:

$$\nu_t = \tilde{\nu} f_{v1}, \qquad f_{v1} = \frac{\chi^3}{\chi^3 + C_{v1}^3}, \qquad \chi \equiv \frac{\tilde{\nu}}{\nu} \tag{3.1}$$

Spalart and Allmaras [21] give a value of $C_{v1} = 7.1$. Adding equations (3.1), ν_t can be written in terms of ν_l:

$$\nu_t = \tilde{\nu} \left[\frac{\left(\frac{\tilde{\nu}}{\nu}\right)^3}{\left(\frac{\tilde{\nu}}{\nu}\right)^3 + C_{v1}^3} \right] \tag{3.2}$$

Let $\tilde{\nu} = \frac{\nu}{10}$, then:

$$\nu_t = \frac{\frac{\nu}{10^4}}{\left(\frac{1}{10}\right)^3 + C_{v1}^3} \tag{3.3}$$

Note that $C_{v1}^3 = 7.1^3 \gg \left(\frac{1}{10}\right)^3$, therefore the $\left(\frac{1}{10}\right)^3$ term can be dropped. Substituting for C_{v1}^3 and re-arranging,

$$\frac{\nu_t}{\nu} \cong 2.8 \times 10^{-6} \tag{3.4}$$

The eddy viscosity ratio $\frac{\nu_t}{\nu}$ should then be set to 10^{-7} or less in the free stream and at the inlet.

3.2 Grid Study

A grid study for $\alpha = 0°$ and $\alpha = 4°$ using a free stream and initial eddy viscosity of $\frac{\mu_t}{\mu} = 10^{-7}$ was carried out. One of the difficulties is that as the grid is refined, the behaviour of the turbulence model changes. The grid that gives the most physically plausible results is not necessarily the finest. An evolution study of 35 different grids has resulted in the two grids presented here. Grids airfoil32 and airfoil35 are presented; airfoil35 is a refined version of airfoil32 with more grid points normal to the wall for better resolution of the viscous sub-layer and more grid points tangential to the wall in high pressure and velocity gradient regions at the leading and trailing edges.

Tables 3.1 through 3.5 show the lift (C_l), total drag (C_d), friction drag (C_{df}) and pressure drag (C_{dp}) for the grids airfoil32 and airfoil35. The effects of doubling grid resolution are shown. 2X wall means the wall block grid has been refined once, that is, the wall block grid resolution has been doubled. 2X global means that all of the blocks (the entire domain) have been refined once, i.e. the entire grid resolution has been doubled. 4X means the grid resolution has been doubled a second time. The first column denotes the grid level; grid level one is the coarsest grid, grid level two has double the resolution of grid level one and grid level three (the finest grid) has double the resolution of grid level two.

Comparing the lift and drag coefficients between the grid levels gives an estimate of the necessary grid resolution for a grid independent solution. Looking at the coefficient of lift C_l in column three of table 3.2, it can be seen that C_l is changing by about 0.09 or 2 percent between each grid level. While this is not too dramatic, doubling the grid resolution in the wall blocks leads to an increase of C_l from 0.421 to 0.442. Further doubling in the wall block resolution results in a C_l increase from

grid level		base	2X wall	4X wall	2X global
1	C_l	0.00188	-0.00028	-0.00031	0.00146
	C_d	0.0106	0.00928	0.00620	0.00598
	C_{df}	0.00042	0.00080	0.00150	0.00077
	C_{dp}	0.0101	0.00848	0.00470	0.00521
2	C_l	0.00112	-0.00034	-0.00042	0.00061
	C_d	0.00590	0.00608	0.00545	0.00473
	C_{df}	0.00082	0.00159	0.00262	0.00157
	C_{dp}	0.00508	0.00449	0.00283	0.00316
3	C_l	0.00056	-0.00034	-0.00034	0.00028
	C_d	0.00476	0.00550	0.00526	0.00474
	C_{df}	0.00161	0.00268	0.00320	0.00265
	C_{dp}	0.00315	0.00282	0.00206	0.00209

Table 3.1: NACA 0012 Grid airfoil32 and variations for $\alpha = 0°$, $Re_c = 3 \times 10^6$

grid level		base	2X wall	4X wall	2X global
1	C_l	0.403	0.431	0.431	0.413
	C_d	0.0162	0.0136	0.00880	0.00873
	C_{df}	0.00037	0.00073	0.00136	0.00070
	C_{dp}	0.0158	0.0129	0.00744	0.00803
2	C_l	0.412	0.436	0.438	0.421
	C_d	0.00854	0.00822	0.00689	0.00643
	C_{df}	0.00074	0.00144	0.00245	0.00142
	C_{dp}	0.00780	0.00678	0.00443	0.00501
3	C_l	0.421	0.442	0.445	0.431
	C_d	0.00643	0.00675	0.00615	0.00590
	C_{df}	0.00146	0.00251	0.00313	0.00243
	C_{dp}	0.00497	0.00424	0.00302	0.00347

Table 3.2: NACA 0012 Grid airfoil32 and variations for $\alpha = 4°$, $Re_c = 3 \times 10^6$

0.442 to 0.445 or 0.7%. Clearly the second doubling of the wall block resolution is not necessary for a grid independent C_l. The total drag C_d should not be used in the grid study since it does not behave monotonically. With an increasingly refined grid C_d initially decreases and then increases before decreasing again. Total drag C_d is the combination of pressure (form) drag C_{dp} and viscous (friction) drag C_{df}:

$$C_d = C_{df} + C_{dp} \tag{3.5}$$

The components of drag should be reviewed independently as they are calculated independently in SPARC. Looking at column 1 for the base grid in tables 3.1 and 3.2, the friction drag C_{df} is under predicted for coarse grids and the pressure drag C_{dp} is over predicted. The grid is too coarse to properly resolve the laminar sublayer and the velocity gradient at the wall. Further, the pressure drag is over predicted since the mesh is quite coarse at the leading edge; the curvature of the airfoil is not well resolved. When the grid resolution in the wall blocks at grid level three is doubled, C_{df} increases by 66% for $\alpha = 0°$ and 72% for $\alpha = 4°$; the airfoil32 base grid is clearly too coarse to properly calculate the wall friction. Pressure drag C_{dp} also changes, although not as severely as friction drag, when the wall block resolution is doubled. C_{dp} changes from 0.00315 to 0.00282 (10%) for $\alpha = 0°$ and from 0.00497 to 0.00424 (15%) for $\alpha = 4°$. There is a similar change when the wall block grid is doubled for a second time; see column 5. The grid airfoil35 attempts to better resolve the friction drag by increasing the number of grid points normal to the wall and increasing the tangential resolution near the leading and trailing edges. Table 3.3 summarizes the revision of grid airfoil32 in grid airfoil35. The number of points for leading edge(LE), middle edge(ME) and trailing edge(TE) blocks is listed as well as the distance y_1 of the first grid point from the wall.

Tables 3.4 and 3.5 show the grid study results for the refined grid airfoil35. Note

grid	points	LE x	ME x	TE x	total x	total y	y_1 (m)
airfoil32	58752	65	49	25	137	137	5.0×10^{-5}
airfoil35	78144	97	65	33	193	149	2.5×10^{-5}
airfoil35 wall 2X	130368	193	129	65	385	213	1.25×10^{-5}

Table 3.3: Refinements from grid airfoil32 to airfoil35; LE=leading edge, ME=middle edge, TE=trailing edge, y_1=distance of first grid point from wall. Airfoil35 wall 2X has a doubled grid resolution in wall blocks, all other blocks are identical to airfoil35.

grid level		base	2X wall	4X wall	2X global	2X domain
1	C_l	0.0001	-0.00052	0.0574	0.00033	-0.00028
	C_d	0.00586	0.00653	0.00445	0.00469	0.00652
	C_{df}	0.00079	0.00149	0.0059	0.00147	0.00149
	C_{dp}	0.00507	0.00504	0.00387	0.00322	0.00503
2	C_l	0.00013	0.00016	divg	0.00013	-0.00006
	C_d	0.00475	0.00557	divg	0.00474	0.00556
	C_{df}	0.00158	0.00266	divg	0.00264	0.00266
	C_{dp}	0.00317	0.00291	divg	0.00210	0.00291
3	C_l	0.00007	-0.00014	n/a	0.00008	-0.00009
	C_d	0.00481	0.00532	n/a	0.00492	0.00532
	C_{df}	0.00272	0.00326	n/a	0.00325	0.00266
	C_{dp}	0.00209	0.00206	n/a	0.00168	0.00291

Table 3.4: NACA 0012 Grid airfoil35 and variations for $\alpha = 0°$, $Re_c = 3 \times 10^6$

that it is necessary to run the grid study for both $\alpha = 0°$ and $\alpha = 4°$. At $\alpha = 0°$, the lift should be zero since the NACA 0012 is a symmetric airfoil. Modelling and discretization errors give a very small value of lift that can be neglected. The pressure drag C_{dp} at $\alpha = 0°$ is small compared to an airfoil generating lift. The proportion of friction drag to total drag C_{df}/C_d is largest for $\alpha = 0°$; this makes the zero angle of attack a good configuration for verifying that the grid resolution is adequate for properly resolving the friction drag. Because the pressure drag is small and the lift is zero for $\alpha = 0°$, a four degree angle of attack is also used to provide a large enough value of C_l for comparison between grids.

Following the coefficient of lift C_l at $\alpha = 4°$ for the base grid in table 3.5, the values

grid level		base	2X wall	4X wall	2X global	2X domain
1	C_l	0.411	0.430	0.439	0.417	0.432
	C_d	0.00820	0.00898	0.00773	0.00639	0.00884
	C_{df}	0.00072	0.00136	0.00237	0.00134	0.00136
	C_{dp}	0.00747	0.00762	0.00535	0.00506	0.00749
2	C_l	0.418	0.439	0.440	0.430	0.441
	C_d	0.00637	0.00691	0.00658	0.00588	0.00677
	C_{df}	0.00143	0.00249	0.00312	0.00247	0.00249
	C_{dp}	0.00494	0.00441	0.00346	0.00341	0.00428
3	C_l	0.430	0.442	0.442	0.436	0.444
	C_d	0.00593	0.00625	0.00583	0.00587	0.00613
	C_{df}	0.00255	0.00319	0.00321	0.00318	0.00319
	C_{dp}	0.00338	0.00306	0.00262	0.00270	0.00294

Table 3.5: NACA 0012 Grid airfoil35 and variations for $\alpha = 4°$, $Re_c = 3 \times 10^6$

continue to change through each grid level from 0.411 to 0.418 to 0.430. Doubling the resolution of the wall blocks gives a C_l of 0.442; doubling a second time results in no change, C_l remains at 0.442. Grid airfoil35 with the resolution in the wall blocks doubled is clearly adequate. Looking at the friction drag C_{df} for base grid level three, C_{df} changes from 0.00255 to 0.00319 (25%) when the wall block resolution is doubled; when the resolution is doubled again, C_{df} changes from 0.00319 to 0.00321 (0.6%) Again, the airfoil35 grid with a single doubling of the wall block resolution appears adequate for predicting friction drag. Similar results occur when the entire grid resolution is doubled; it is more practical to refine only the wall blocks thereby reducing the total number of grid points. The doubled wall block grid has 130,368 grid points, the doubled global grid has 312,576 points.

The results for pressure drag C_{dp} are not quite as convincing as the lift and friction drag results. In the interest of using a reasonable number of grid points, the grid airfoil35 with one wall block refinement is deemed sufficiently accurate. Looking at C_{dp} for the base grid at $\alpha = 4^o$, values change from 0.00494 to 0.00338 (32%) from grid levels two to three and from 0.00338 to 0.00306 (9%) for one wall block refinement. A further wall block refinement changes C_{dp} from 0.00306 to 0.00262 (14%). Doubling the entire base grid at grid level three changes C_{dp} from 0.00338 to 0.00270 (20%). Further refinements will not result in an increase in friction drag. They will result in a small reduction in pressure drag but the total drag is already somewhat lower than experimental results. The small gain in numerical accuracy would probably not justify further refinements, especially when the results for lift C_l are very good. The calculated drag at $\alpha = 4°$ ($C_d = 0.00625$) is already lower than the experimental value ($C_d = 0.0066$) of Abbott [38].

Figures 3.7 and 3.8 show y^+ values for the first grid point away from the airfoil surface for the $\alpha = 0°$ and $\alpha = 4°$ test cases. It is well documented that for proper resolution of the laminar sublayer and prediction of the wall shear stresses, the first grid point away from the wall should be located at $y^+ \leq 1$ when wall functions are not used [39] [16] [40]. Clearly the base grid does not meet this requirement; refinement at the wall is required. Doubling the grid points in the wall blocks meets the y^+ requirement over most of the airfoil surface.

Another factor that can influence the accuracy of the numerical solution is the size of the computational domain. To test the domain size, an additional row of blocks was added increasing the domain width from 40 to 80 chord lengths in the cross stream (y) direction and the inlet length from 20 to 40 chord lengths in the x direction. The results for the large domain with the grid refined once in the wall blocks are shown in the far right column of tables 3.4 and 3.5. Comparing the lift and drag values with the results in column 4 (1X wall) for $\alpha = 4°$, the lift coefficient C_l changes from 0.442 to 0.444 (0.5%), the friction drag coefficient C_{df} changes from 0.00319 to 0.00318 (0.3%). The domain increase has a negligible effect on these values. The pressure drag coefficient C_{dp} changes from 0.00306 to 0.00294 (4%). While this

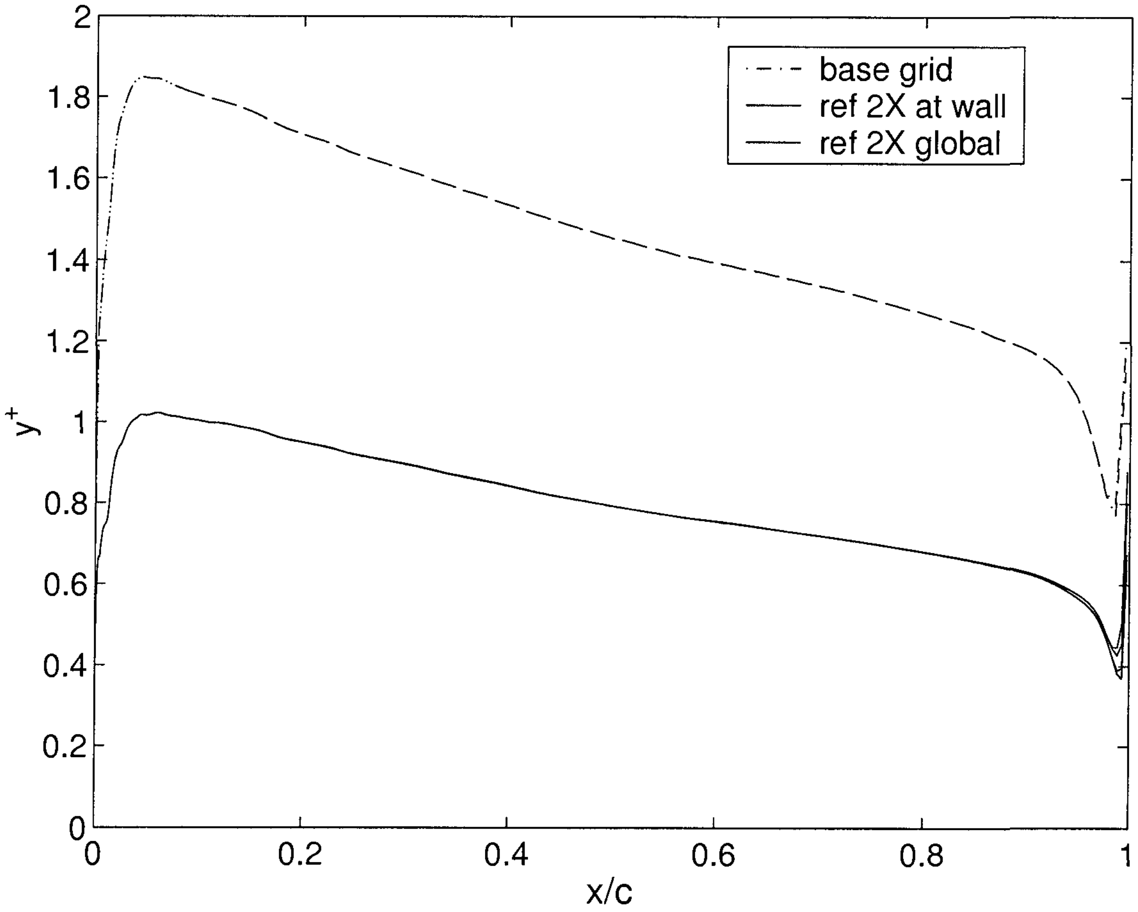

Figure 3.7: NACA 0012 Spalart Allmaras model y^+ values for the first grid point from the wall in the grid study for airfoil35 at $\alpha = 0°$; doubling the resolution at the wall and globally have the same effect on y^+

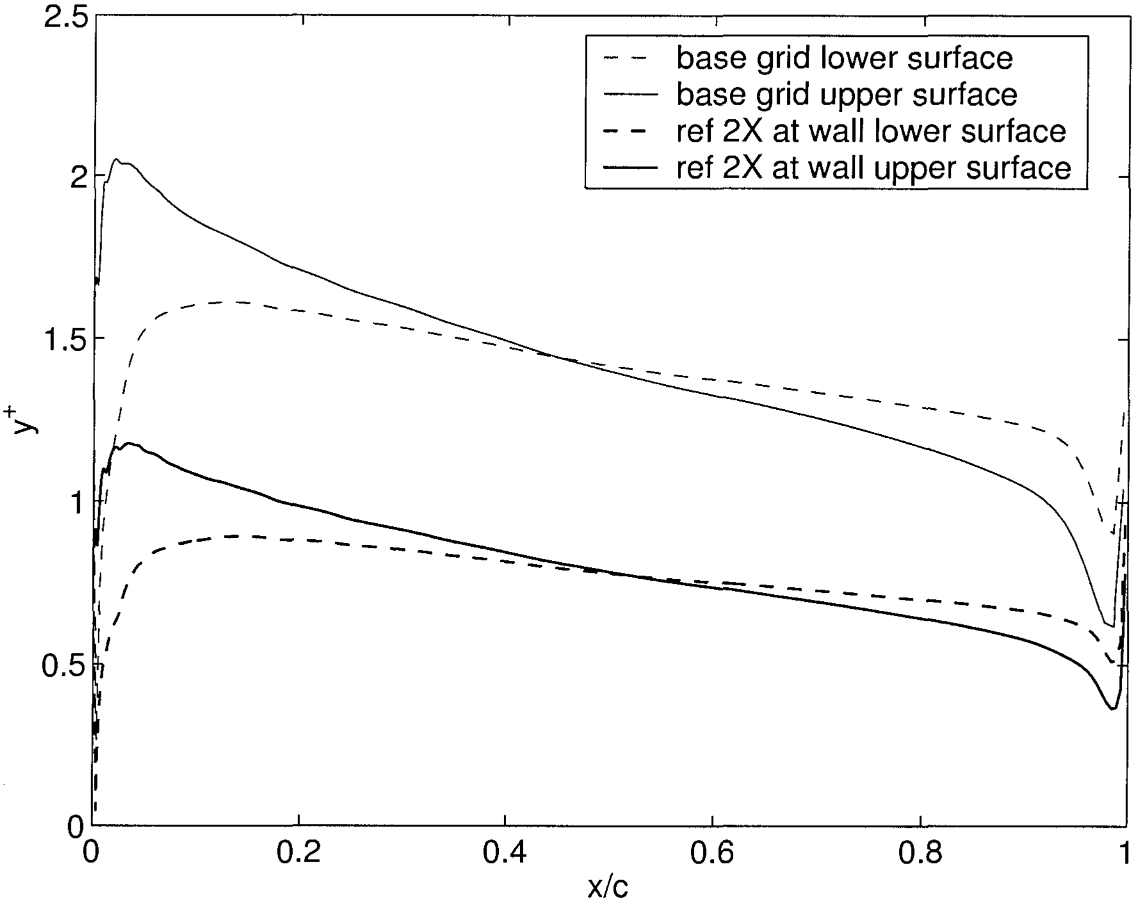

Figure 3.8: NACA 0012 Spalart Allmaras model y^+ values for the first grid point from the wall in the grid study for airfoil35 at $\alpha = 4°$

change is slightly more aggressive than the changes for the other coefficients, it is not large enough to justify the additional computational expense of a larger domain.

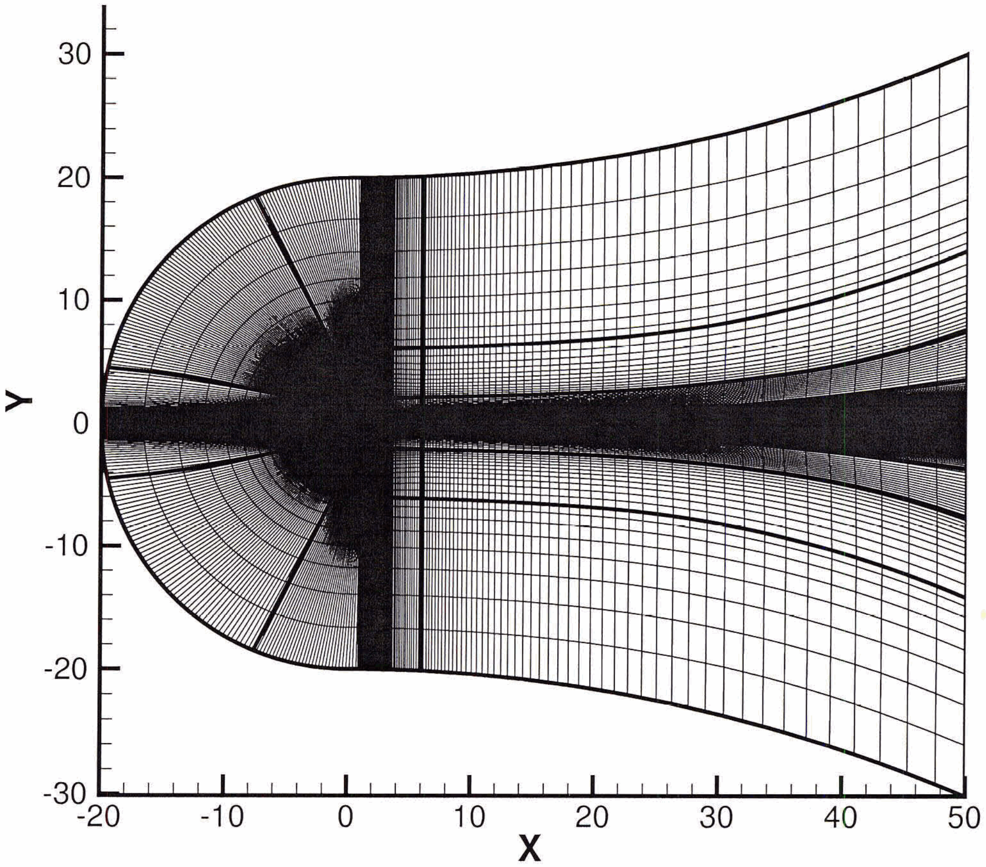

Figure 3.9: NACA 0012 Grid airfoil35, 78144 grid points

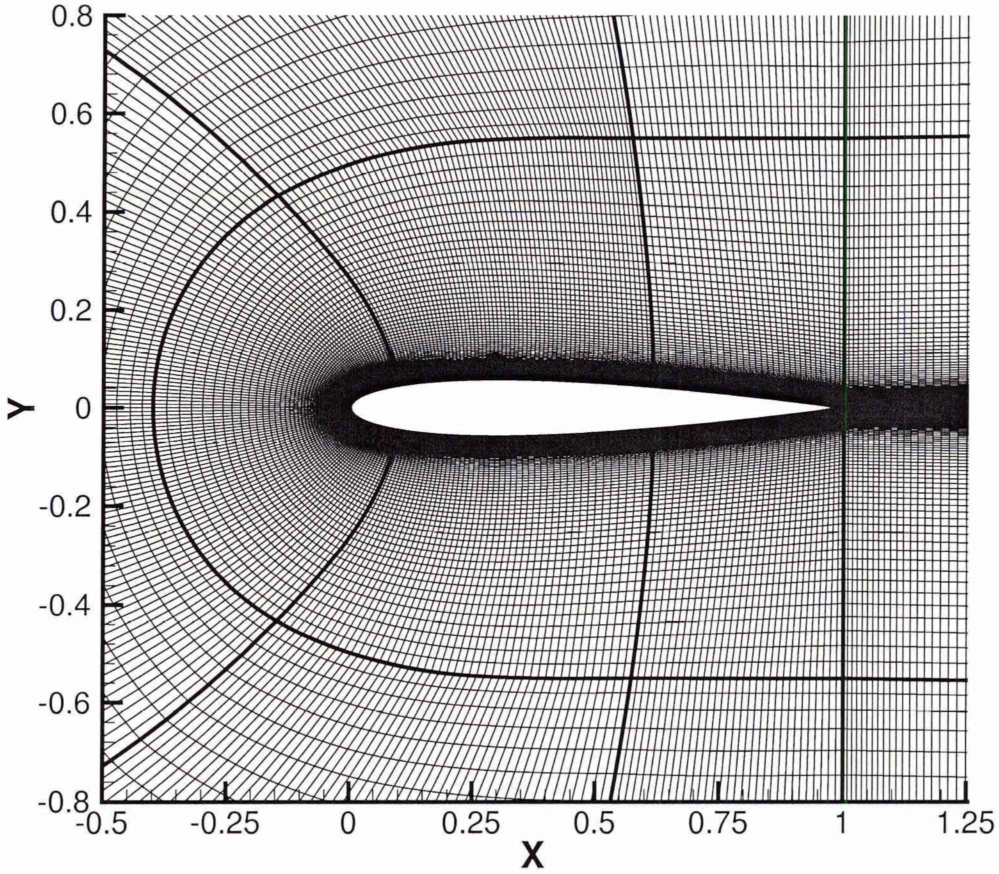

Figure 3.10: NACA 0012 Grid airfoil35, detail near airfoil, 78144 grid points

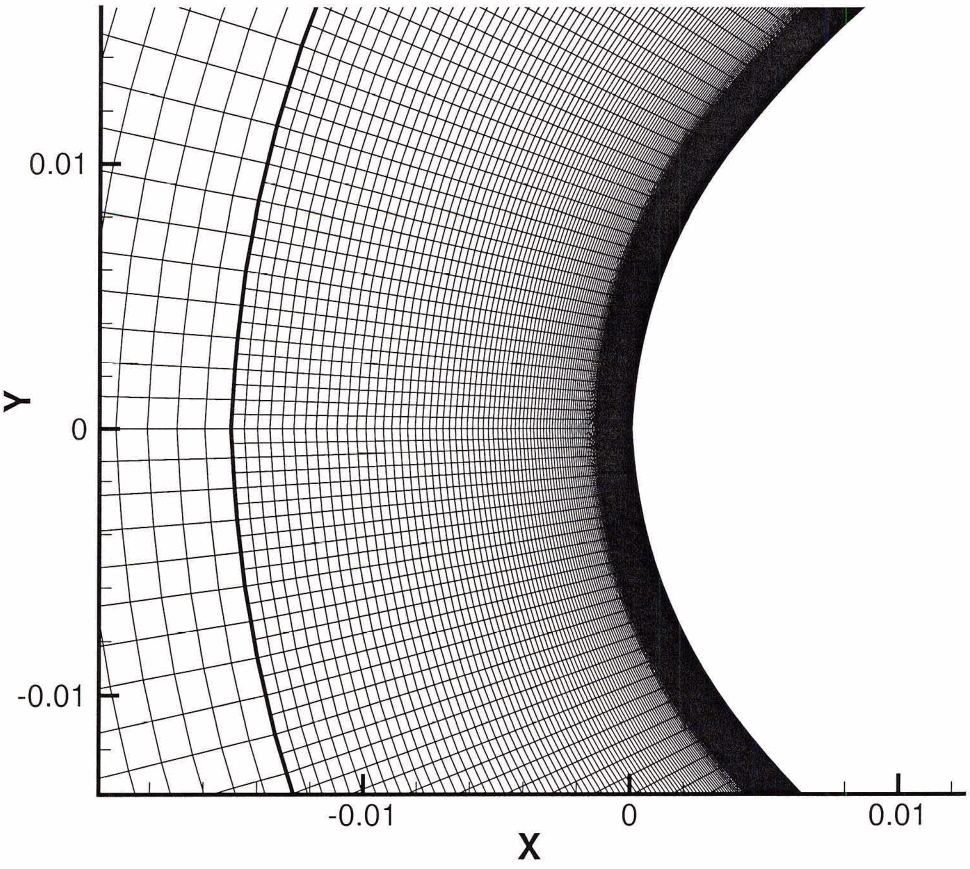

Figure 3.11: NACA 0012 Grid airfoil35, doubled resolution of wall blocks, 130368 grid points

3.3 Spalart Allmaras

Results of steady state simulations for the NACA 0012 airfoil using the Spalart Allmaras turbulence model are presented in this section. The Reynolds number is set at $Re_c = 3 \times 10^6$ and angles of attack vary from $\alpha = 0°$ to $\alpha = 18°$. Note that the same grid is used for all angles of attack; the angle of attack is varied by changing the angle of the free stream at the far field boundaries and in the domain initialization. The angle of attack is shown in the upper right hand corner of each plot in the figures; the contour legend applies to all plots below it.

Pressure coefficient (C_p) contours are shown in figure 3.12. The pressure field is symmetric for $\alpha = 0°$ with a pressure peak at the leading edge stagnation point $x/c = 0$, low pressure areas along the upper and lower surfaces of the airfoil between $x/c = 0.05$ and $x/c = 0.8$ and a trailing edge pressure peak. With increasing angle of attack, the stagnation point moves along the lower surface of the airfoil while the low pressure area on the upper surface becomes increasingly pronounced. Pressure peaks at the higher angles of attack exceed the contour scale; the scale is set to avoid too few contours in the low angle of attack plots.

The airfoil surface pressure distribution is shown in figure 3.13. The curves are shifted in the x/c direction by $0.05\alpha°$ such that the data for multiple angles of attack can be displayed in one plot. The magnitude and shape of the curves agree very closely (within 2%) with the experimental work of Gregory [30].

Eddy viscosity ratio ($\frac{\mu_t}{\mu}$) contours are presented in figures 3.14 and 3.15. For $\alpha = 0°$, an eddy viscosity ratio of approximately 100 develops in the boundary layer on either side of the airfoil in the adverse pressure gradient region downstream of $x/c = 0.4$. The eddy viscosity develops further in the downstream wake, reaching a value of $\frac{\mu_t}{\mu} = 350$ at $x/c = 1.5$. The eddy viscosity ratio in the wake increases with

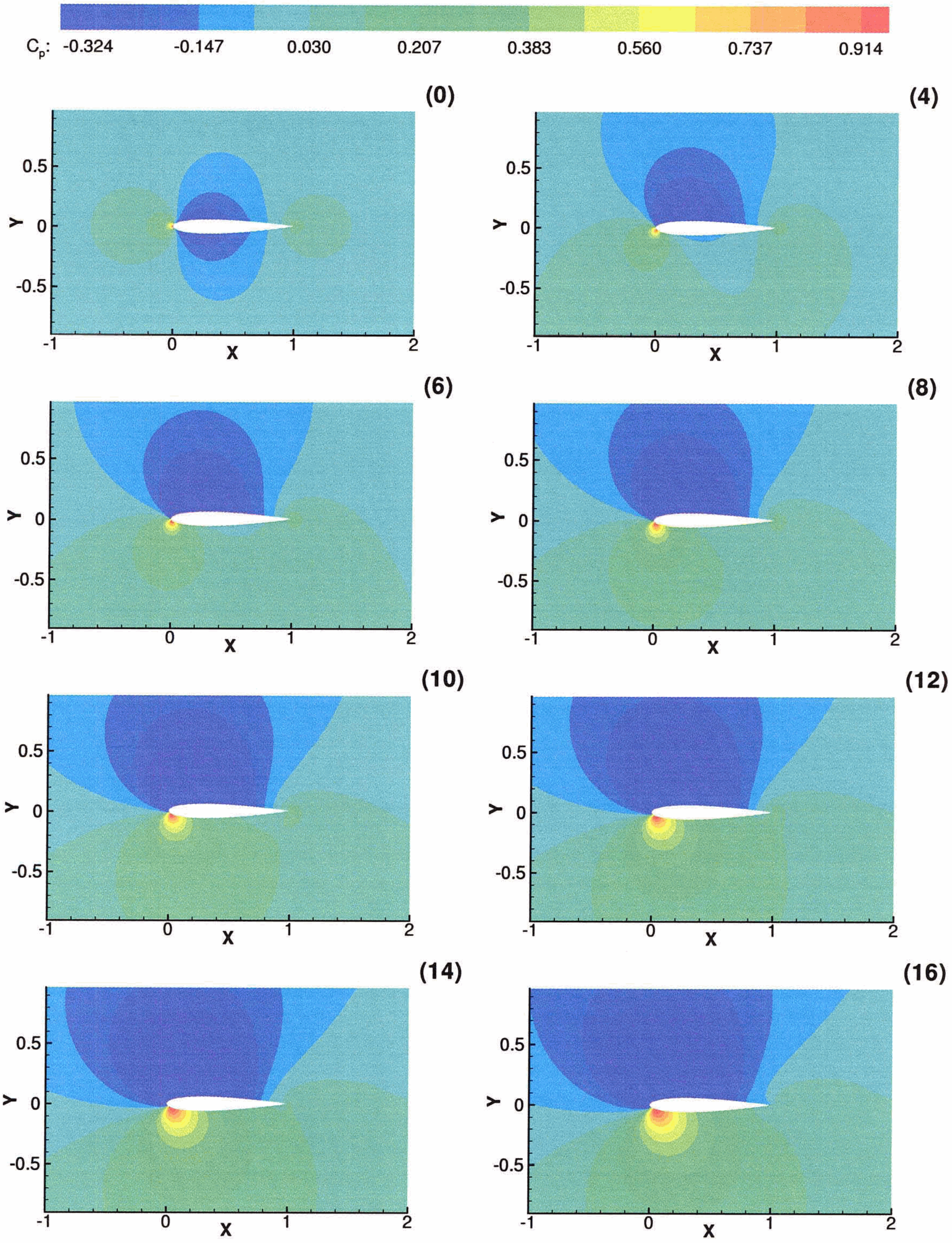

Figure 3.12: NACA 0012 Spalart Allmaras model pressure contours (C_p) at $Re_c = 3 \times 10^6$ for $\alpha = 0°$ to $\alpha = 16°$

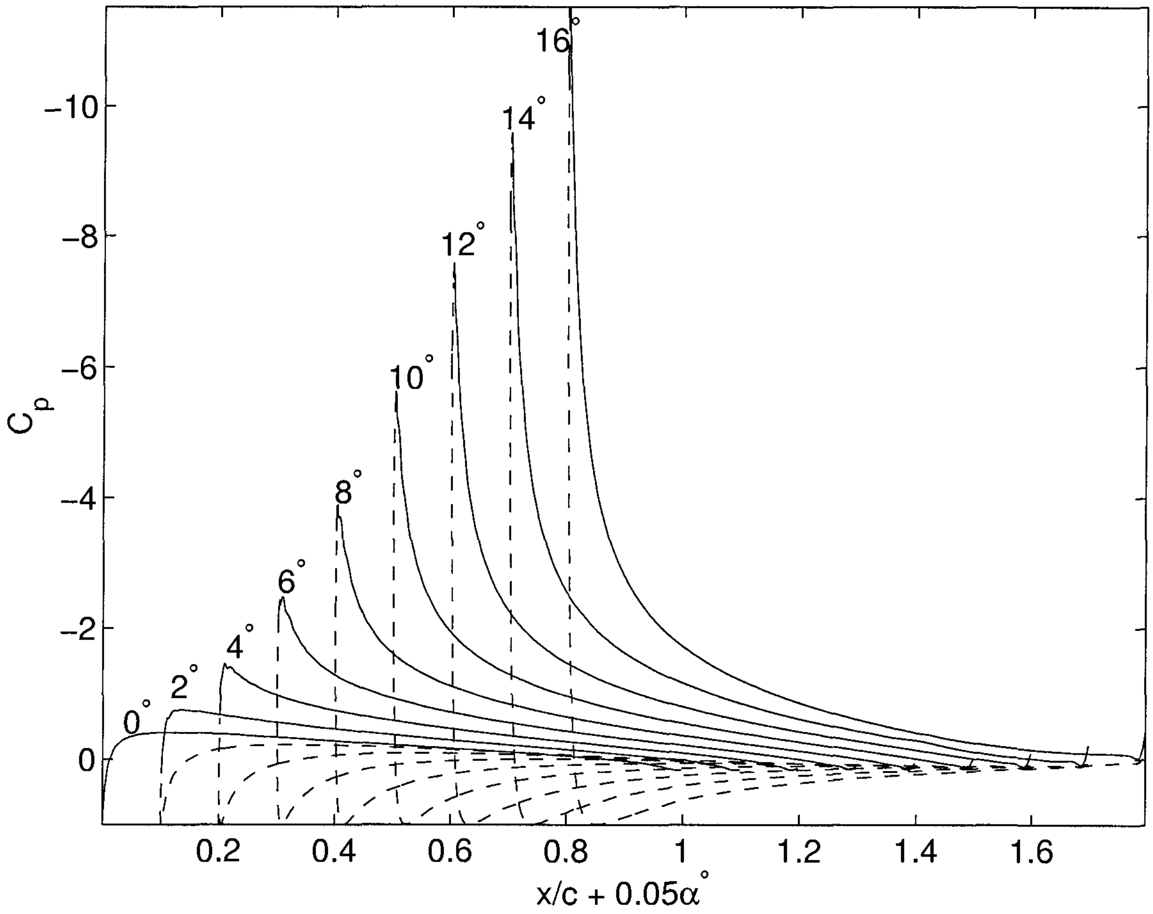

Figure 3.13: NACA 0012 Spalart Allmaras model airfoil surface pressure distribution $Re_c = 3 \times 10^6$ for selected angles of attack from $\alpha = 0°$ to $\alpha = 16°$; the lower surface is in dashed lines, the upper surface is in solid lines

increasing α.

Flow separation begins at the trailing edge at $\alpha = 15^\circ$. This is marked by a significant jump in the eddy viscosity ratio in the separated region and in the wake; see figure 3.15 at $\alpha = 15^\circ,\ 16^\circ,\ 17^\circ$. Before separation at $\alpha = 14^\circ$, the eddy viscosity ratio in the wake is 1000; it doubles to over 2000 at $\alpha = 17^\circ$.

Velocity stream lines are shown in figure 3.16. A trailing edge separation bubble is clearly visible at $\alpha = 16^\circ$. It continues to grow towards the leading edge with increasing α. Note that steady state results could not be obtained for $\alpha > 16^\circ$. The contour plots shown for $\alpha = 17^\circ$ and 18° were obtained just before the solution diverged; they are included for illustrative purposes as the divergence was likely caused by the beginning of unsteady vortex shedding phenomena.

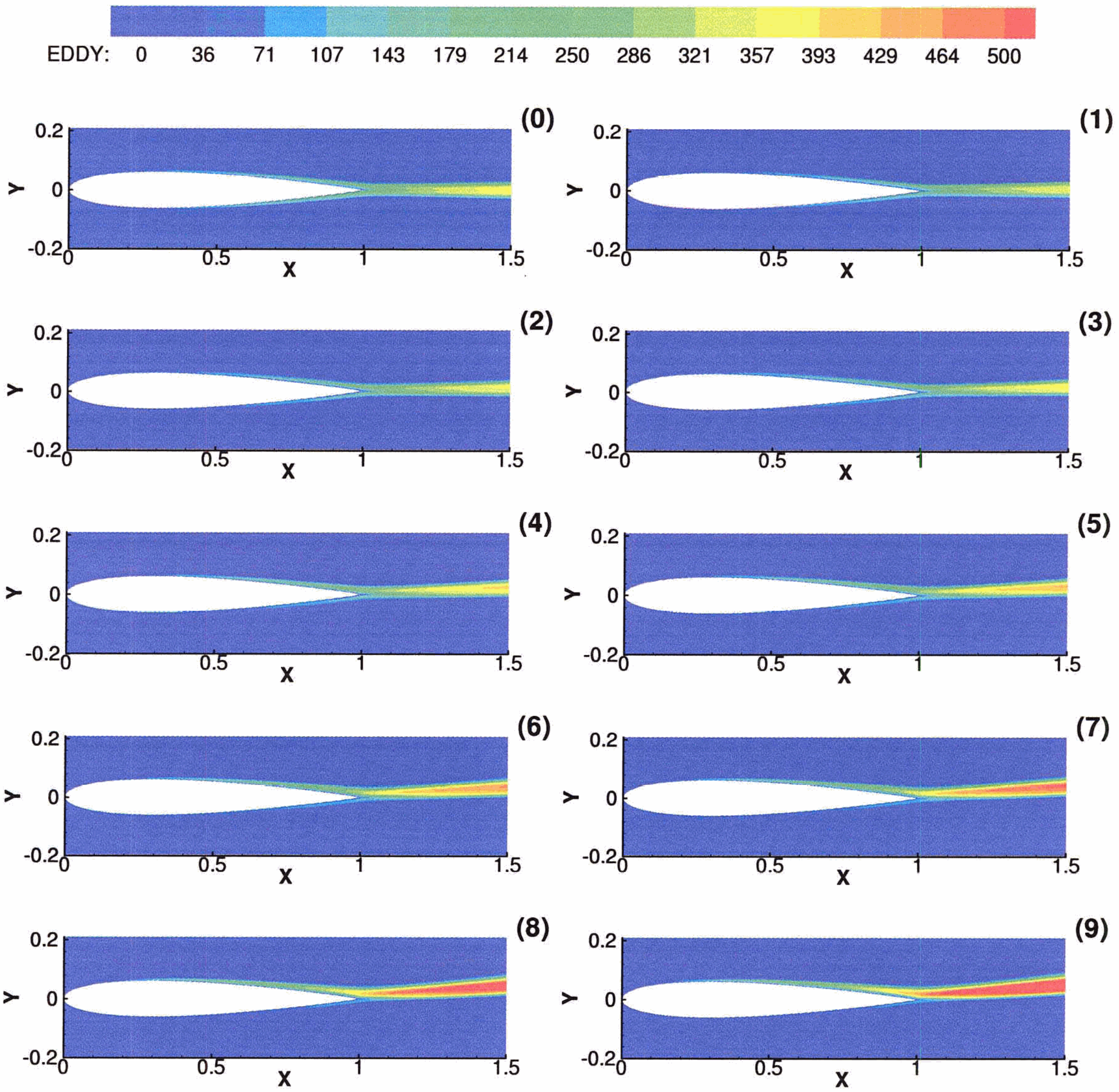

Figure 3.14: NACA 0012 Spalart Allmaras model eddy viscosity contours ($\frac{\mu_t}{\mu}$) at $Re_c = 3 \times 10^6$ for $\alpha = 0°$ to $\alpha = 9°$

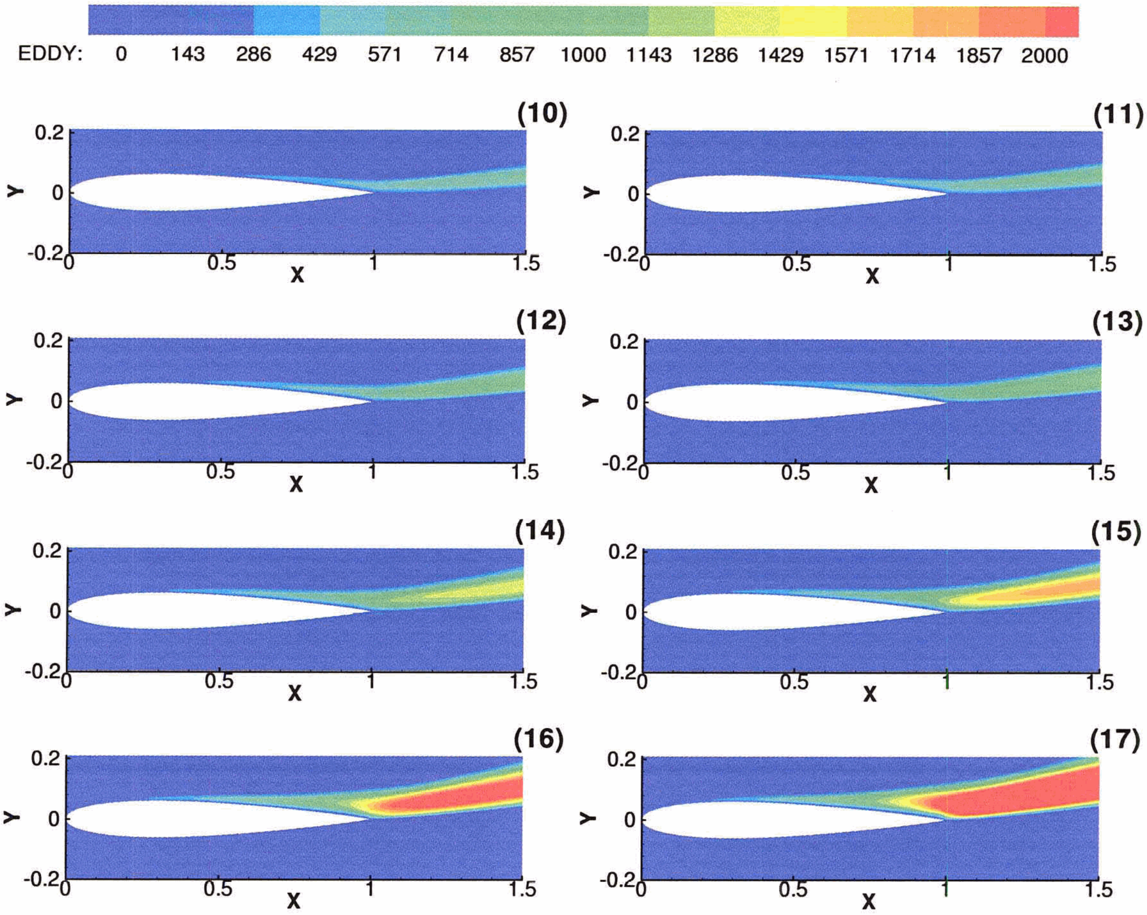

Figure 3.15: NACA 0012 Spalart Allmaras model eddy viscosity contours ($\frac{\mu_t}{\mu}$) at $Re_c = 3 \times 10^6$ for $\alpha = 10°$ to $\alpha = 17°$

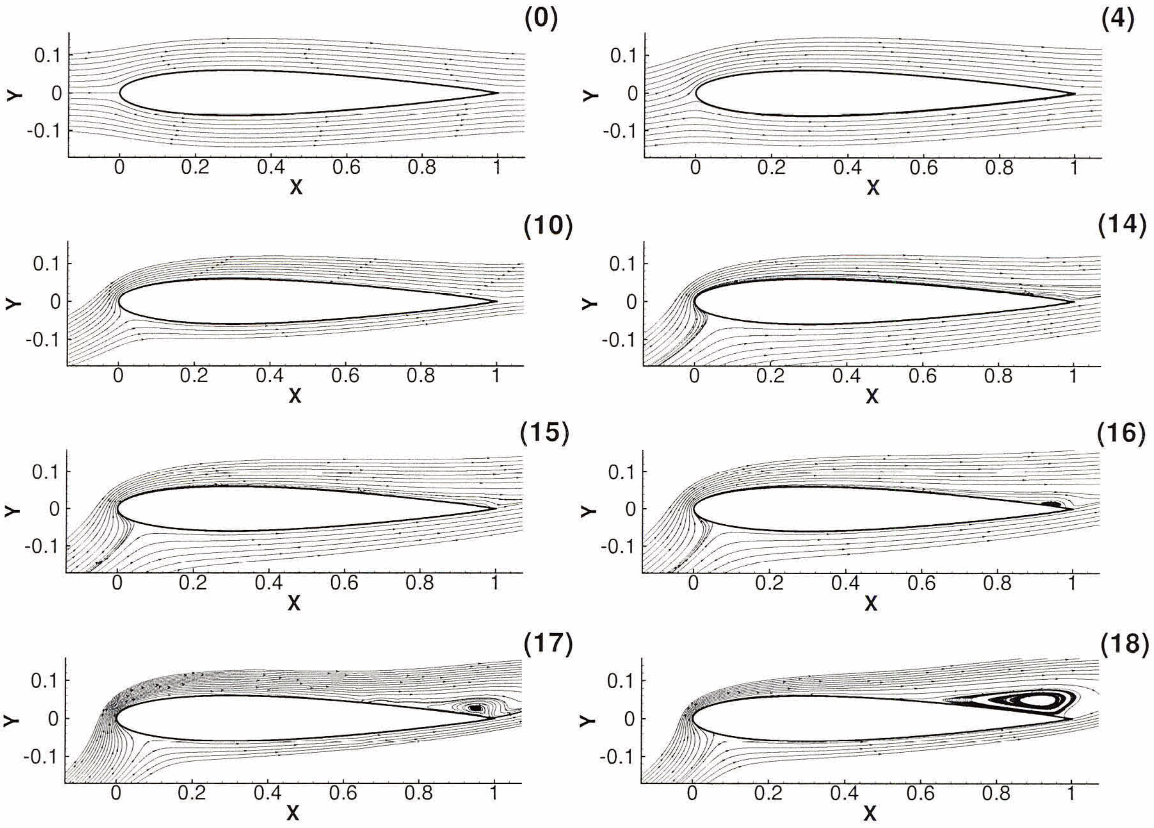

Figure 3.16: NACA 0012 Spalart Allmaras model stream lines at $Re_c = 3 \times 10^6$ for selected angles of attack from $\alpha = 0°$ to $\alpha = 18°$

3.4 Speziale $k - \tau$

Results for the two equation $k - \tau$ model (KTS) of Speziale/Abid/Anderson [22] are presented. The final grid from the Spalart Allmaras steady state simulations is used. The grid study for the SA model should be adequate since both SA and KTS models account for low Reynolds number turbulence near solid walls and do not use wall functions. Using the same grid for each model makes comparison of the results and assessment of the models more straightforward. Eddy viscosity is the only free stream turbulence parameter that must be set for the SA model. The KTS model has two transport equations, one for the turbulent time scale τ and the other for the turbulent kinetic energy k. Two free stream parameters must therefore be set; these are the turbulent intensity and the eddy viscosity. The turbulent intensity is the square root of the ratio of the turbulent kinetic energy (the energy of turbulent velocity fluctuations) divided by the free stream kinetic energy:

$$\text{turbulent intensity} = \frac{\sqrt{\frac{1}{3}\left(\overline{u'^2} + \overline{v'^2} + \overline{w'^2}\right)}}{U_\infty} \tag{3.6}$$

Wind tunnel values of turbulent intensity are influenced by the size and configuration of the meshes and honeycombs used to straighten the flow; values as low as 0.1% are possible although a value of 0.3% is more typical [33]. For the KTS simualtions, the turbulent intensity is set to a free stream value of 0.3% in order to match typical experimental data.

Initial runs at the very low eddy viscosity used for the SA model ($\frac{\mu_t}{\mu} = 10^{-7}$) did not result in a converged solution. This is probably due to the inherent instability of the model when used in conjunction with non-dissipative numerical schemes. A parametric study of eddy viscosity was therefore carried out for the KTS model to determine appropriate initialization and far field values. $\frac{\mu_t}{\mu} = 1$ is the lowest value of eddy viscosity ratio for which convergence is obtained; simulations are therefore carried out at this eddy viscosity.

Figure 3.17 shows the pressure distribution along both surfaces of the airfoil for various angles of attack. The magnitude of the C_p curve peaks is approximately 10% lower than the Spalart Allamaras model and is a very close match to the experimental work of Gregory [30] for $\alpha \leq 12°$. The pressure peaks at the leading edge are slightly under predicted (10%) above $\alpha = 14°$.

Figure 3.18 shows velocity streamlines from the KTS model at various angles of attack from $\alpha = 0°$ to $\alpha = 17°$. A trailing edge separation bubble first appears at $\alpha = 16°$ as it did with the SA model but is considerably larger here. The bubble diameter d for the SA model is approximately $d/c = 0.02$ where here it is $d/c = 0.06$ for $\alpha = 16°$. Again, at $\alpha = 17°$, the separation bubble is larger than the SA model and there is an additional recirculation bubble right at the trailing edge. Convergence was not possible in steady state beyond $\alpha = 17°$ and unsteady effects (periodic oscillation) occurred at $\alpha \geq 16°$.

Eddy viscosity contour plots for the KTS model are shown in figure 3.19. Results are similar to those of the SA model except in the separated region at higher angles of attack ($\alpha \geq 12°$) where the eddy viscosity has a higher magnitude over a wider area. This can be seen by comparing the eddy viscosity ratio plots at $\alpha = 17°$ for the SA and KTS models.

The turbulent time scale τ is presented in figure 3.20. The smallest time scales (small scales of turbulence) occur in the boundary layer near the airfoil surface. The largest scales are found in the wake and in separated regions at high angles of attack.

The turbulent kinetic energy ratio contours in figure 3.21 closely follow the eddy viscosity contours of figure 3.19. The turbulent kinetic energy is approximately 30

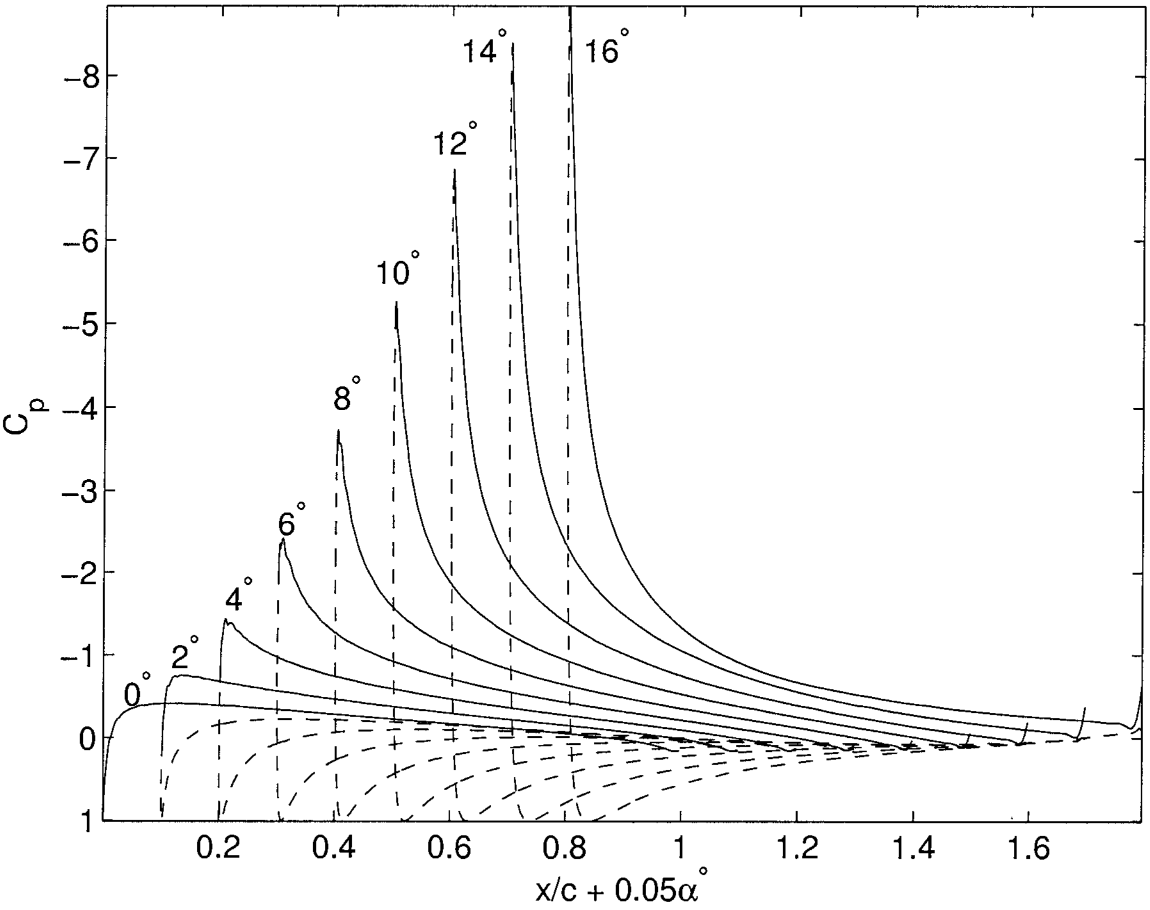

Figure 3.17: NACA 0012 Speziale $k-\tau$ model airfoil surface pressure distribution, $Re_c = 3 \times 10^6$ for selected angles of attack from $\alpha = 0°$ to $\alpha = 16°$; the lower surface in dashed lines, the upper surface is in solid lines

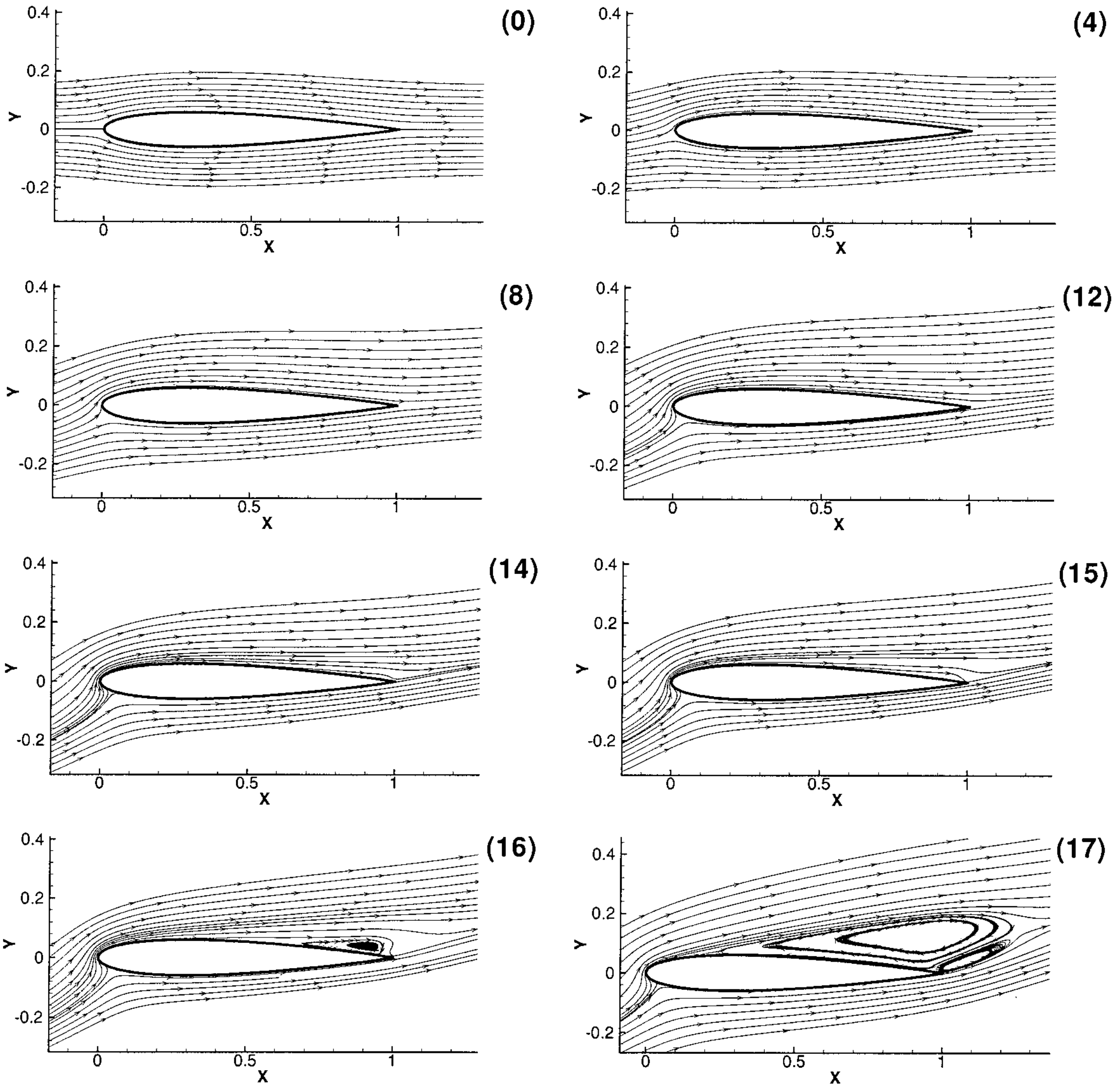

Figure 3.18: NACA 0012 Speziale $k-\tau$ streamlines, $Re_c = 3 \times 10^6$ for selected angles of attack from $\alpha = 0°$ to $\alpha = 17°$

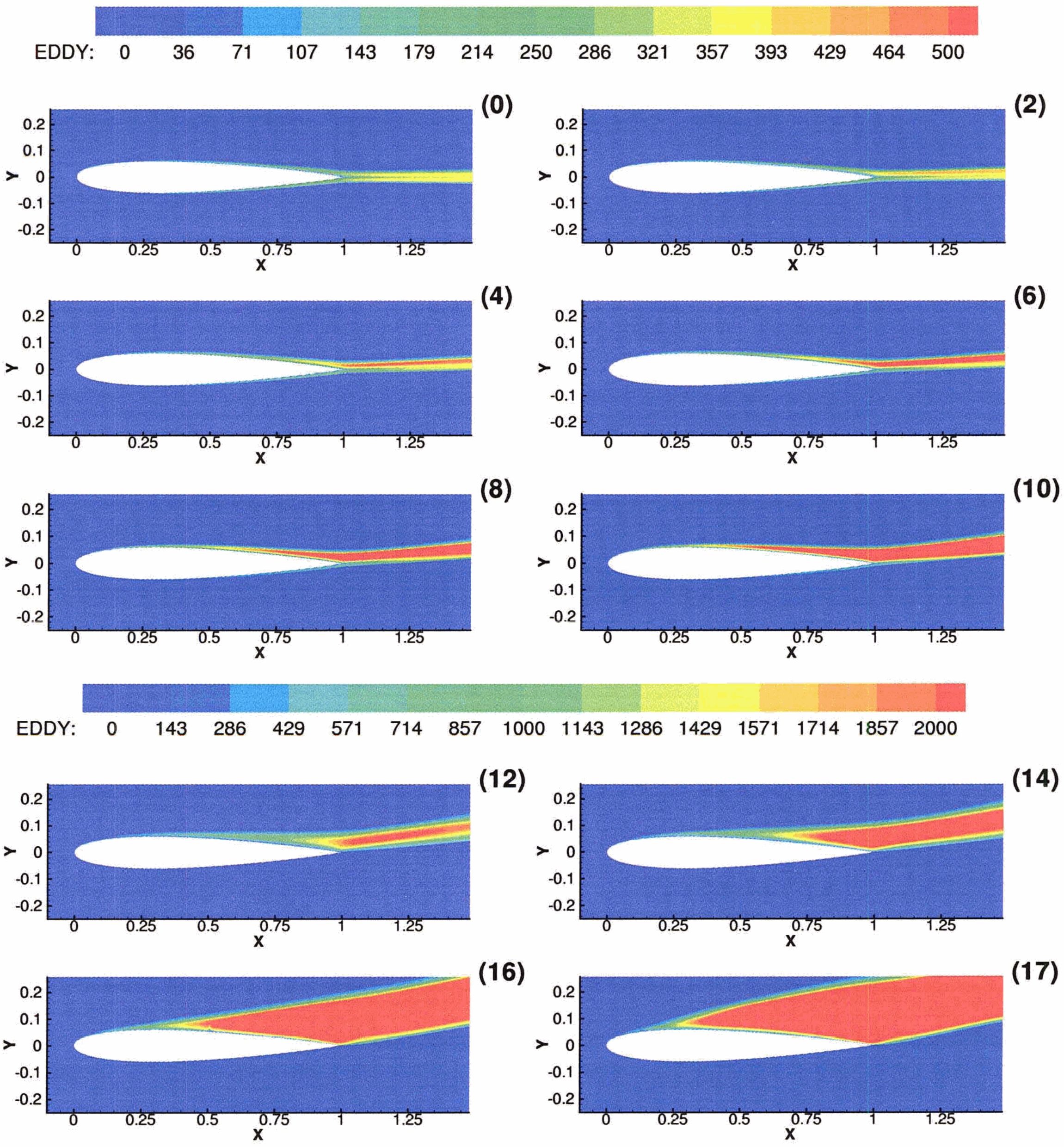

Figure 3.19: NACA 0012 Speziale $k-\tau$ eddy viscosity $\frac{\mu_t}{\mu}$, $Re_c = 3 \times 10^6$ for selected angles of attack from $\alpha = 0°$ to $\alpha = 17°$

times larger than the free stream mean kinetic energy in the separated regions for $\alpha \geq 16°$ and in the wake for $\alpha = 12°$ and $\alpha = 14°$. (Note that the turbulent kinetic energy ratio is the ratio of the local turbulent kinetic energy to the free stream turbulent kinetic energy. The free stream turbulent kinetic energy is set at 0.3% of the kinetic energy of the mean flow.)

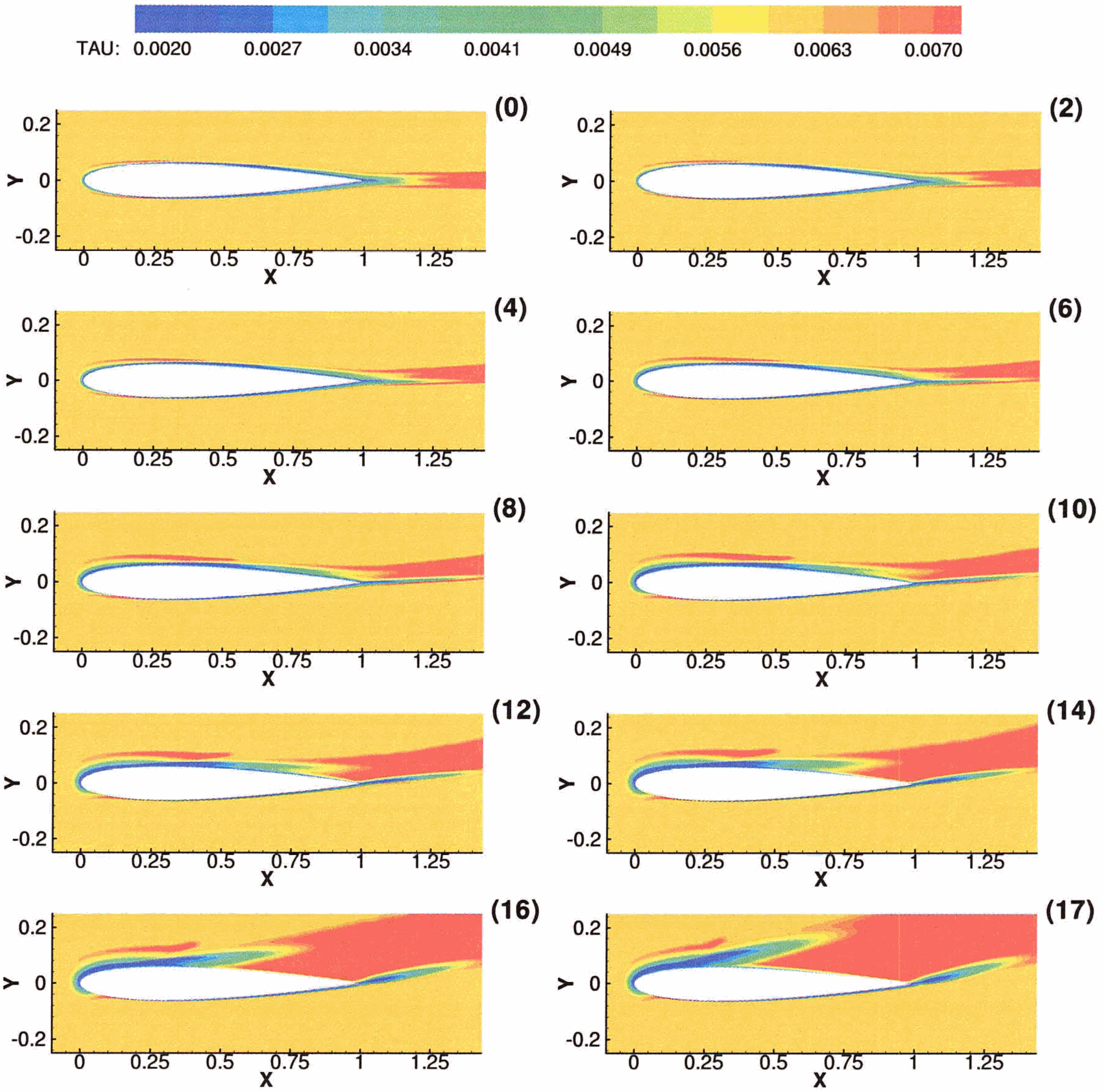

Figure 3.20: NACA 0012 Speziale $k-\tau$ turbulent time scale τ in seconds, $Re_c = 3\times10^6$ for selected angles of attack from $\alpha = 0°$ to $\alpha = 17°$

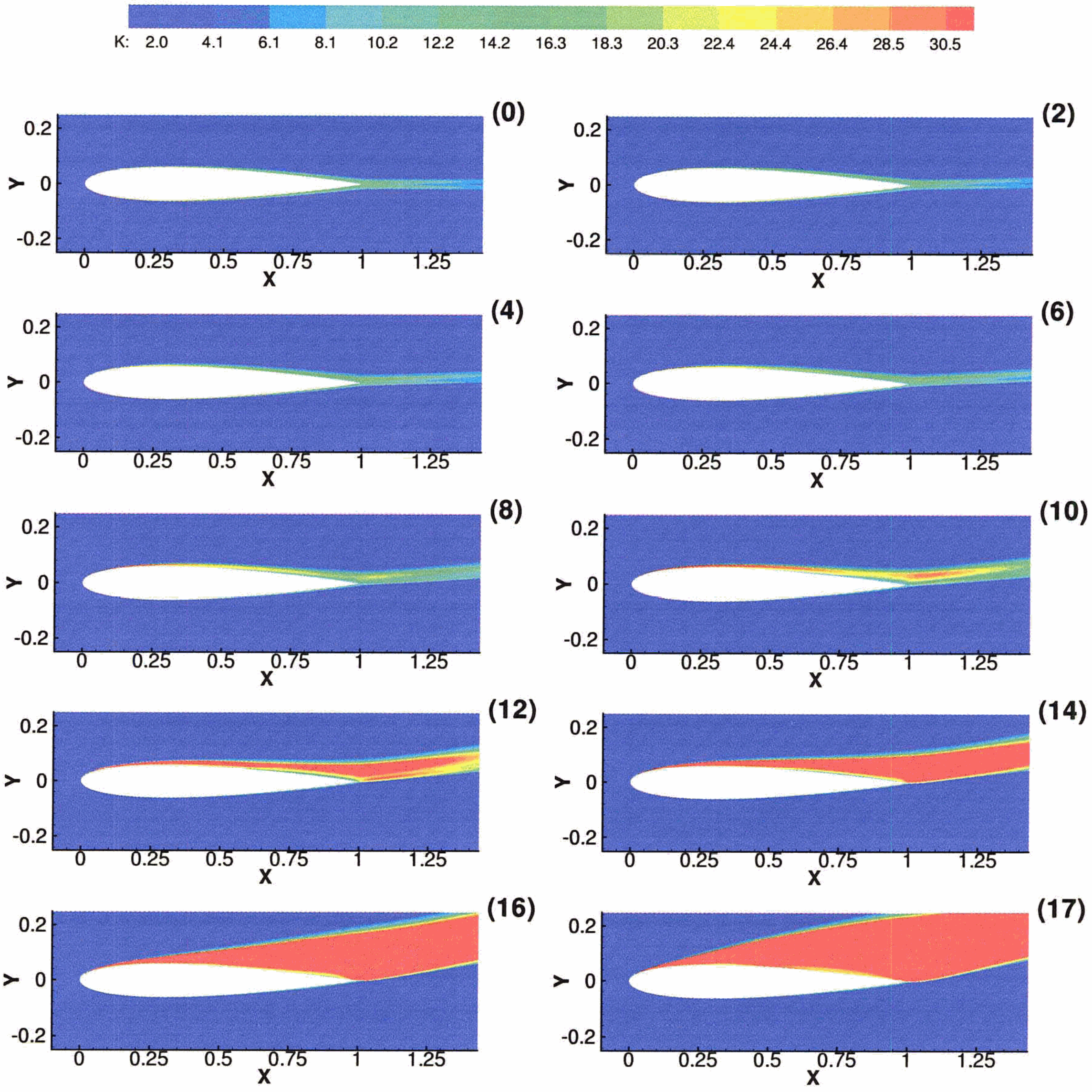

Figure 3.21: NACA 0012 Speziale $k-\tau$ turbulent kinetic energy ratio, $Re_c = 3 \times 10^6$ for selected angles of attack from $\alpha = 0°$ to $\alpha = 17°$

3.5 Comparison of Steady State Results

Lift, drag and shear stress predictions are compared between turbulence models and experimental data in this section. Numerical results have not been obtained above the stall angle of attack ($\alpha \approx 17°$) since the post stall regime is unsteady.

Figure 3.22 compares the lift curves of the SA and KTS models with the experimental data of Abbott [38]. The SA model follows the experimental curve very closely up to $\alpha = 16°$. The KTS model is in good agreement with the experimental data up to approximately $\alpha = 8°$ after which it under predicts C_l.

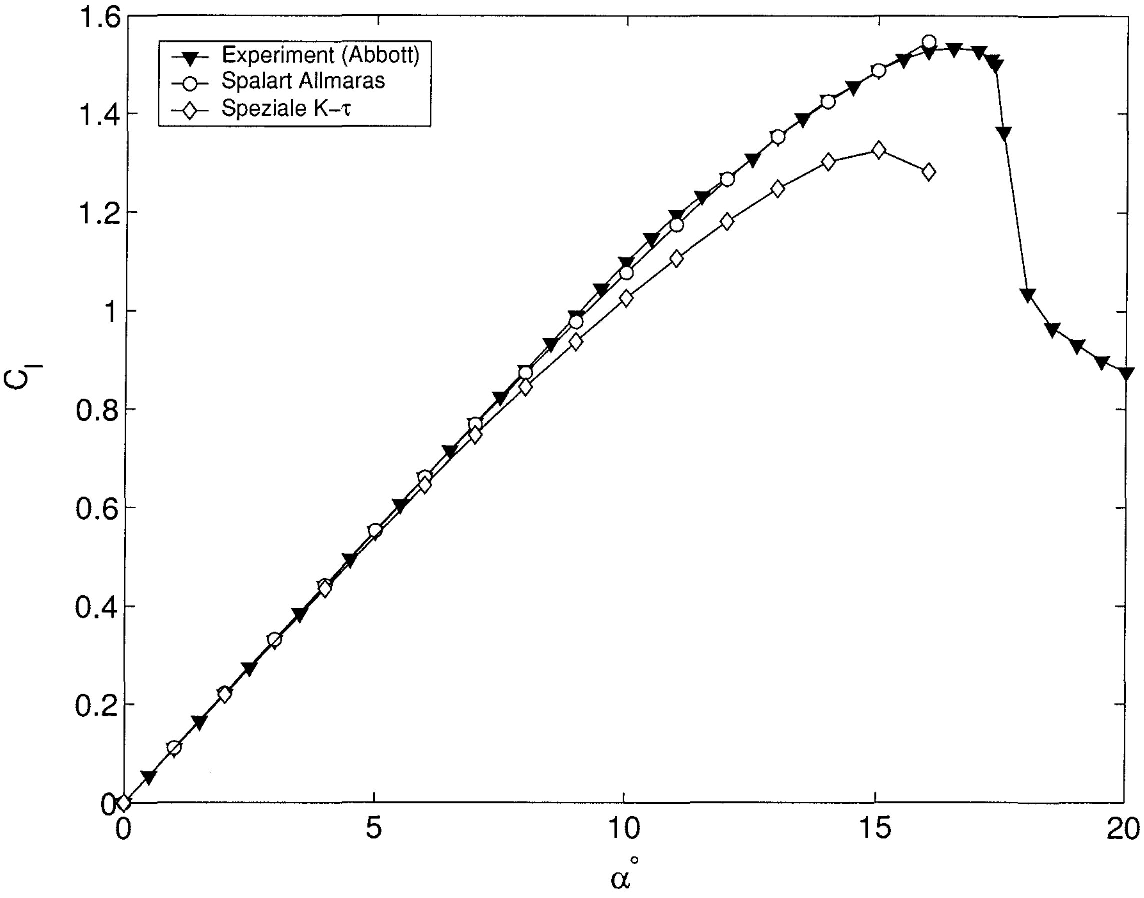

Figure 3.22: Comparison of Experimental and Numerical Lift Curves for NACA 0012

The drag (C_d) curves are plotted in figure 3.23. Again, below $\alpha = 8^\circ$, both the SA and KTS models predict the drag quite well. However, at angles of attack approaching stall, both models stray from the experimental results. Abbott [38] only presents drag measurements up to $\alpha = 12^\circ$. Critzos [41] measured the lift and drag for the NACA 0012 airfoil through all angles of attack (0° to 180°) encountered by helicopter rotors (the NACA 0012 section is common in these applications [42]). The KTS model over predicts the drag before $\alpha = 14^\circ$ and under predicts the drag after $\alpha = 14^\circ$. The SA model under predicts drag for $\alpha \geq 12^\circ$. Neither model appears to properly predict the large increase in drag which occurs between $\alpha = 14^\circ$ and $\alpha = 16^\circ$.

Experimental results for the shear stress distribution along the airfoil surface were not found since measurement of friction drag is very difficult. Friction drag results for the SA and KTS models are shown in figure 3.24. Note that drag is always measured in a direction parallel to the free stream flow. As α increases, a component of the shear stress along the airfoil surface begins to act in a direction perpendicular to the free stream flow. The friction drag acting in the direction parallel to the free stream (C_{df}) is related to the friction drag parallel to the airfoil chord (C_{dfc}) by:

$$C_{df} = C_{dfc} \cos \alpha \tag{3.7}$$

Equation (3.7) should be considered when looking at figure 3.24. The friction drag decreases with increasing α. Some of this decrease can be attributed to the cosine of α, but consider that $\cos 16^\circ = 0.96$. If the chord parallel friction drag C_{dfc} were to remain constant from $\alpha = 0^\circ$ to $\alpha = 16^\circ$, a reduction of only 4% in C_{df} would occur. Looking at the friction drag curve for the KTS model, a reduction of 45% is seen. The majority of the reduction in friction drag with increasing α can be attributed to flow physics rather than $\cos \alpha$. The thickness of the boundary layer on the upper side of the airfoil increases with increasing α; the shear stress at the wall is reduced

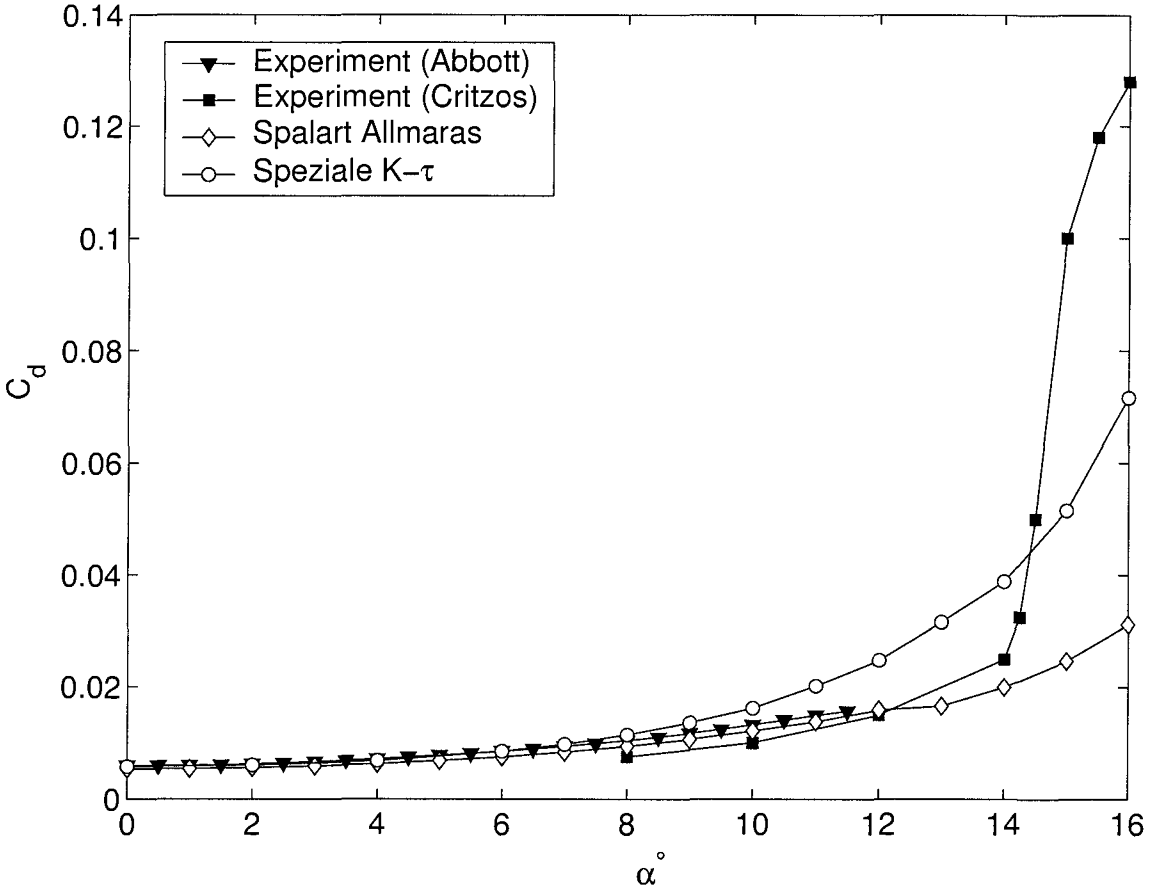

Figure 3.23: Comparison of Experimental and Numerical Drag Curves for NACA 0012

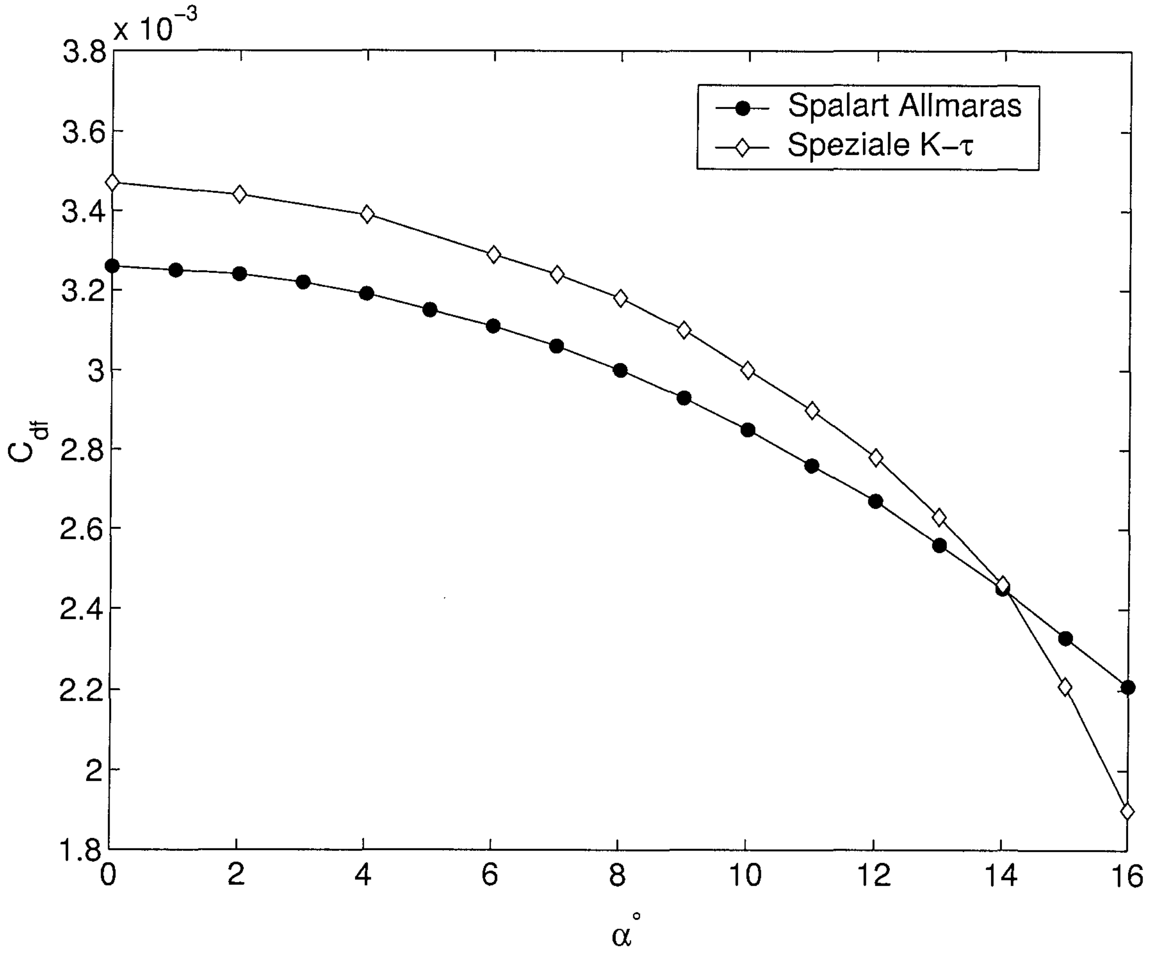

Figure 3.24: Comparison of Friction Drag Curves for NACA 0012

since the velocity gradient is smaller. Where separation bubbles appear, there is zero velocity at the separation point and reversed velocity in the separation region along the wall. These effects further reduce the friction drag.

Lombardi et al [1] calculated the shear stress along the NACA 0012 surface at $\alpha = 0°$ using FLUENT. Their results are compared to the results of the SA and KTS models in figure 3.25. Lombardi shows a higher friction drag peak ($C_{df} = 0.009$) at the leading edge ($x/c = 0.02$) and lower drag in the region $x/c \geq 0.3$. The SA and KTS friction drag curves are similar, the KTS curve being slightly higher.

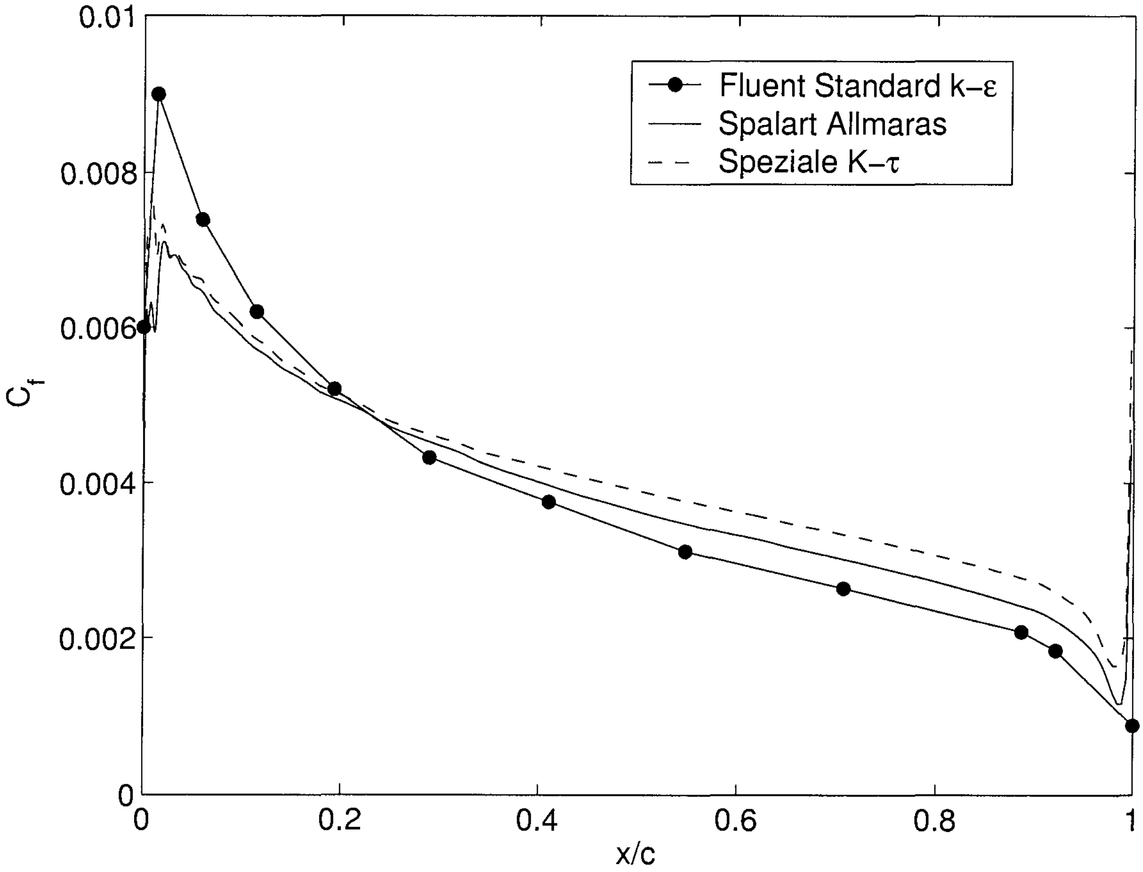

Figure 3.25: Comparison of Friction Drag Curves for NACA 0012 at $\alpha = 0°$ and $Re_c = 3 \times 10^6$ for Spalart Allmaras and Speziale $k - \tau$ Turbulence Models with the FLUENT results of Lombardi [1]

3.6 Summary

In this chapter, grid resolution and the eddy viscosity boundary condition are tested parametrically. An appropriate eddy viscosity is determined by examining its effect on the turbulent transition point and the airfoil surface shear stress. It is found that the surface shear stress profile does not change for the Spalart Allmaras model when the eddy viscosity ratio $\frac{\mu_t}{\mu}$ is less than 10^{-6}. A grid study is carried out for the Spalart Allmaras model by doubling the grid resolution globally and in the wall blocks. The effect on the lift, friction drag and pressure drag coefficients is checked. The final grid has a doubled wall block resolution and a total of 130,368 grid points.

Steady state simulations for angles of attack from $\alpha = 0°$ to $\alpha = 17°$ are presented for the Spalart Allmaras and Speziale $k-\tau$ models. Contour plots of pressure, velocity and eddy viscosity are presented for both models. Plots of turbulent kinetic energy ratio and turbulent time scale are given for the Speziale $k-\tau$ model. Both models give good results until stall is approached. Unsteady effects cause the simulations to diverge in the post stall regime for $\alpha > 16°$ where the drag tends to be under predicted.

Chapter 4

Unsteady Simulations

Reynolds Averaged Navier Stokes (RANS) simulations are only able to predict steady state flow fields; the turbulence models represent the time averaged effect of the turbulence [7]. For the NACA 0012 airfoil at low angles of attack ($\alpha < 10°$) there is no separation of the mean flow and the time averaged shear stress at every point on the airfoil surface is positive. There are of course small scale velocity fluctuations in the turbulent boundary layer and some negative instantaneous velocities, but their time average remains positive.

As the angle of attack increases above 13°, the adverse pressure gradient on the upper side of the airfoil leads to flow separation. The mean velocity close to the wall becomes negative in certain locations. Large vortices whose diameters are similar in scale to the chord length are shed; there is significant variation in the coefficients of lift (C_l) and drag (C_d) with time. The physics of such separated flows become much more complex and are therefore much more challenging for the turbulence models [17],[43].

To carry out unsteady (URANS) calculations using RANS techniques, some of the fluctuations, such as large scale vortex shedding, must be resolved numerically rather than being accounted for in a model.

A grid similar to that used for the steady state simulations is used here. Since the Reynolds number is much lower ($Re_c = 10^5$ rather than $Re_c = 3 \times 10^6$), the mesh resolution required normal to the wall is less demanding. The first grid point from the wall is again located at $y^+ \approx 1$. The grid is refined in the x direction along the upper surface of the airfoil, and at the leading and trailing edges. The domain size remains the same, with far field boundaries applied everywhere except at the airfoil wall (solid boundary). Rather than apply an angle of attack by changing the flow direction of the free stream, the airfoil grid is tilted; this ensures sufficient downstream length before the outlet. Convergence problems were encountered for the case $\alpha = 20°$ using free stream tilting rather than tilting the grid; the wake reached the far field boundaries too quickly.

The grid has 329 grid point along the airfoil surface in the x direction, 209 of which are on the upper surface. There are 121 points in the cross stream (y) direction and 225 points in the downstream (x) direction. The outlet flares in the cross stream direction to reduce cell aspect ratios at $x = 0$, $y > 15$. Convergence difficulties were encountered for aspect ratios greater than 400.

A major grid study is not undertaken for the unsteady simulations. It would be difficult to achieve due to the computation time required and the unsteady nature of the results. By using a grid similar to that used in the steady state simulations, with wall resolution at $y^+ \approx 1$ and more points along the upper airfoil surface, reasonable unsteady results are expected. The interest for the unsteady simulations is focused on a qualitative view of the vortex shedding phenomena and the impact of the turbulence model rather than an exact prediction of the lift and drag.

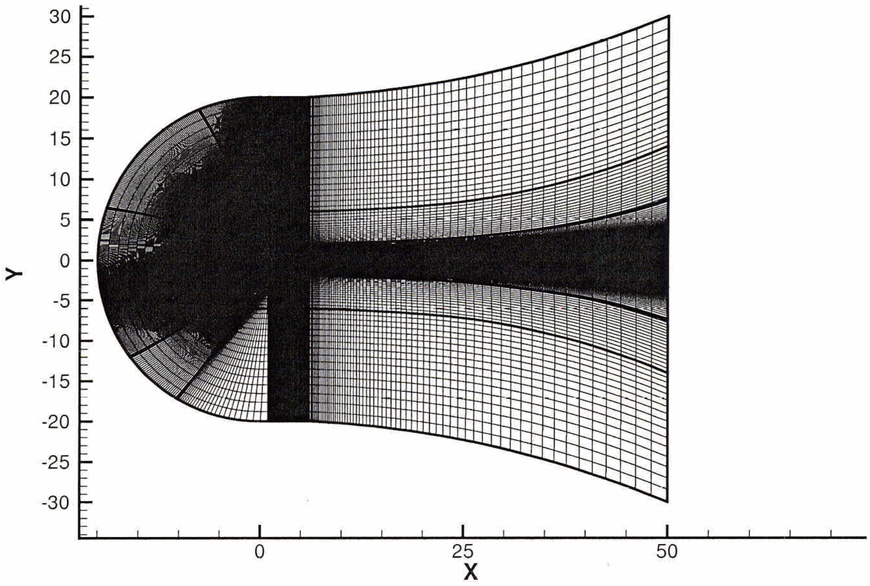

Figure 4.1: Grid Domain for Unsteady Simulations; $\alpha = 20°$

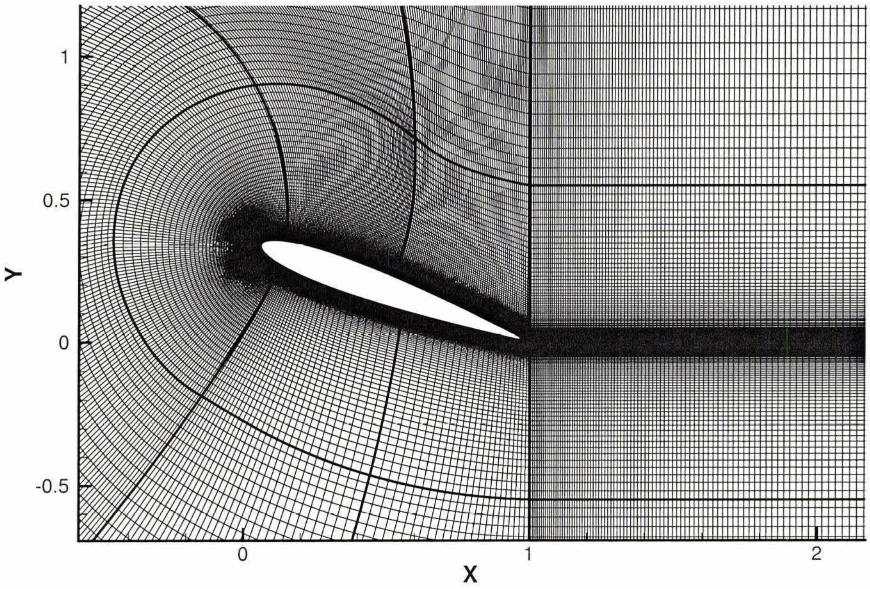

Figure 4.2: Tilted Grid Around Airfoil for Unsteady Simulations; $\alpha = 20°$

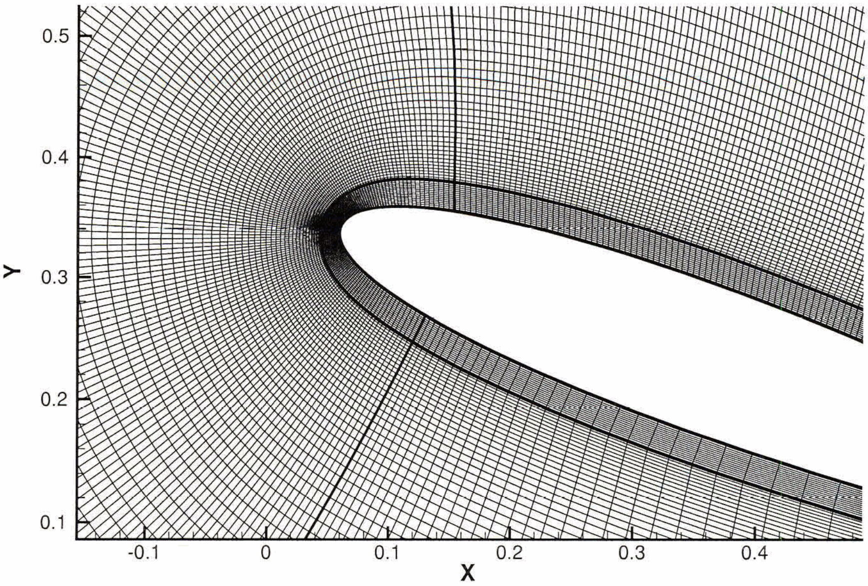

Figure 4.3: Grid Detail Near Leading Edge for Unsteady Simulations; $\alpha = 20°$

4.1 Spalart Allmaras

The Spalart Allmaras model did not produce an unsteady flow pattern at $\alpha = 0°$ and $Re_c = 10^5$ with the free stream eddy viscosity set to 1. At a low free stream eddy viscosity of 10^{-6}, oscillations were present in the lift and drag signals but there were large eddy viscosity gradients near the domain boundaries. It was not possible to converge the solution at each time step. To overcome the problems at the boundaries and to stabilize the solution, the eddy viscosity was set to 1. For the sake of consistency, this matches the boundary conditions applied to the adaptive $k-\tau$ and Speziale $k-\tau$ models. It should also be noted that the Spalart Allmaras model implemented in SPARC has been tuned for steady state solutions; applying it to an unsteady problem may not be feasible. Only steady state results were therefore obtained.

Contour plots of the Spalart Allmaras results at $\alpha = 20°$ and $Re_c = 10^5$ are presented with time averaged results for the Speziale $k-\tau$ and adaptive $k-\tau$ models.

4.2 Speziale $k - \tau$

Figure 4.4 shows the lift and drag signals for the KTS model at $Re_c = 10^5$ and $\alpha = 20°$. The frequency and phase of the lift and drag are identical; the signal is periodic. The period is approximately 0.1 seconds which corresponds to a Strouhal number of $St = 0.55$ based on the chord length c, the free stream velocity $U_\infty = 18.125 m/s$ and the shedding frequency. The mean values of the lift and drag coefficients are $C_l \approx 0.85$ and $C_d \approx 0.33$. The time step for these computations is 0.005 seconds; this corresponds to 20 time steps per shedding cycle.

Streamlines for the vortex shedding cycle are shown in figure 4.5 with time incre-

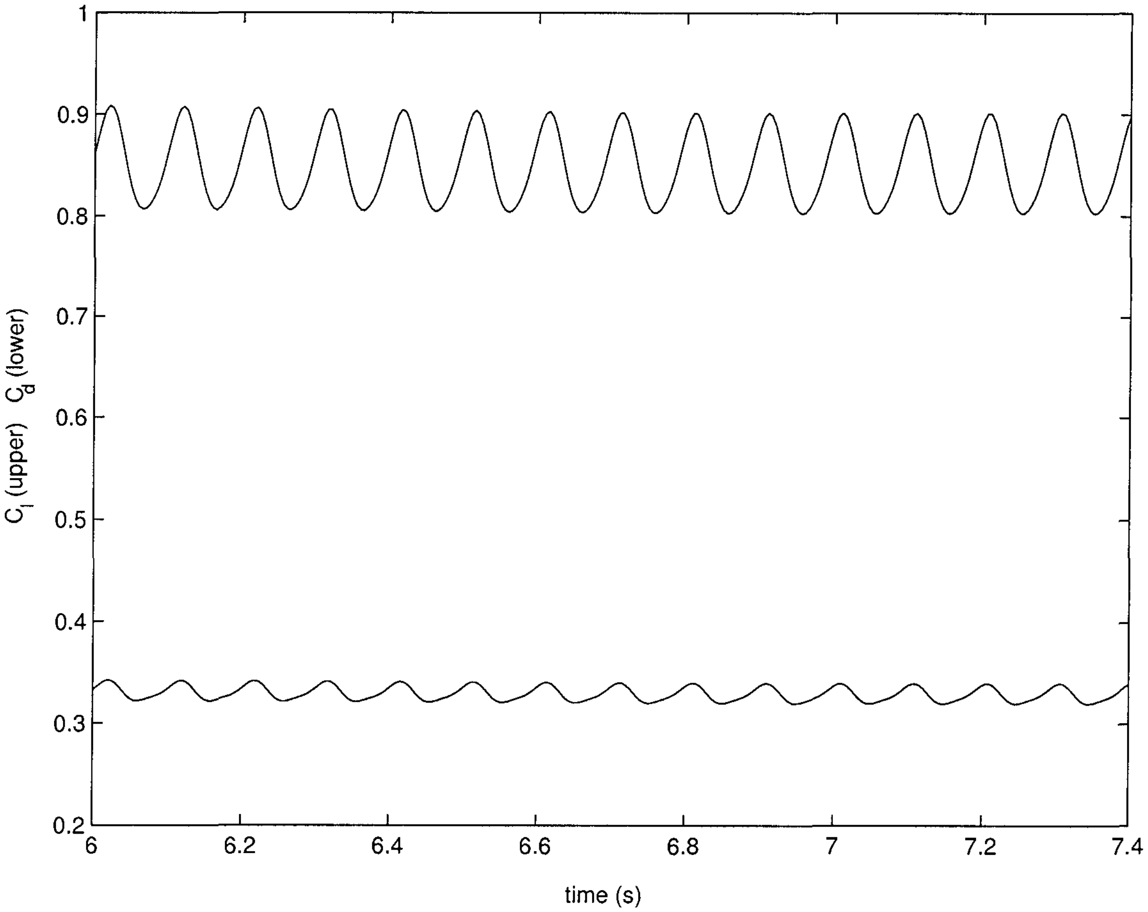

Figure 4.4: Unsteady Lift and Drag Signals for Speziale $k-\tau$ Model at $\alpha = 20°$ and $Re_c = 10^5$.

ments of $0.2T$ where T is the cycle period. The corresponding stream wise velocity contours are shown in figure 4.6. Note that the plots at $0T$ and $1.0T$ are identical; they are at the start and end of the cycle. The large separated clockwise rotating vortex in the $0T$ frame gradually moves downstream. It detaches from the airfoil at approximately $0.4T$. Note that a counterclockwise rotating vortex immediately downstream of the clockwise rotating one has already separated. At $0.6T$ a counterclockwise rotating trailing edge vortex edge appears. It is shed at $0.8T$ and a clockwise rotating vortex is re-established at the leading edge. Two vortices are shed in each cycle, one generated at the leading edge and the other at the trailing edge.

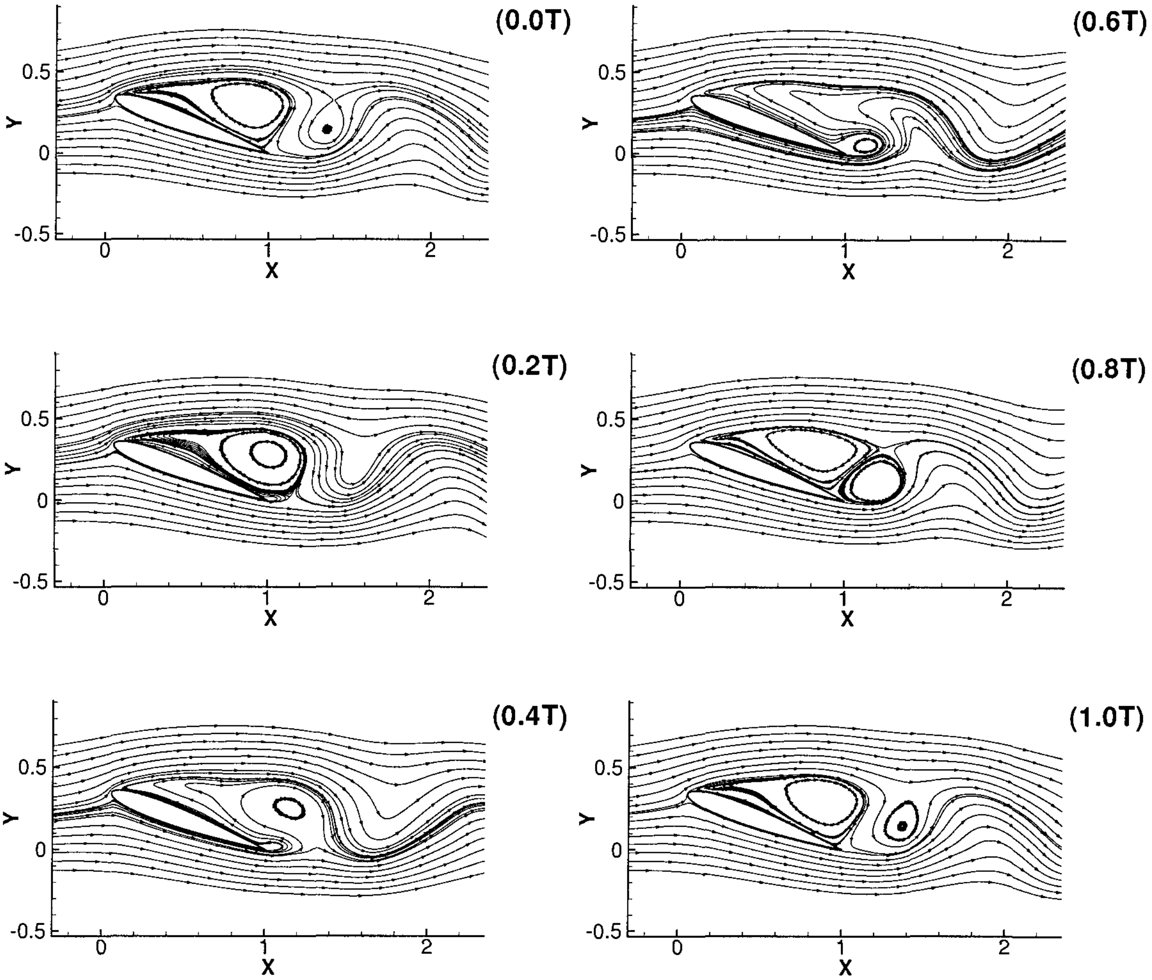

Figure 4.5: Velocity Streamlines for Speziale $k-\tau$ Model at $\alpha = 20^\circ$ and $Re_c = 10^5$; Time is given in fractions of cycle Period T

Figure 4.7 shows the pressure contours. Note that there is a low pressure region at the centre of each vortex.

Figures 4.8, 4.9 and 4.10 present the eddy viscosity ratio, turbulent time scale and turbulent kinetic energy ratio, also in increments of $0.2T$. Note that the maximum eddy viscosity occurs in the wake between $x/c = 1$ and $x/c = 2$. The smallest values ($\tau \leq 0.01$) of the turbulent time scale occur at the leading edge, in the boundary layer on the lower surface of the airfoil and in the separated shear layer at $y/c \approx 0.5$. These regions contain the smallest turbulent structures in the flow field. The separation bubble on the upper surface between $x/c = 0.1$ and $x/c = 1$ has a time scale of $\tau \approx 0.1$, as does the wake. The maximum turbulent kinetic energy occurs at the trailing edge and in the near wake at $x/c = 1$ to $x/c = 2$ which also corresponds to the area of maximum eddy viscosity. There is a turbulent kinetic energy peak in the separated shear layer at the leading edge ($x/c = 0.1$, $y/c = 0.35$).

Vorticity contours are shown in figure 4.11; a regular shedding pattern is clearly visible. Note that the contour scale is limited to values of ± 100; values as high as -9000 and $+4000$ occur in the wall boundary layer but the interest here is in the vortex shedding.

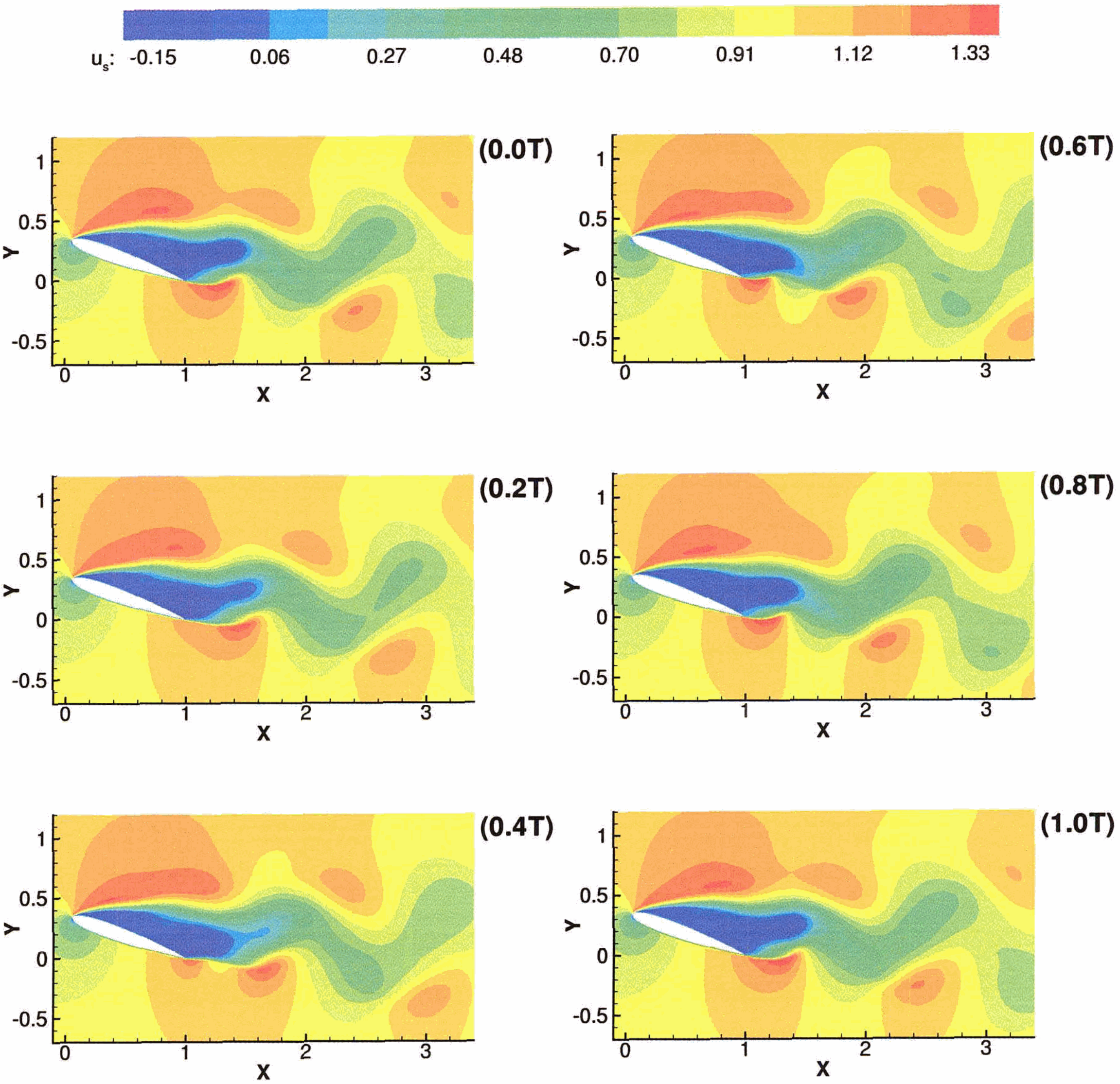

Figure 4.6: u/U_∞ Velocity Contours for Speziale $k-\tau$ Model at $\alpha = 20°$ and $Re_c = 10^5$.

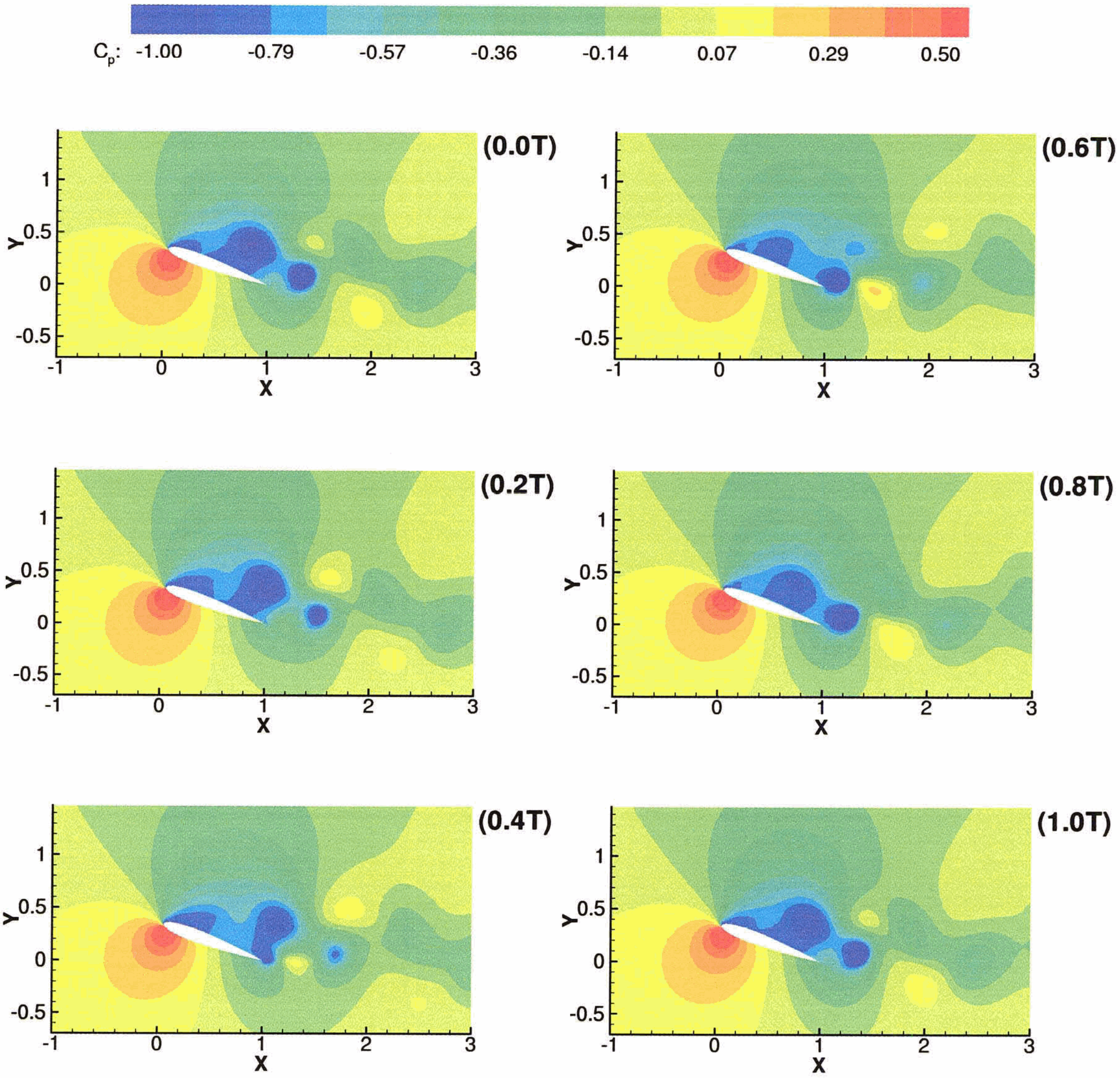

Figure 4.7: C_p Contours for Speziale $k-\tau$ Model at $\alpha = 20°$ and $Re_c = 10^5$.

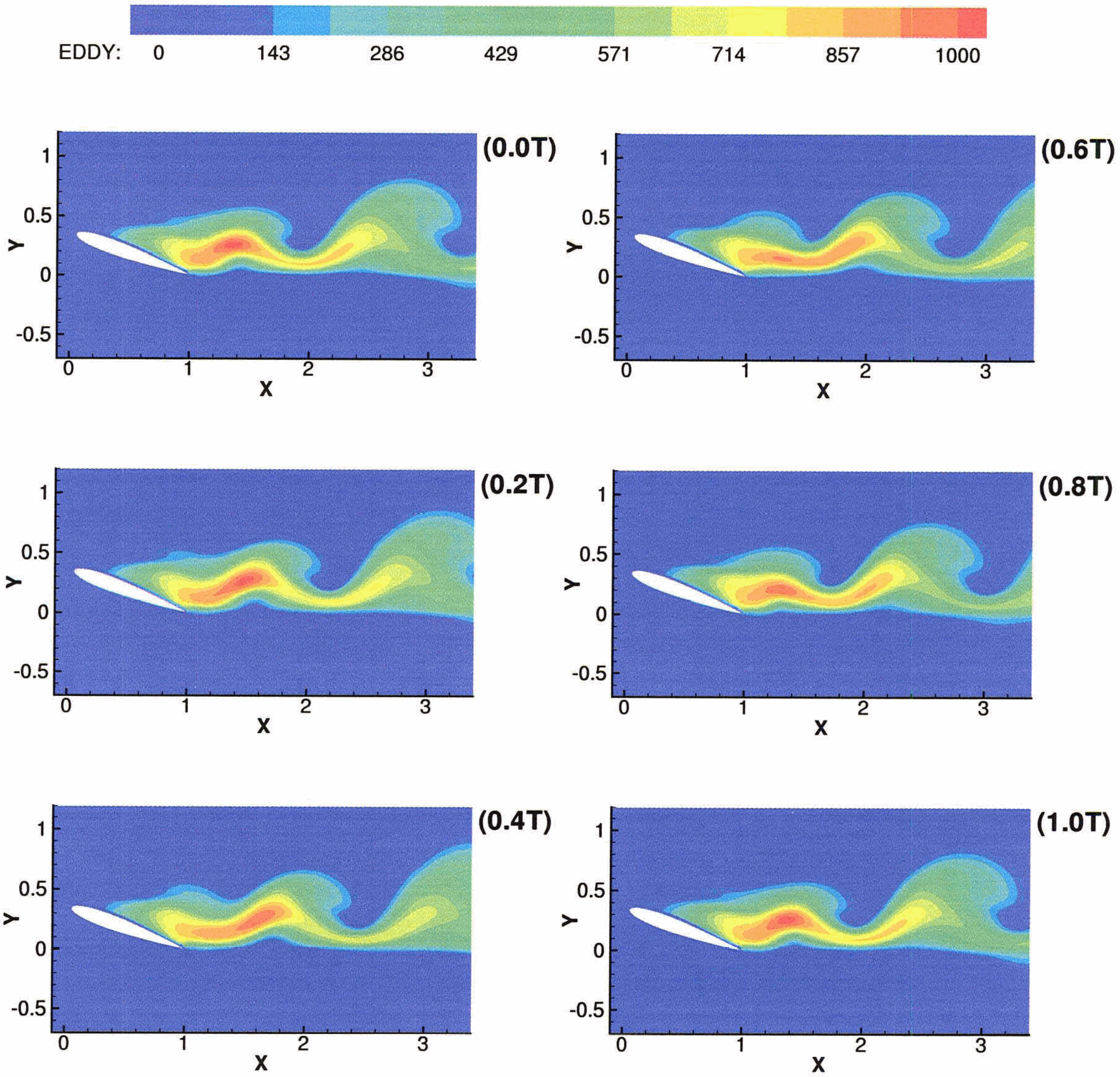

Figure 4.8: Eddy Viscosity Ratio $\frac{\mu_t}{\mu}$ Contours for Speziale $k - \tau$ Model at $\alpha = 20°$ and $Re_c = 10^5$.

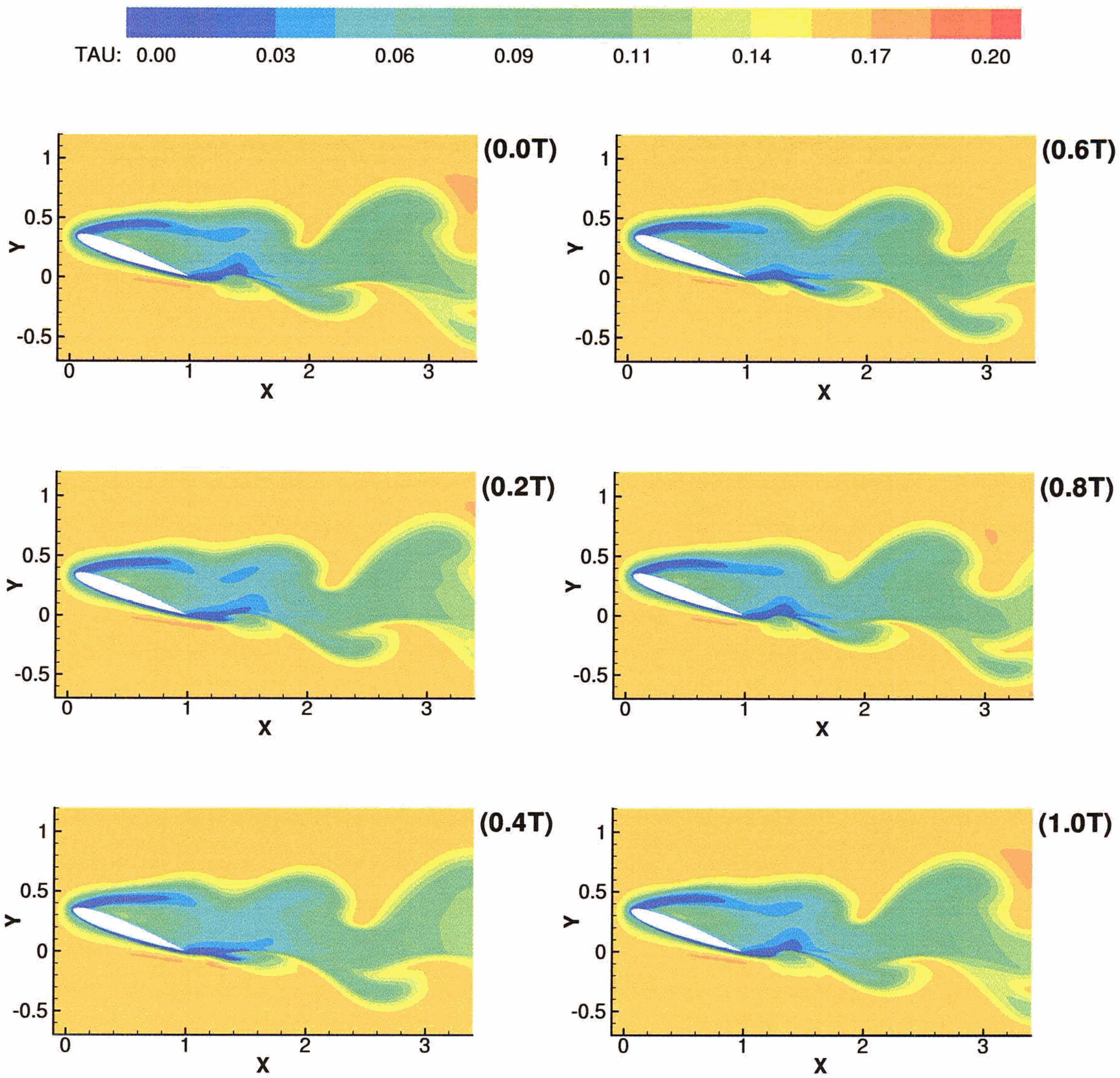

Figure 4.9: Turbulent Time Scale τ Contours in seconds for Speziale $k-\tau$ Model at $\alpha = 20°$ and $Re_c = 10^5$.

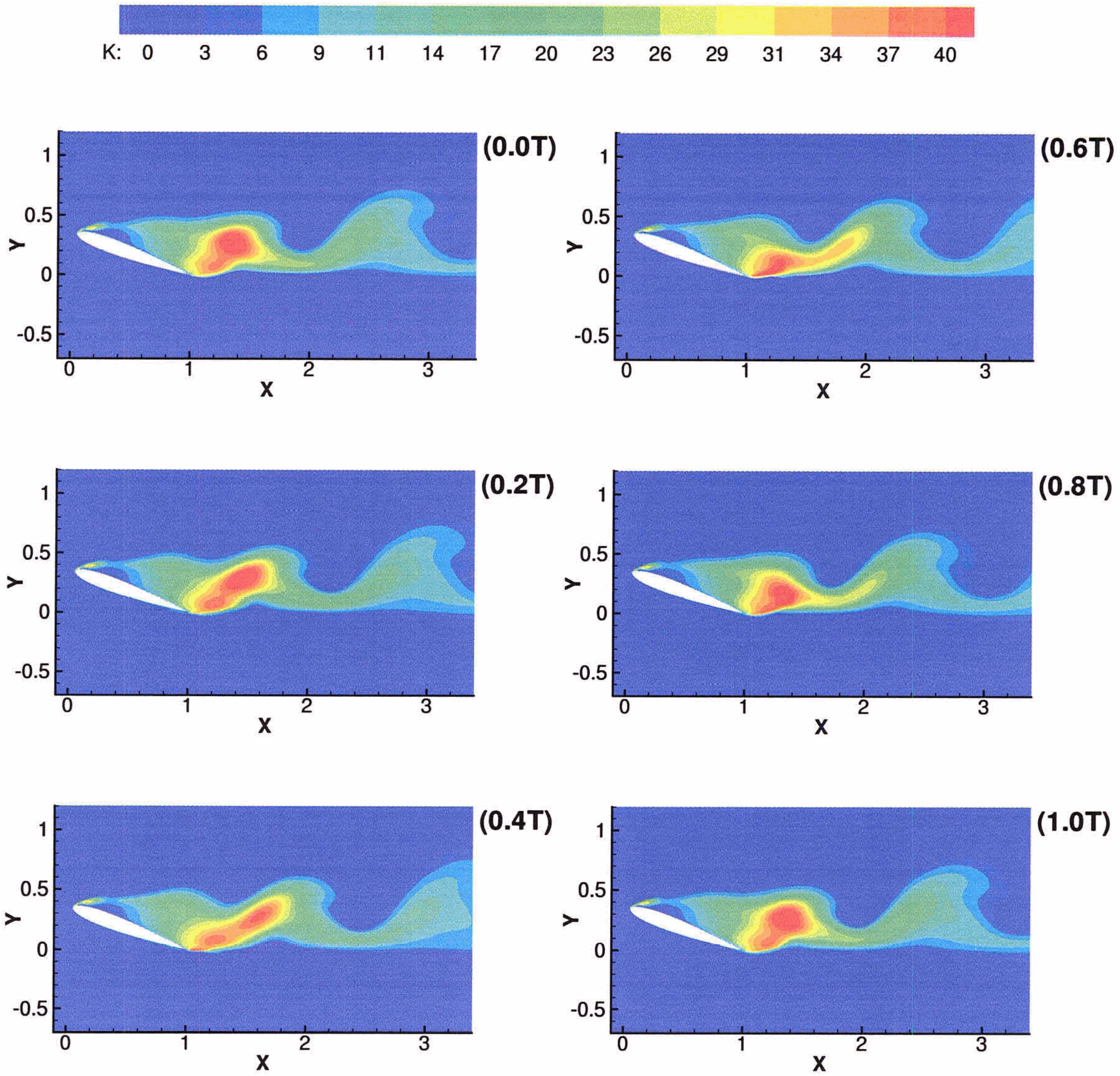

Figure 4.10: Turbulent Kinetic Energy Ratio (local to free stream) Contours for Speziale $k - \tau$ Model at $\alpha = 20°$ and $Re_c = 10^5$.

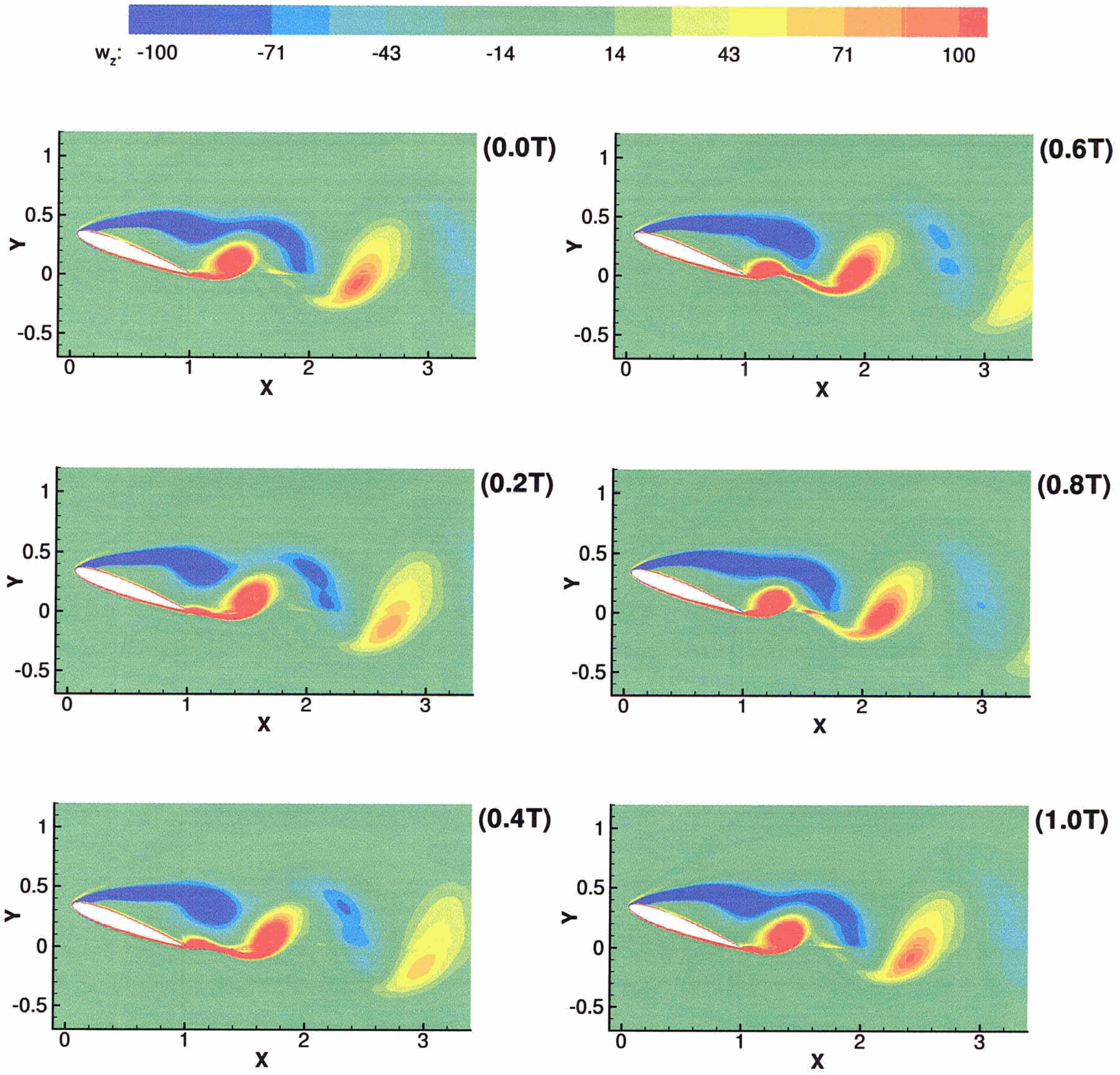

Figure 4.11: Vorticity Contours for Speziale $k-\tau$ Model at $\alpha = 20°$ and $Re_c = 10^5$.

4.3 Adaptive $k - \tau$

The unsteady results for the adaptive $k - \tau$ (AKT) model are presented here. This model yields considerably more detail than the Speziale $k - \tau$ model as can be seen in the contour plots and in the lift and drag signals of figure 4.12. The C_l and C_d signals are more stochastic and no longer perfectly periodic. The period and amplitude of vortex shedding events is similar but not identical. An approximate period for vortex shedding can be taken as $T \approx 0.1$ seconds from figure 4.12. This yields a Strouhal number of $St = 0.55$ which was also obtained from the Speziale $k - \tau$ model. The time averaged lift and drag coefficients are $C_l \approx 1.05$ and $C_d \approx 0.45$.

Velocity stream lines for the AKT model are shown in figure 4.13. The snapshot time for each plot is shown in the upper right hand corner and is listed in seconds rather than fractions of period. There is no set period since the C_l and C_d signals are not periodic. Several recirculation bubbles of various diameters are observed; see the stream line plot at $t = 0.16$ and $t = 0.28$.

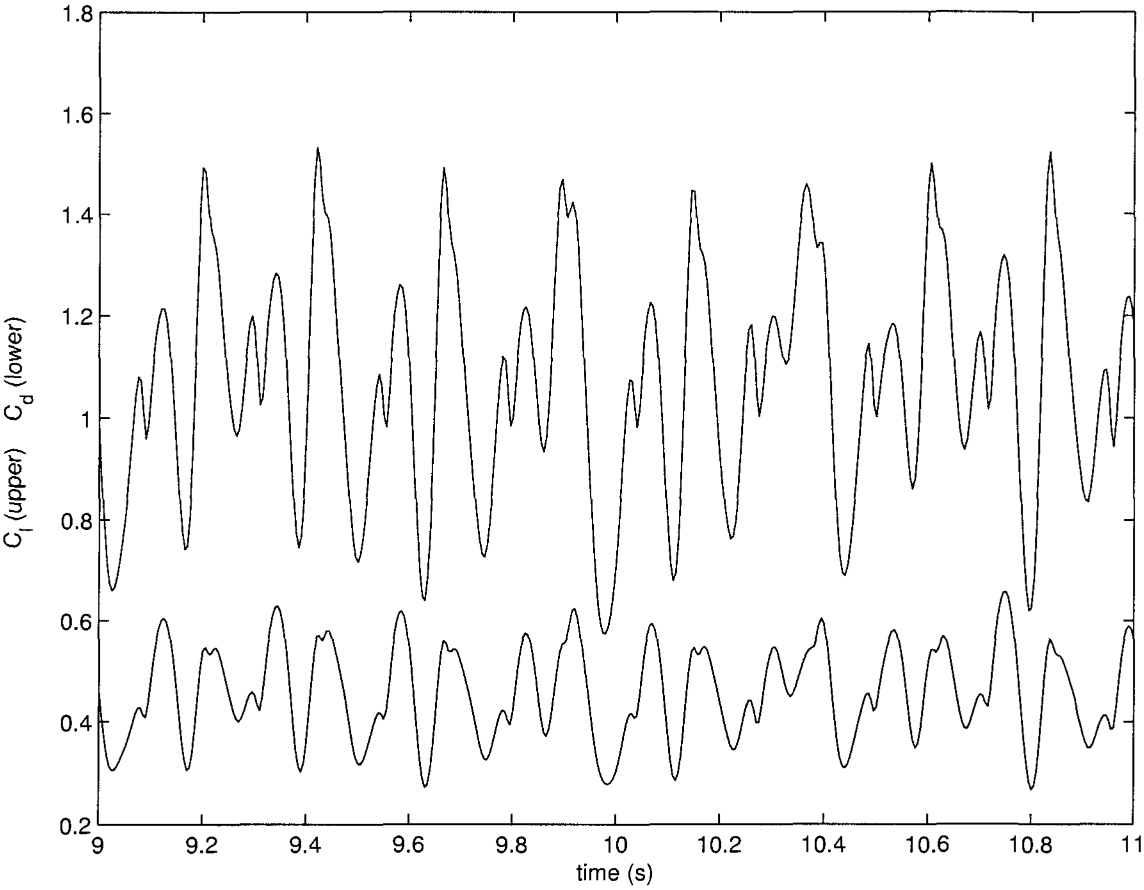

Figure 4.12: Unsteady Lift and Drag Signals for Adaptive $k - \tau$ Model at $\alpha = 20°$ and $Re_c = 10^5$.

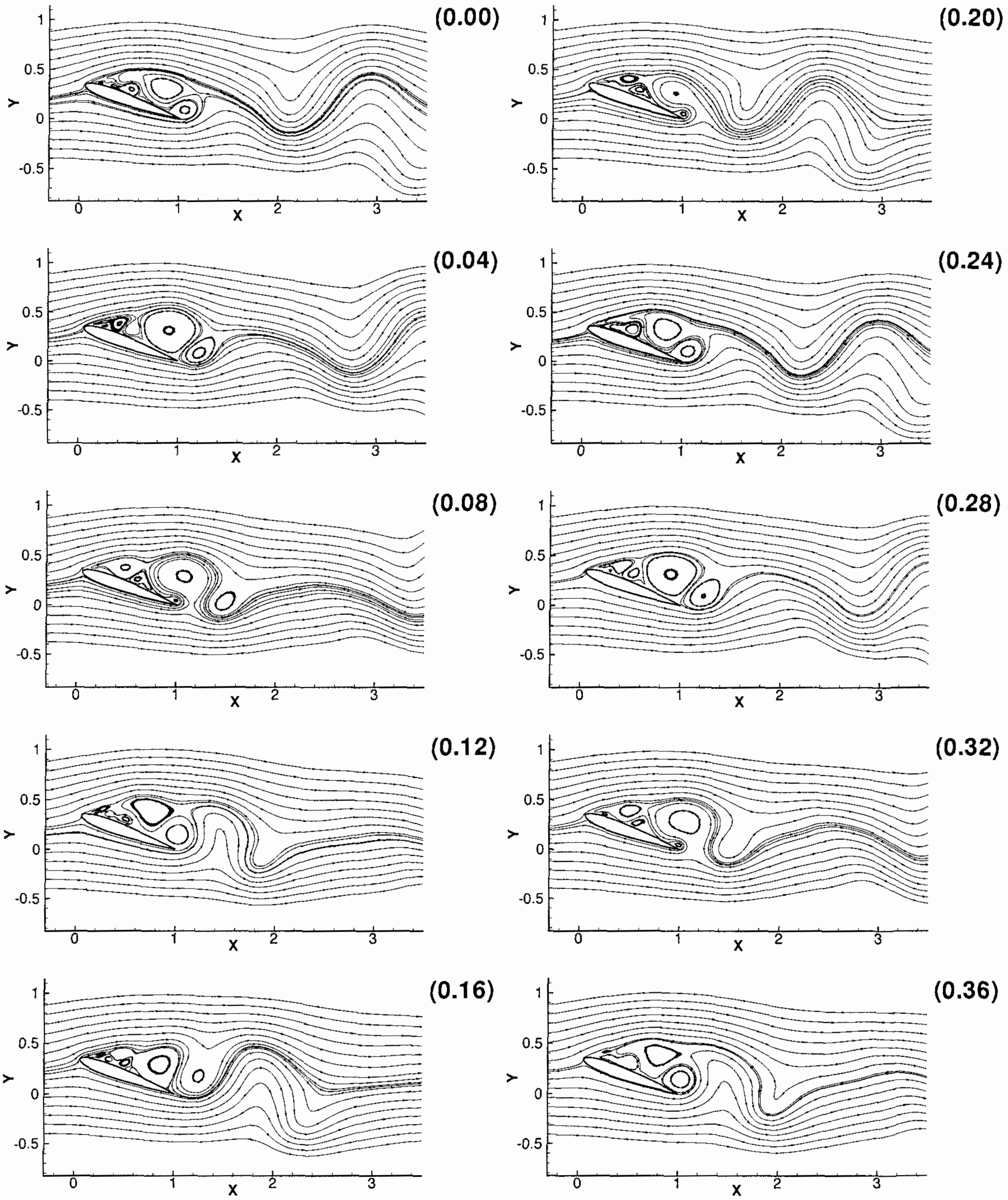

Figure 4.13: Velocity Streamlines for Adaptive $k-\tau$ Model at $\alpha = 20^\circ$ and $Re_c = 10^5$.

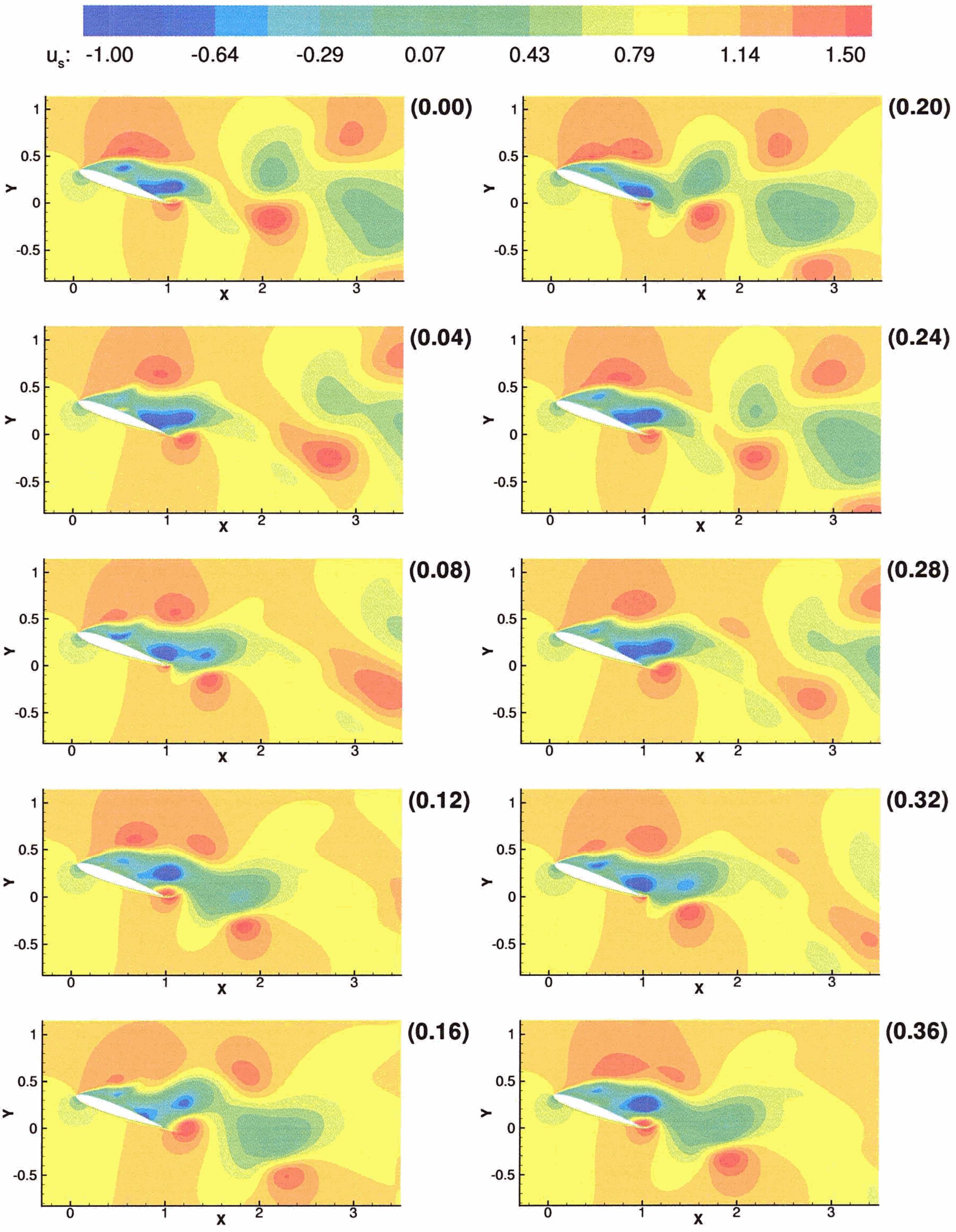

Figure 4.14: u/U_∞ Velocity Contours for Adaptive $k-\tau$ Model at $\alpha = 20°$ and $Re_c = 10^5$.

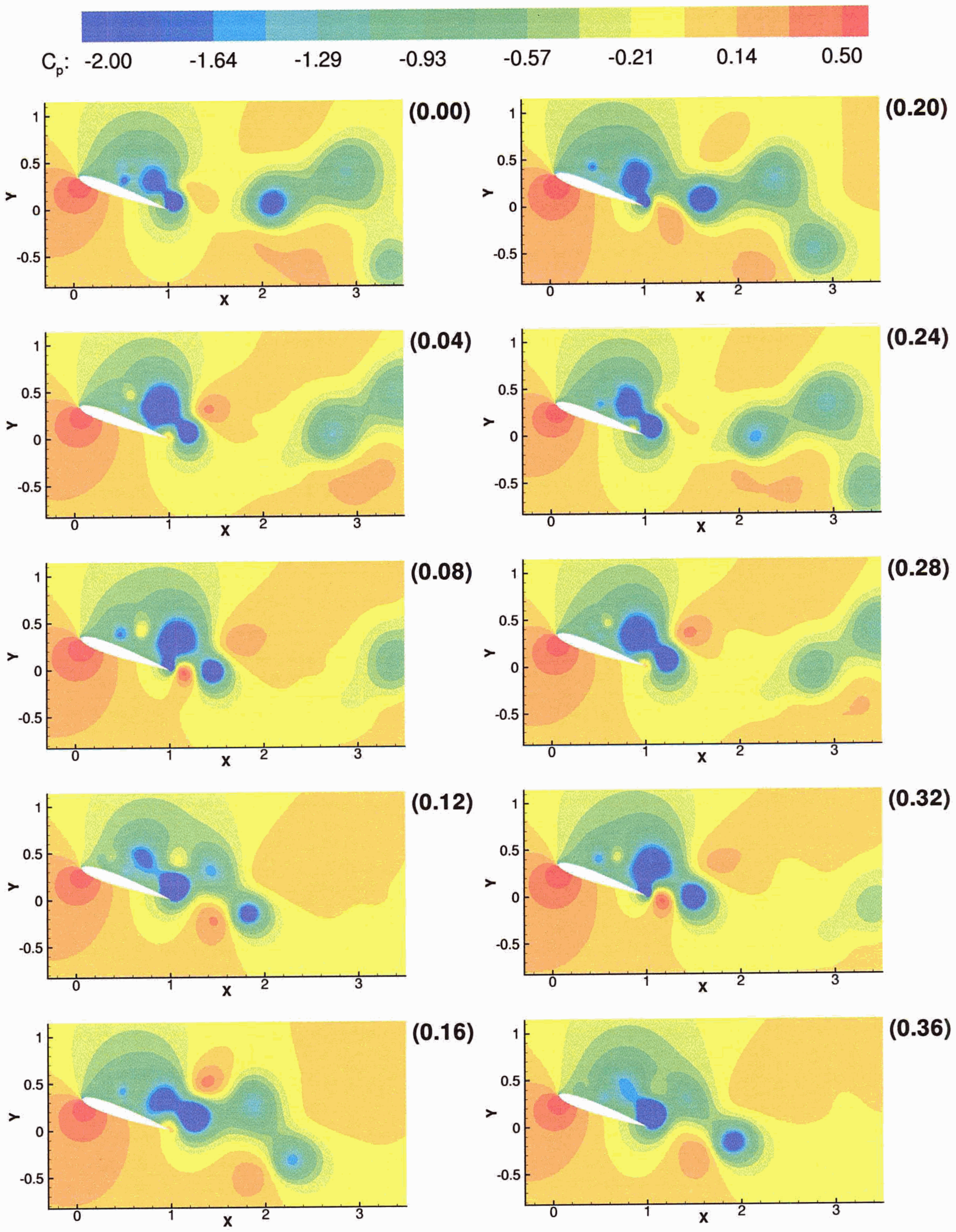

Figure 4.15: Pressure Contours for Adaptive $k-\tau$ Model at $\alpha = 20°$ and $Re_c = 10^5$.

Figures 4.16, 4.17 and 4.18 show the eddy viscosity ratio, turbulent time scale and turbulent kinetic energy ratio contours. The eddy viscosity contours are much more complex than those obtained with the KTS model. Note however that the magnitude of the eddy viscosity is much smaller with a maximum in the near wake of $\frac{\mu_t}{\mu} \approx 60$. The lower eddy viscosities, obtained with the AKT model, indicate a less dissipative model and therefore allow richer dynamic features. The turbulent time scale is approximately 0.01 seconds in the separation zone ($x/c = 0.1$ to $x/c = 1.0$) and rises to 0.1 seconds in the wake. The turbulent kinetic energy peaks at the leading edge at the separation point $x/c = 0.5$ and along the trailing edge from $x/c = 0.8$ to $x/c = 1.0$. The turbulent kinetic energy ratio has a maximum value of three in these regions; this is an order of magnitude less than the results obtained with the KTS model. Figure 4.19 shows the vorticity contours. The magnitude of the vorticity in the wake is similar to the KTS model. The very high vorticities (order 10^3) in the boundary layer are hidden by the contour scale limits. Again, the interest is in the wake vortex structures.

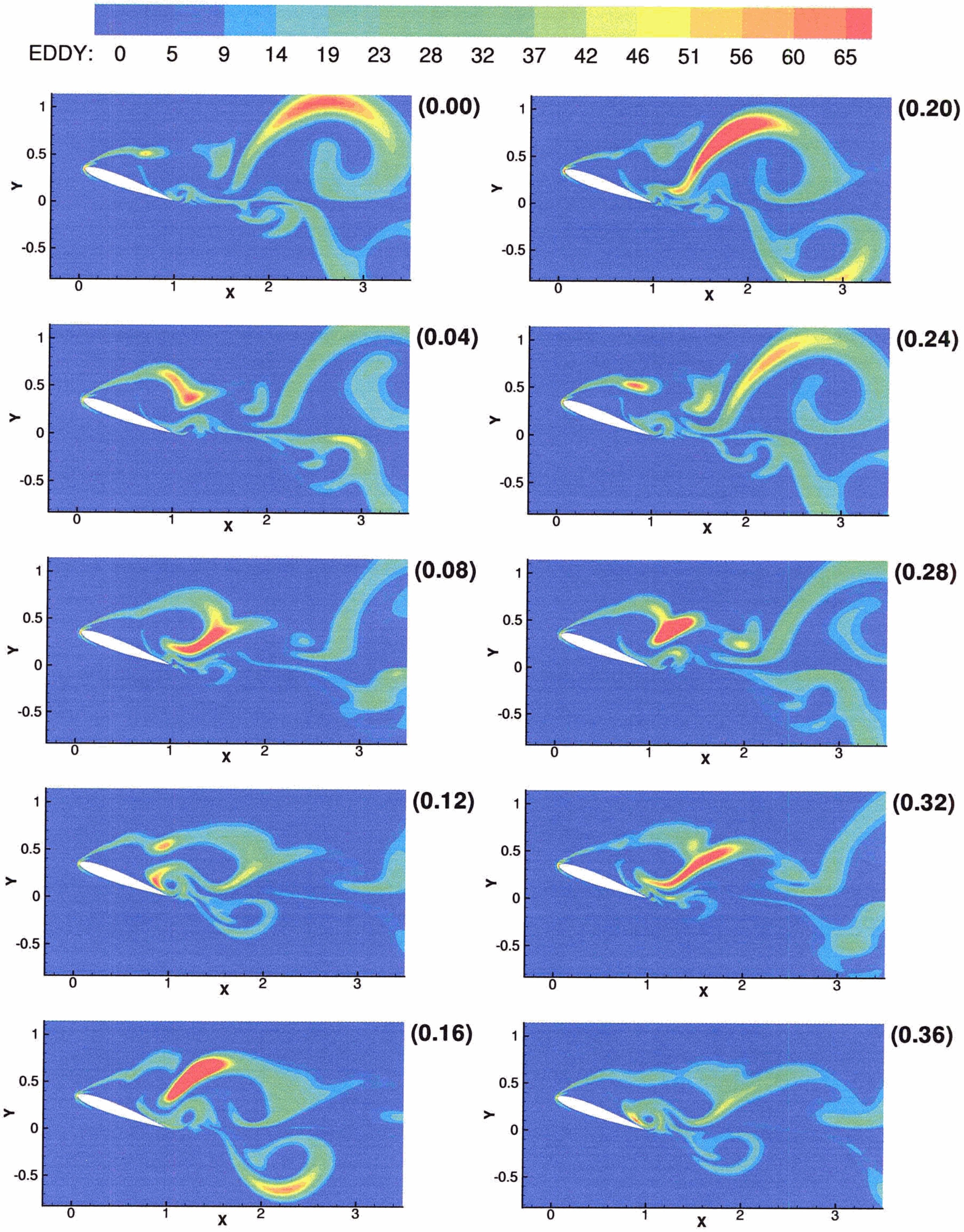

Figure 4.16: Eddy Viscosity Ratio $\frac{\mu_t}{\mu}$ Contours for Adaptive $k-\tau$ Model at $\alpha = 20°$ and $Re_c = 10^5$.

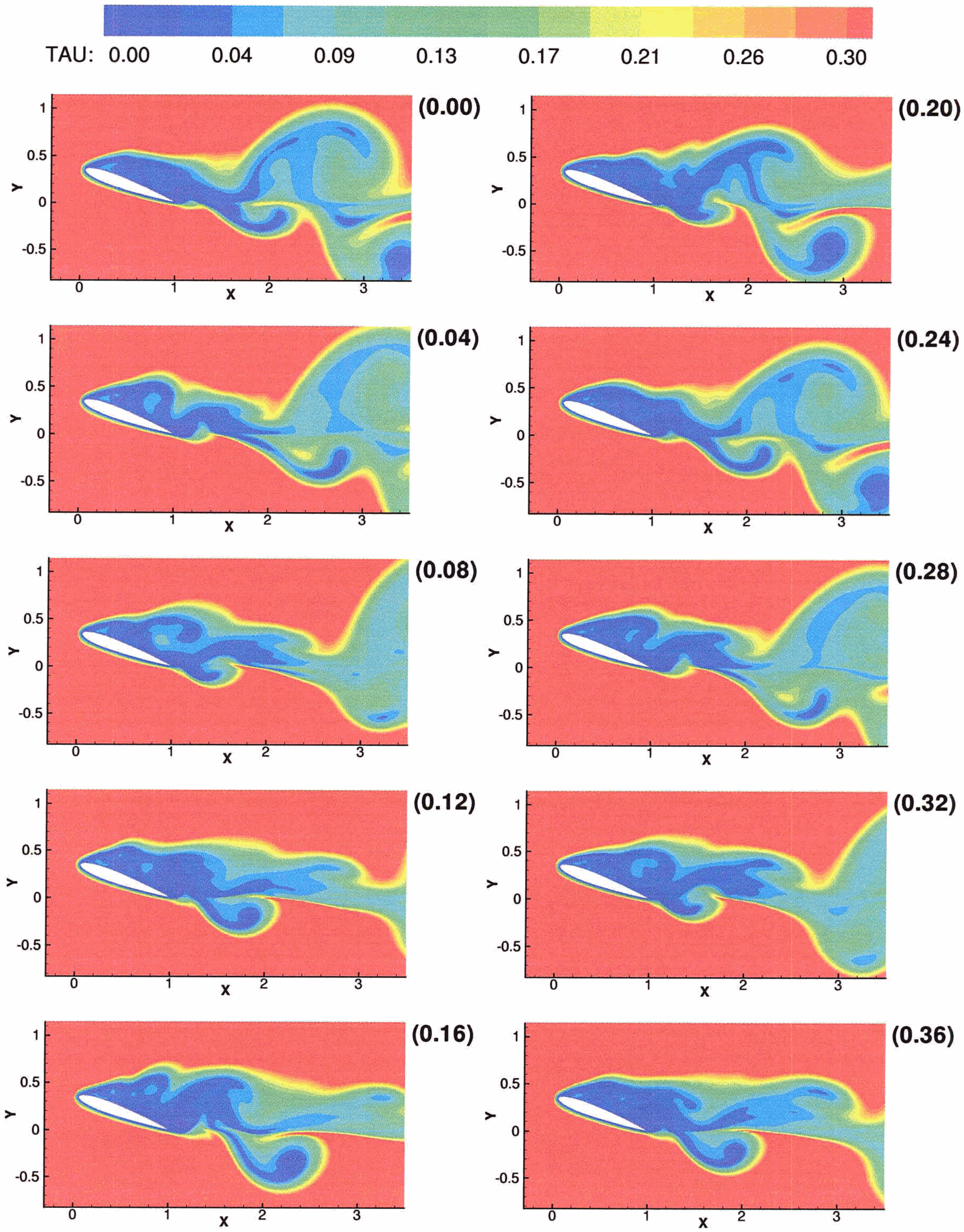

Figure 4.17: Turbulent Time Scale τ Contours in seconds for Adaptive $k - \tau$ Model at $\alpha = 20°$ and $Re_c = 10^5$.

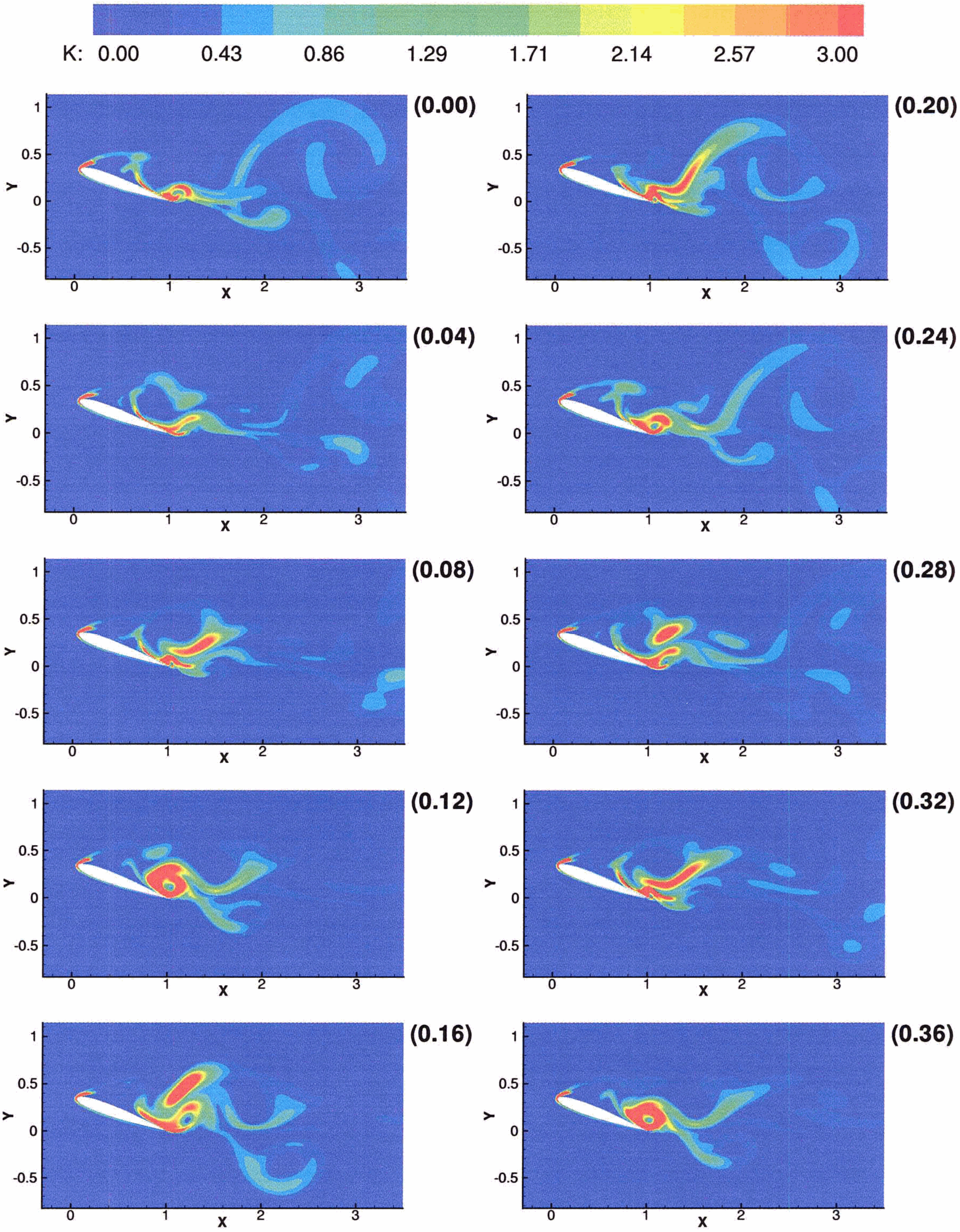

Figure 4.18: Turbulent Kinetic Energy Ratio (local to free stream) Contours for Adaptive $k - \tau$ Model at $\alpha = 20°$ and $Re_c = 10^5$.

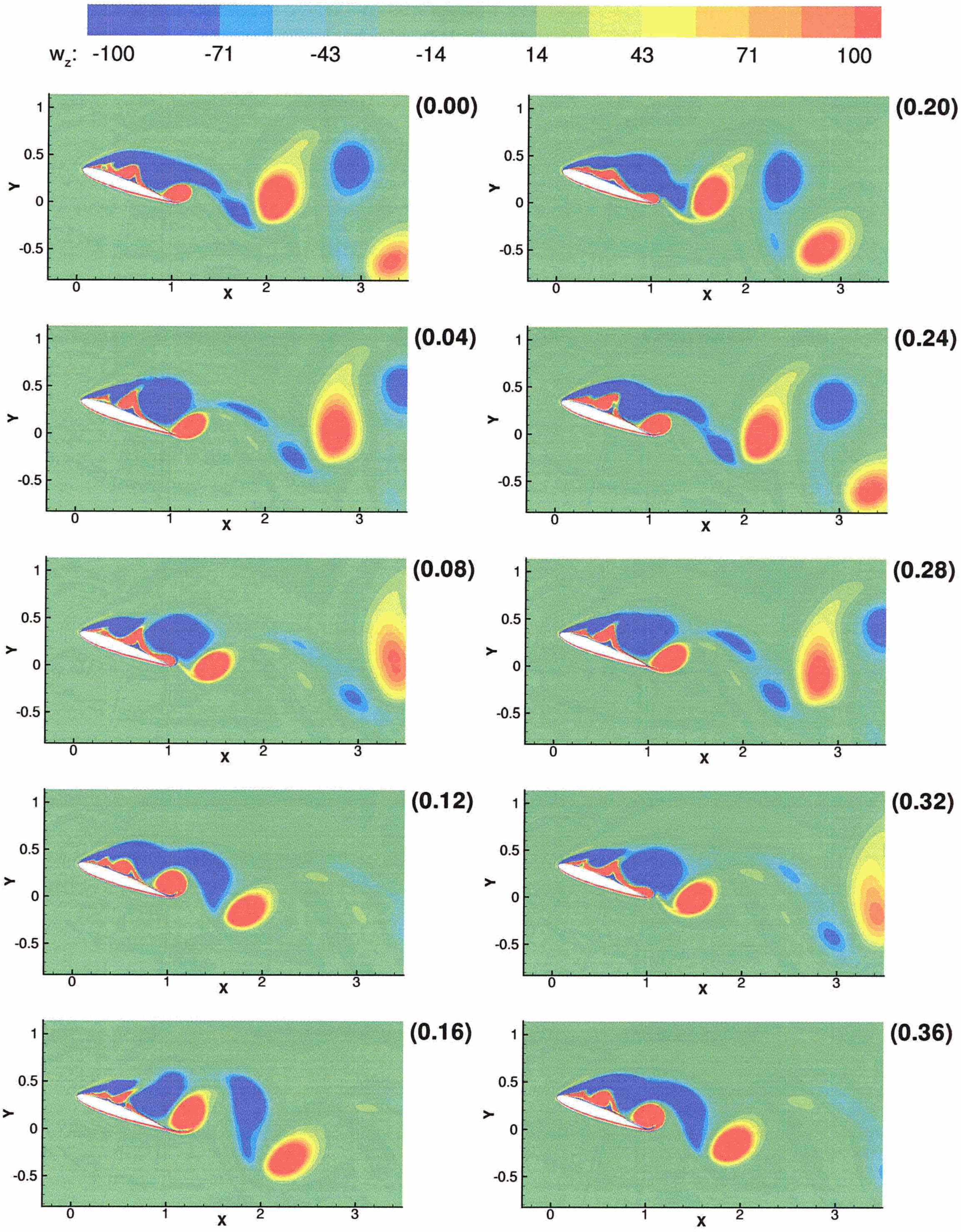

Figure 4.19: Vorticity Contours for Adaptive $k-\tau$ Model at $\alpha = 20°$ and $Re_c = 10^5$.

4.4 Comparison of Lift and Drag Signals

Lift (C_l) and drag (C_d) signals for the Speziale $k - \tau$ (KTS), adaptive $k - \tau$ (AKT) and Spalart Allmaras (SA) models at $Re_c = 10^5$ and $\alpha = 20°$ are presented in figure 4.20. As discussed earlier, the high dissipation associated with the SA model yields a steady state solution only. The AKT model gives the largest signal amplitude ($0.55 < C_l < 1.45$), ($0.3 < C_d < 0.6$) compared to the KTS model with ($0.8 < C_l < 0.9$), ($0.32 < C_d < 0.34$).

The period of the KTS model is approximately 0.1 seconds. The period for the AKT model has greater variation but is also approximately 0.1 seconds. The Strouhal number for the models is calculated based on the projected length of the airfoil normal to the free stream, the shedding period T and the free stream velocity U_∞:

$$St = \frac{c \sin \alpha}{T U_\infty} \tag{4.1}$$

This yields a Strouhal number of 0.19 for the KTS model and 0.17 for the AKT model. Experimentally, bluff bodies, including airfoils at high angles of attack, have Strouhal numbers of approximately 0.21; this is slightly higher than predicted here.

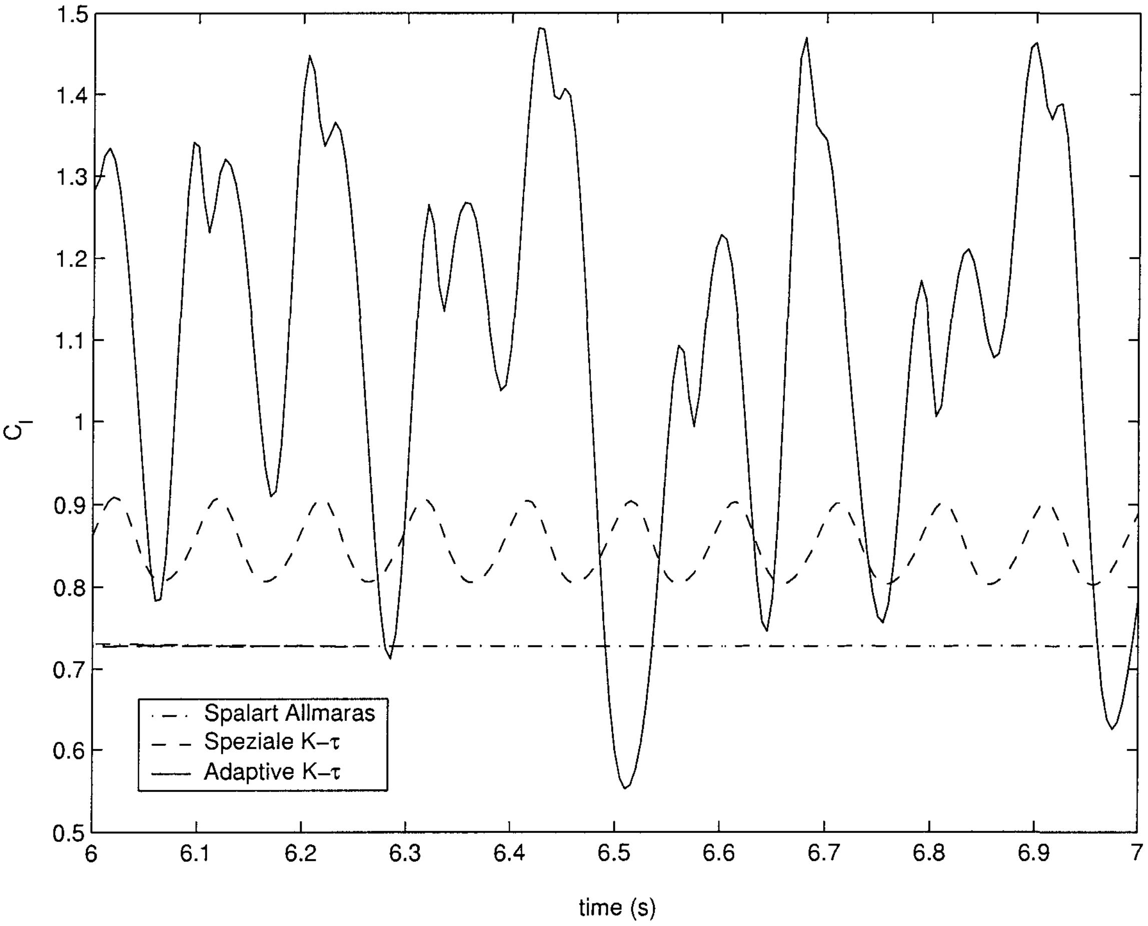

Figure 4.20: Comparison of Unsteady Lift Signals for Spalart Allmaras, Speziale $k-\tau$ and Adaptive $k-\tau$ models at $\alpha = 20°$ and $Re_c = 10^5$.

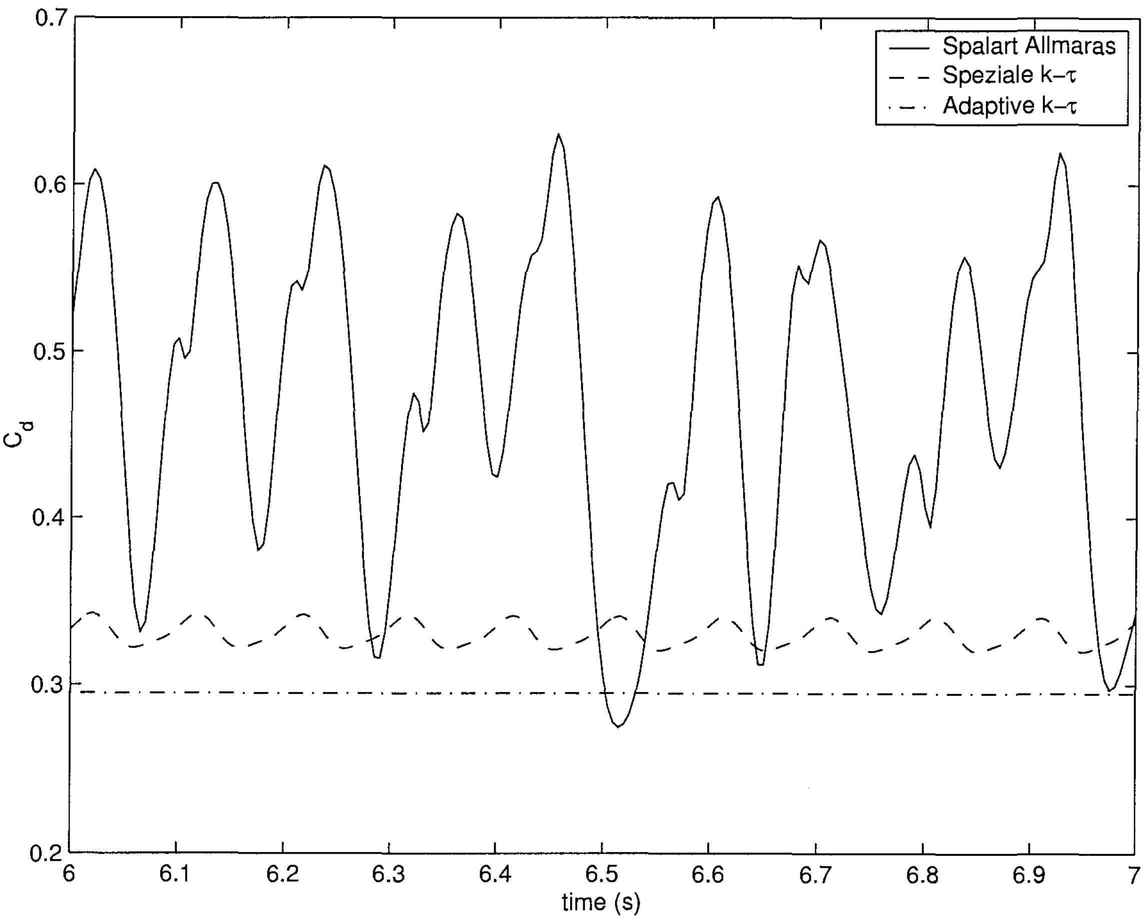

Figure 4.21: Comparison of Unsteady Drag Signals for Spalart Allmaras, Speziale $k - \tau$ and Adaptive $k - \tau$ models at $\alpha = 20°$ and $Re_c = 10^5$.

4.5 Comparison of Time Averaged Contour Plots

Plots of the time averaged streamlines, velocity, pressure, eddy viscosity, turbulent time scale and turbulent kinetic energy are presented. Averaging was done over 2000 time steps; this removes the effect of the starting and stopping points in the vortex shedding cycle. Time averaging was done only for the KTS and AKT models; the steady results of the SA model are presented directly. Turbulent time scale and turbulent kinetic energy ratio plots are only available for the KTS and AKT models; the SA model does not use these quantities.

Time averaged velocity stream lines are shown in figure 4.22. The SA model yields a large clockwise rotating vortex between $x/c = 0.2$ and $x/c = 1.4$. There is also a secondary counter-rotating vortex below the main vortex at the trailing edge at $x/c = 0.9$ to $x/c = 1.4$. The KTS model also yields two vortices, one clockwise rotating between $x/c = 0.1$ and $x/c = 1.1$ and the other counterclockwise rotating at $x/c = 1.0$ to $x/c = 1.4$. These vortices do not overlap as in the SA model; the larger vortex does not extend past the trailing edge. Multiple vortex structures are obtained with the AKT model. There is a large clockwise rotating vortex at the trailing edge between $x/c = 0.6$ and $x/c = 1.3$ followed by a smaller counterclockwise rotating vortex between $x/c = 1.2$ and $x/c = 1.6$. There are several smaller vortices near the leading edge including a small counterclockwise vortex on the airfoil surface between $x/c = 0.2$ and $x/c = 0.3$. There is a clockwise rotating vortex between $x/c = 0.1$ and $x/c = 0.5$ located above the surface vortex, and another counterclockwise rotating vortex downstream of it from $x/c = 0.4$ to $x/c = 0.7$.

Averaged velocity contours in figure 4.23 show that the SA and KTS models produce similar results. The AKT model predicts higher negative velocities in the trailing edge region ($U/U_\infty = -0.6$) from $x/c = 0.8$ to $x/c = 1.1$ compared to the

KTS and SA models ($U/U_\infty = -0.2$). This is likely associated with the strong vortex at this location. There is a second smaller area of low velocity predicted by the AKT model at $x/c = 0.3$ to $x/c = 0.5$ that is missed by the SA and KTS models. A region of low velocity is associated with the centre of each of the major vortices.

Pressure contours are shown in figure 4.24; the SA and KTS models produce similar results. The AKT model yields a low pressure region at the trailing edge that is missed by the other models.

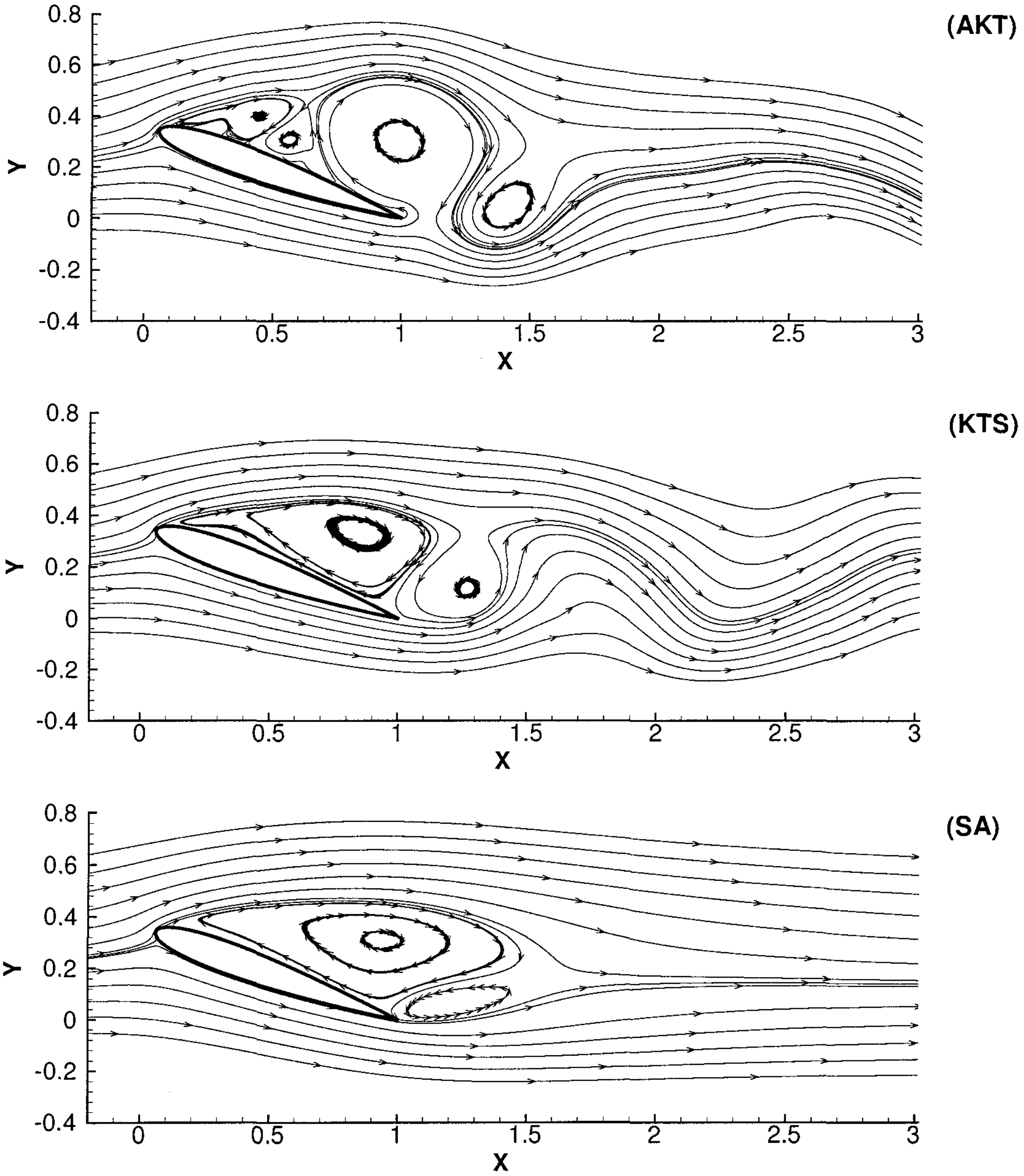

Figure 4.22: Comparison of Time Averaged Velocity Streamlines for Spalart Allmaras (SA), Speziale $k-\tau$ (KTS) and Adaptive $k-\tau$ (AKT) models at $\alpha = 20°$ and $Re_c = 10^5$.

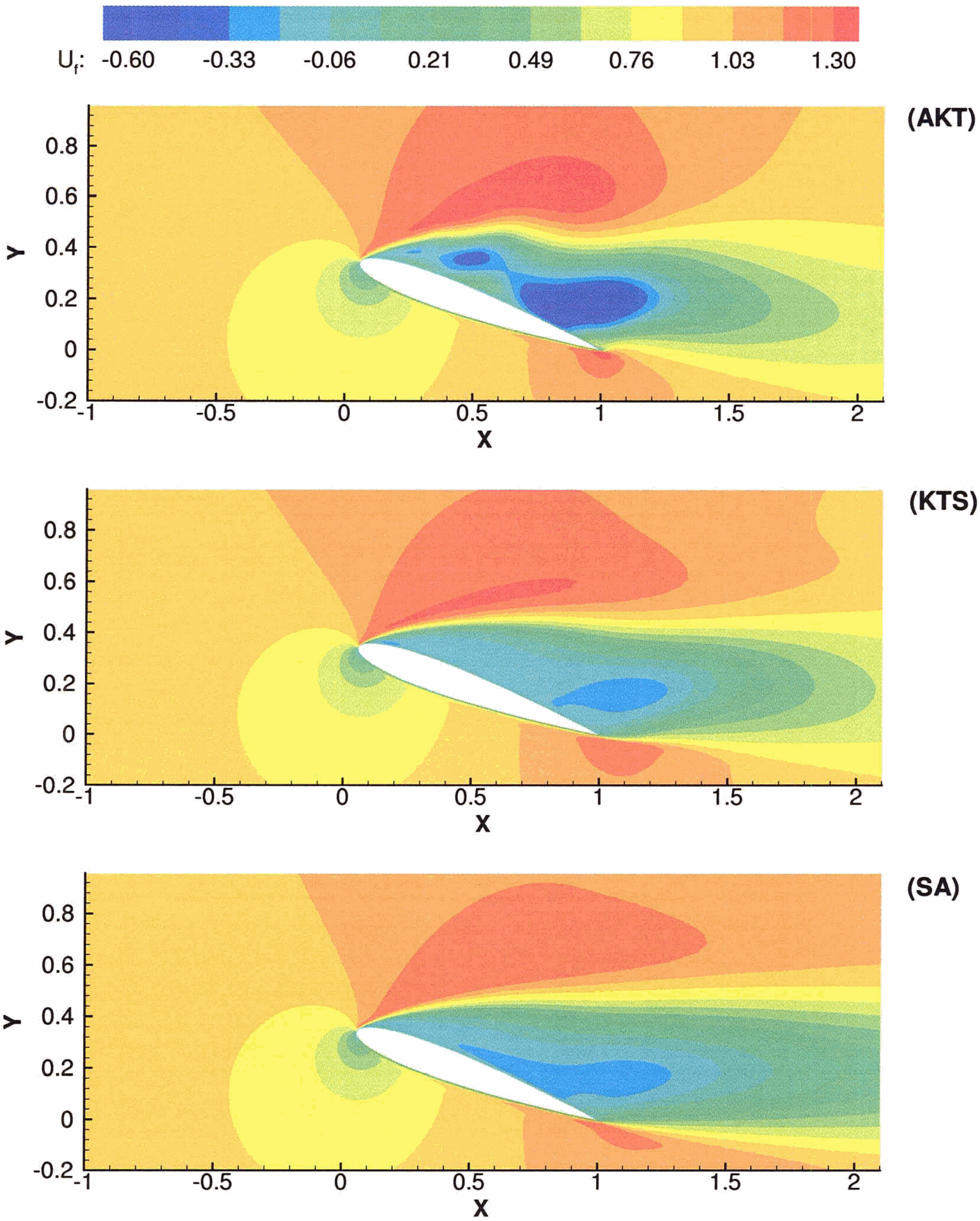

Figure 4.23: Comparison of Time Averaged U/U_∞ Velocity for Spalart Allmaras (SA), Speziale $k-\tau$ (KTS) and Adaptive $k-\tau$ (AKT) models at $\alpha = 20°$ and $Re_c = 10^5$.

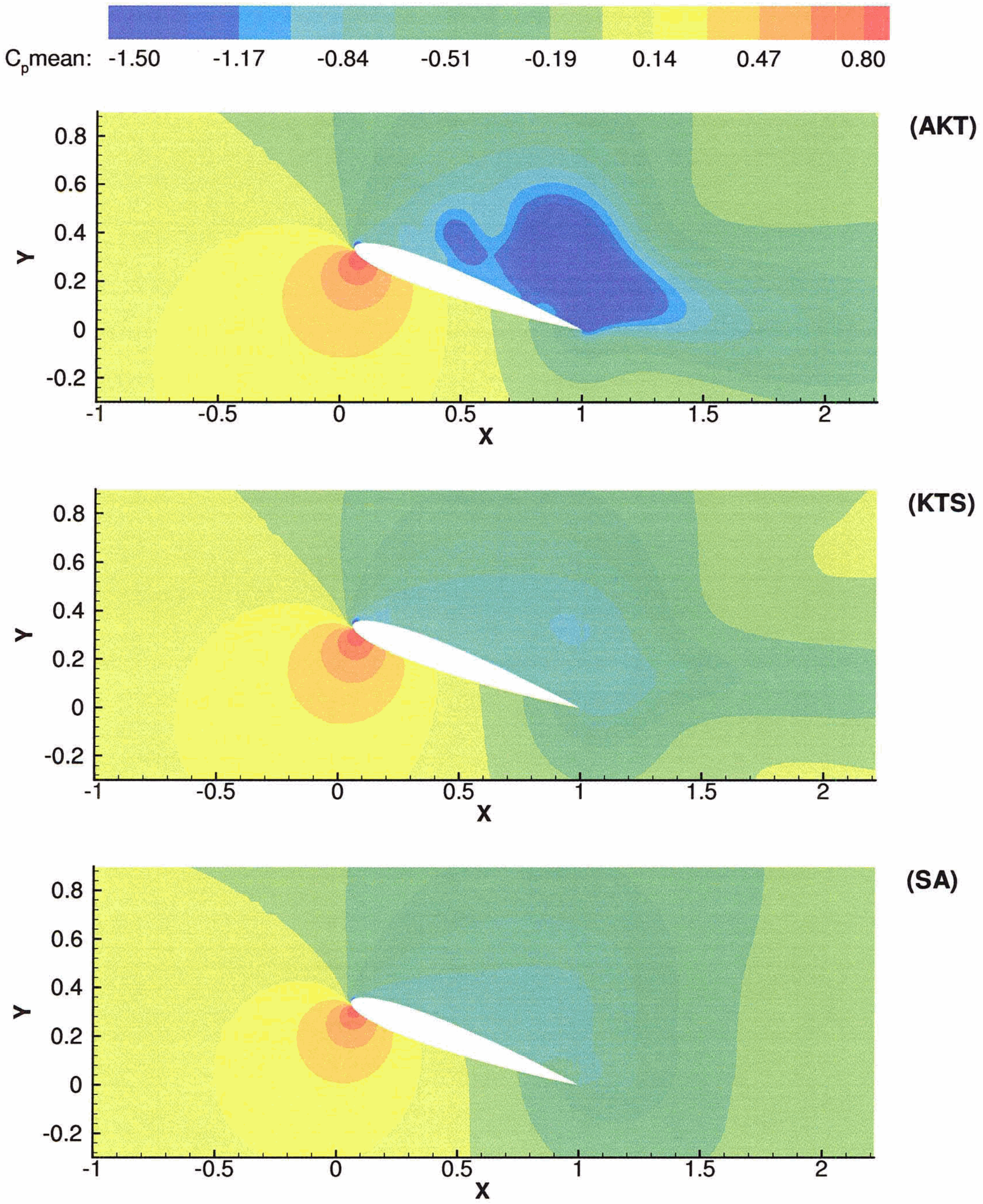

Figure 4.24: Comparison of Time Averaged Pressure Coefficient C_p for SA, KTS and AKT Models at $\alpha = 20°$ and $Re_c = 10^5$.

Figure 4.25 shows eddy viscosity contours. The SA and KTS models use the same contour level scale; the AKT model has its own scale. Note that the AKT model yields eddy viscosities in the separated region and in the wake which are an order of magnitude lower (max of $\frac{\mu_t}{\mu} \approx 60$) than those of the KTS and SA models (max $\frac{\mu_t}{\mu} \approx 900$ and $\frac{\mu_t}{\mu} \approx 1000$ respectively).The lower eddy viscosities of the AKT model produce simulations akin to *Large Eddy Simulations* where the role of turbulence modelling is confined to the subgrid scale fluctuations. Indeed the AKT model produces richer dynamics and a broader range of vortices as illustrated in figure 4.22. The KTS and SA models predict two vortex regions only. Since the AKT model resolves more of the turbulent structures directly, it is not necessary to account for their average effect through an increase in eddy viscosity.

Turbulent time scale and turbulent kinetic energy ratio plots for the AKT and KTS models are shown in figures 4.26 and 4.27 respectively. The turbulent kinetic energy ratio is similar for both models at the leading edge in the adverse pressure gradient region ($x/c \approx 0.05$). From $x/c = 0.2$ and downstream in the wake, the turbulent kinetic energy is much higher for the KTS model (approximately 15). There is no appreciable difference between the free stream and wake turbulent kinetic energy in the AKT model for $x/c > 1.4$. The time average vorticity is shown in figure 4.28; the KTS and SA models give similar results while the AKT model yields more complicated vortex structures in the separated region from $x/c = 0$ to $x/c = 1$. All models show negative vorticity (clockwise) originating from the leading edge and positive vorticity (counterclockwise) origination from the trailing edge.

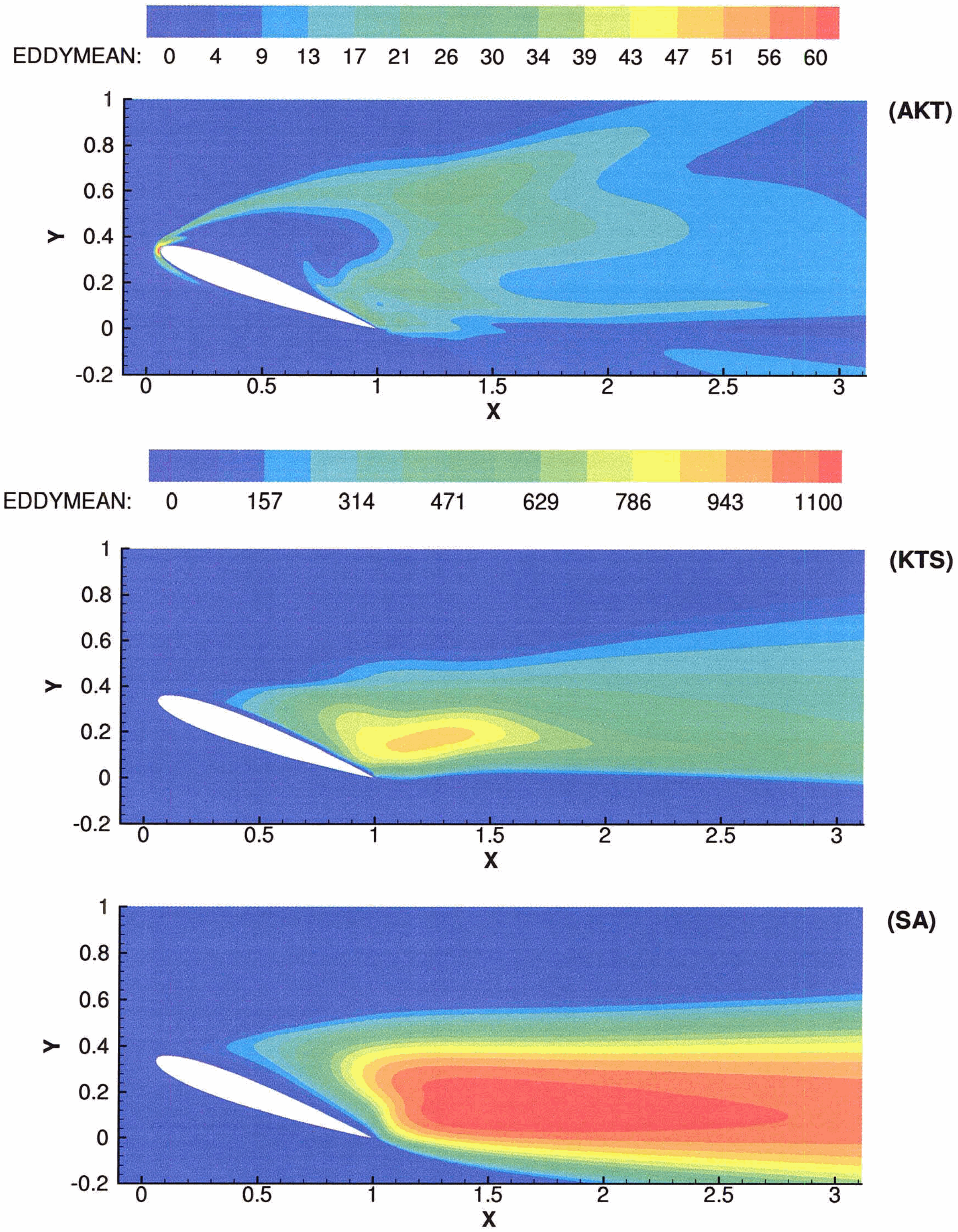

Figure 4.25: Comparison of Time Averaged Eddy Viscosity Ratio $\frac{\mu_t}{\mu}$ for Spalart Allmaras (SA), Speziale $k-\tau$ (KTS) and Adaptive $k-\tau$ (AKT) models at $\alpha = 20°$ and $Re_c = 10^5$. Upper contour legend applies to AKT; lower contour legend applies to KTS and SA.

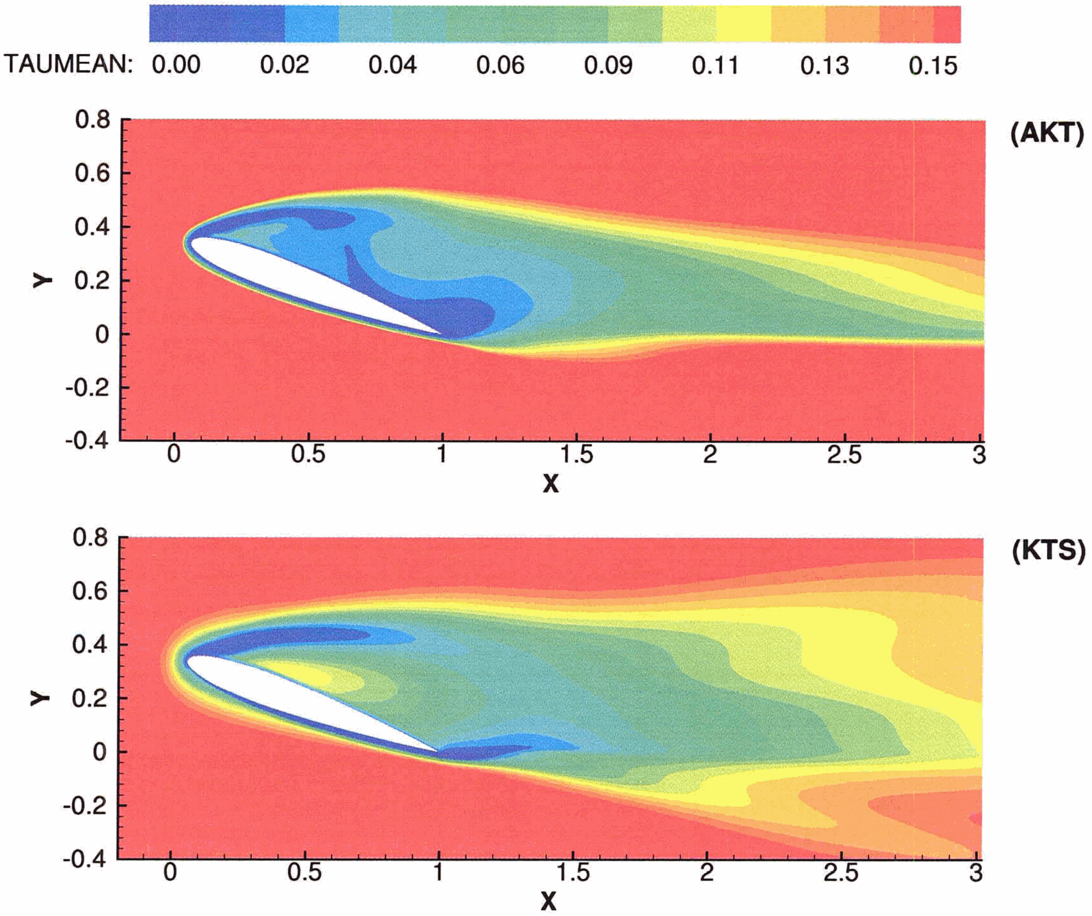

Figure 4.26: Comparison of Time Averaged Turbulent Time Scale for Speziale $k-\tau$ (KTS) and Adaptive $k-\tau$ (AKT) models at $\alpha = 20°$ and $Re_c = 10^5$.

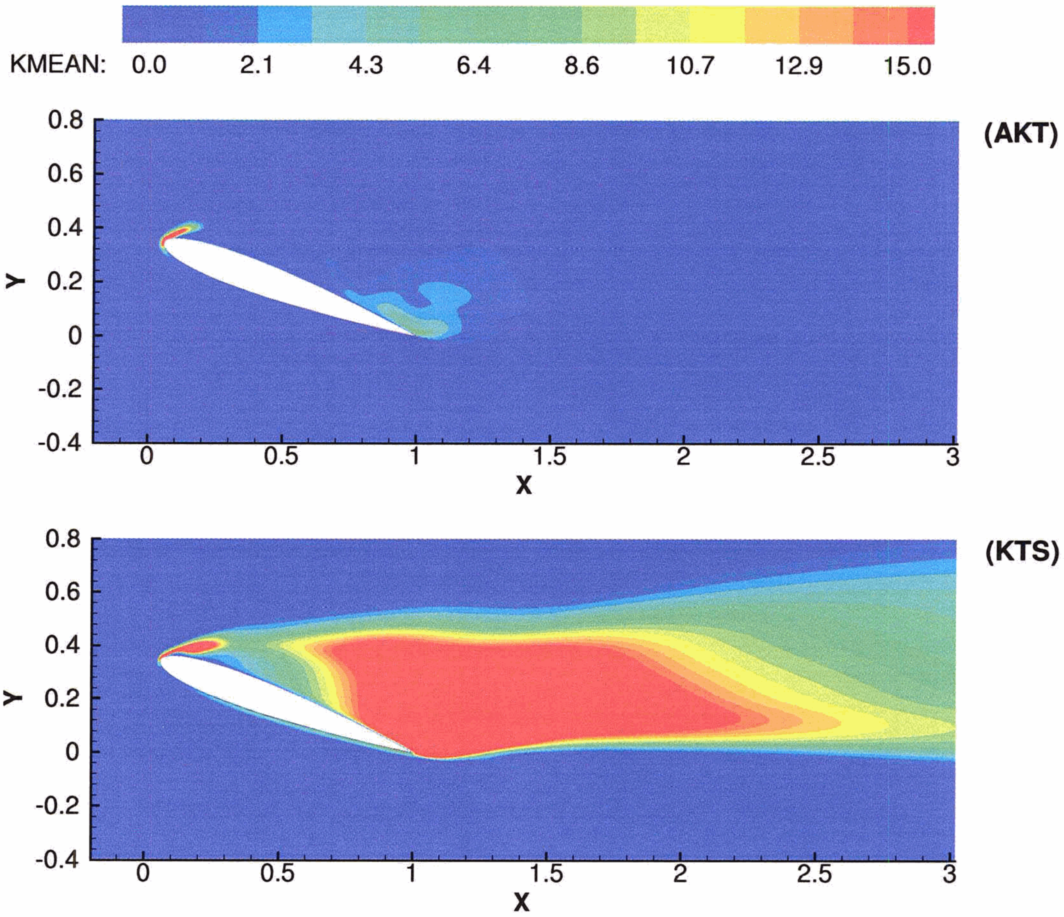

Figure 4.27: Comparison of Time Averaged Turbulent Kinetic Energy Ratio for Speziale $k-\tau$ (KTS) and Adaptive $k-\tau$ (AKT) models at $\alpha = 20°$ and $Re_c = 10^5$.

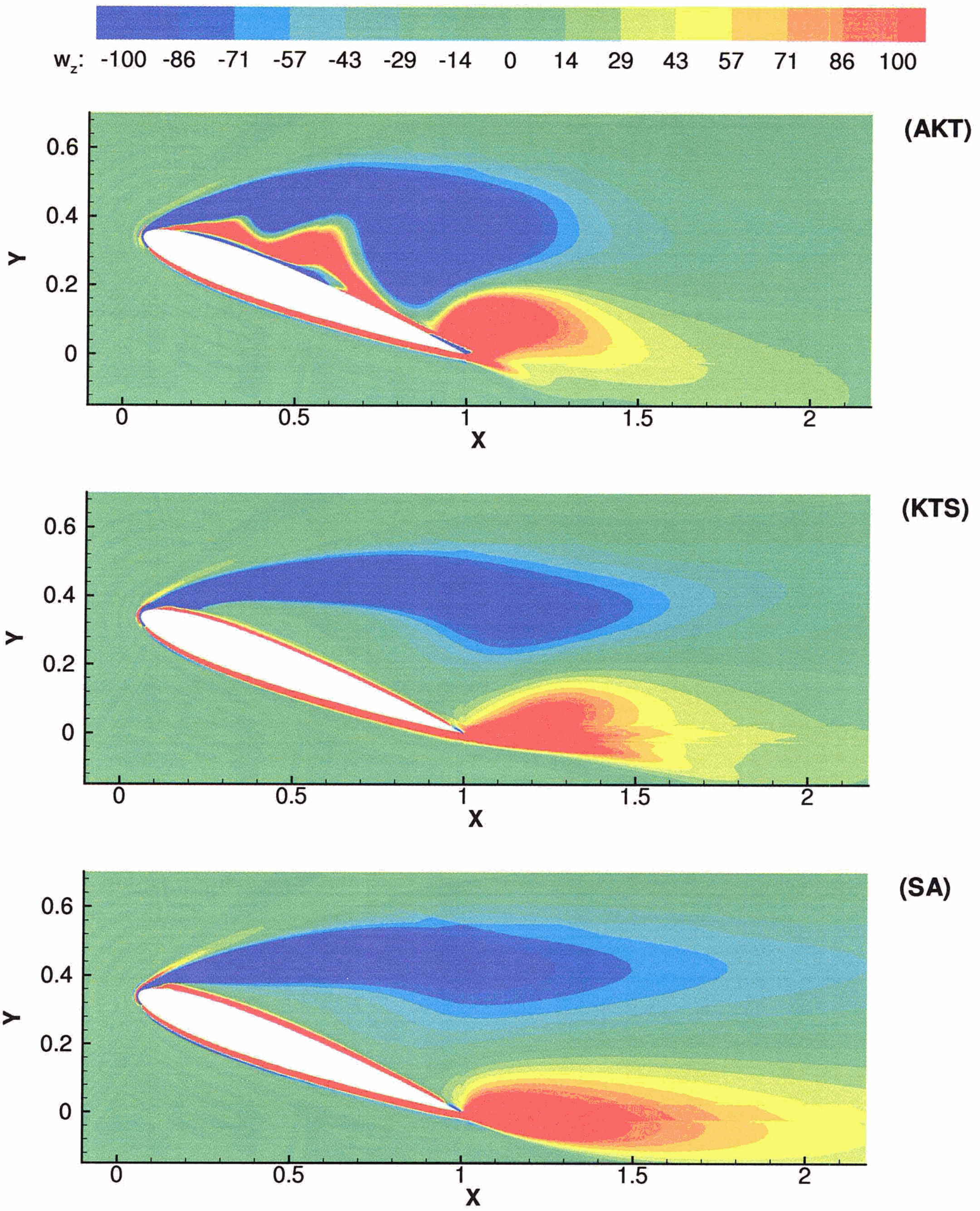

Figure 4.28: Comparison of Time Averaged Vorticity for Speziale Adaptive $k-\tau$ (AKT), Speziale $k-\tau$ (KTS) and Spalart Allmaras (SA) models at $\alpha = 20°$ and $Re_c = 10^5$.

4.6 Summary

The results of unsteady simulations carried out at $\alpha = 20°$ and $Re_c = 10^5$ are presented in this chapter for the Speziale $k - \tau$ and adaptive $k - \tau$ models. Snapshots of the flow streamlines, velocity, pressure, eddy viscosity, turbulent time scale, turbulent kinetic energy and vorticity contours are presented for each cycle to allow visualization of the vortex shedding phenomenon. The Speziale $k - \tau$ model yields a periodic lift and drag signal; the adaptive $k - \tau$ model yields a more complicated non-repeating signal.

The Spalart Allmaras model converged to a steady solution when run in unsteady mode. The unsteady results of the Speziale $k - \tau$ and adaptive $k - \tau$ models are averaged in time and compared with the steady results of the Spalart Allmaras model. Both the Spallart Allmaras and Speziale $k - \tau$ models predict eddy viscosities in the near wake and in the separated regions on the upper side of the airfoil which are an order of magnitude higher than predicted by the adaptive $k - \tau$ model. The adaptive model predicts a more complicated flow field with richer flow physics than the other models; resolution of additional flow structures may account for the reduction in eddy viscosity since eddy viscosity accounts for unresolved turbulence.

Chapter 5

Conclusions

Simulations of turbulent flow over a NACA 0012 airfoil have been conducted in this work with an emphasis on assessing the turbulence modelling capabilities of the research code SPARC. The goal is to use this research in more complicated CFD code fluid-structure interaction and airfoil optimization problems at the University of Victoria.

Simulations were carried out in two parts; the first part focused on steady state simulations at a high Reynolds number ($Re_c = 3 \times 10^6$) and angles of attack ranging from 0° to 18° while the second part focused on unsteady time dependent simulations at $Re_c = 10^5$ and $\alpha = 20^\circ$.

The objective of the steady simulations was to validate the lift, pressure drag and friction drag predictions of the turbulence models using experimental data. Simulations were carried out with the Spalart Allmaras one equation and the Speziale $k - \tau$ two equation turbulence models. Results from both models are found to be quite sensitive to initial and boundary conditions as well as the grid resolution. Since wall functions are not used to approximate the velocity profile in the boundary layer, proper resolution of the laminar sublayer is critical for accurate shear stress prediction. This requires that the first grid point from the wall be located at $y^+ \leq 1$. Convergence difficulties may be encountered at the outlet of the computational domain due to high cell aspect ratios caused by the very fine grid resolution at the airfoil wall. Flaring the domain in the cross stream direction at the outlet to keep cell aspect ratios under 400 prevents convergence problems.

The Spalart Allmaras model works well if the free stream eddy viscosity ratio is low, preferably less than 10^{-7}. Higher eddy viscosities influence the location of the turbulent transition point at the leading edge and therefore the shear stress distribution. Though the original form of the model in the paper by Spalart and Allmaras [21] includes a tripping function which allows the transition point to be specified by the user, this feature has not been implemented in SPARC. This caused some concern as turbulence models are generally unreliable in predicting the transition point. Future work with this model should include an implementation of the tripping function.

Since the Speziale $k-\tau$ model uses two additional transport equations rather than the single eddy viscosity transport equation in the Spalart Allmaras model, the free stream turbulent intensity must be specified in addition to the eddy viscosity. The turbulent intensity is set to 0.3% which is a typical value encountered in most wind tunnels. Convergence was only obtained for an eddy viscosity near 1.0.

Both the Spalart Allmaras and Speziale $k - \tau$ models give accurate results until stall is approached. Both models under predict lift and drag at stall. Neither model converged in the unsteady regime past stall. This may be a limitation of SPARC as it does not allow steady simulations to converge when large scale unsteady phenomena are present.

Unsteady simulations were carried out in the second part of this work at $\alpha = 20°$ and $Re_c = 10^5$. The lower Reynolds number was selected due to the limited computational resources available. Nevertheless, there is interest in airfoil data at low Reynolds numbers where there is little experimental data. Gliders, unmanned aircraft and aircraft operating at very high altitudes (greater than 100,000 feet) are typical applications.

A grid study was not carried out for the low Reynolds number simulations. The grid from the first part of this work was used with the grid resolution at the wall adjusted to again obtain $y^+ \approx 1$ at the first grid point. Additional grid points were also added along the upper airfoil surface in the vortex shedding region. The interest is more in a qualitative view of the vortex shedding phenomena rather than an exact prediction of the lift and drag coefficients, which are highly dependent on the turbulence model in the post stall regime.

The Spalart Allmaras model did not yield any unsteady phenomena when run in unsteady mode; it is tuned in SPARC for steady simulations. The Speziale $k-\tau$ model yielded periodic lift and drag signals where large counter rotating vortices were shed at every cycle. Considerably more complex results were obtained with the adaptive $k-\tau$ model of Magagnato [7]. This model is a hybrid between RANS and LES; in steady state coarse grid simulations it reverts to a RANS simulation whereas in an unsteady 3D fine grid simulations, it approaches a DNS. Transient, non-periodic lift and drag signals were obtained as well as a complicated flow field with multiple separation bubbles. The eddy viscosity in the separated region and the wake is an order of magnitude lower for the adaptive $k-\tau$ model than it is for the Spalart Allarmas and Speziale $k-\tau$ models; this is attributed to resolving turbulent structures (multiple vortices) rather than accounting for them through an increased eddy viscosity.

Summarizing, three turbulence models have been evaluated in steady and unsteady flows in SPARC. Their ability to predict lift, pressure drag, friction drag and unsteady vortex shedding phenomena has been demonstrated. While the Spalart Allmaras model yields good results at high Reynolds numbers in steady state at low to moderate angles of attack, it under predicts drag near stall. The Speziale $k-\tau$ model yielded results similar to the Spalart Allmaras model in the steady simulations but was able to capture some of the vortex shedding phenomena in the unsteady solutions. Overall, the adaptive $k-\tau$ model yielded the most physically plausible results with richer dynamics and broader range of vortices at a reasonable computational cost. This model is recommended for future research at the University of Victoria where high angles of attack and vortex shedding phenomena will likely be encountered.

References

[1] G. Lombardi; M.V. Salvetti; D. Pinelli. Numerical evaluation of airfoil friction drag. *Journal of Aircraft, Engineering Notes*, 37(2):354–356, 1999.

[2] T. von Karman. Turbulence and skin friction. *Journal of the Aeronautical Sciences*, 1(1):47–66, January 1934.

[3] S.L. Yang; Y.L. Chang; O. Arici. Post-stall navier-stokes computations of the nrel airfoil using a $k-\omega$ turbulence model. *Wind Energy ASME*, 16:127–136, 1995.

[4] J.T. Barton; T.H. Pulliam. Airfoil computation at high angle of attack, inviscid and viscous phenomena. *AIAA Journal*, 24(5):705–712, May 1986.

[5] P.R. Spalart. Strategies for turbulence modelling and simulations. *International Journal of Heat and Fluid Flow*, 21:252–263, 2000.

[6] J.C. Muti Lin; L.L. Pauley. Low-reynolds-number separation on an airfoil. *AIAA Journal*, 34(8):1570–1577, August 1996.

[7] F. Magagnato; M. Gabi. A new adaptive turbulence model for unsteady flow fields in rotating machinery. *International Journal of Rotating Machinery*, 8(3):175–183, 2002.

[8] P. Hamroy D. Greer. Design and predictions for a high-altitude (low-reynolds-number) aerodynamic flight experiment. Technical Report TM-1999-206579, NASA, 1999.

[9] F-B Hsiao; C-F Liu; Z. Tang. Aerodynamic performance and flow structure studies of a low reynolds number airfoil. *AIAA Journal*, 27(2), February 1989.

[10] F. Magagnato. *SPARC Structured PArallel Research Code.* Department of Fluid Machinery, University of Karlsruhe (TH), Kaiserstrasse 12,D-76131 Karlsruhe, Germany.

[11] G. Pedro. Hydrodynamics and fluid-structure interactions in swimming propulsion. Master's thesis, University of Victoria, 2001.

[12] M. Secanell. Shape optimization of a subsonic airfoil. Technical report, Dept. of Mechanical Engineering, University of Victoria, 2003.

[13] G. Pedro; A. Suleman; N. Djilali. A numerical study of the propulsive efficiency of a flapping hydrofoil. *International Journal of Numerical Methods in Fluids*, 42:493–526, 2003.

[14] E. Chaput. Aerospatiale-a airfoil. contribution in ecarp-european computational aerodynamics research project: Validation of cfd codes and assessment of turbulent model. *Notes on Numerical Fluid Mechanics, Vieweg Verlag*, 58:327–346, 1997.

[15] C. Weber; F. Ducros. Large eddy and reynolds-averaged navier-stokes simulations of turbulent flow over an airfoil. *IJCFD*, 13:327–355, 2000.

[16] L. Davidson. Navier-stokes stall predictions using an algebraic reynolds-stress model. *Journal of Spacecraft and Rockets*, 29(6):794–800, December 1992.

[17] C.M. Rhie; W.L. Chow. Numerical study of the turbulent flow past an airfoil with trailing edge separation. *AIAA Journal*, 21(11):1525–1532, November 1983.

[18] D.P. Rizzetta; M.R. Visbal. Comparative numerical study of two turbulence models for airfoil static and dynamic stall. *AIAA Journal*, 31(4):784–786, 1992.

[19] J.H. Ferziger; M. Perić. *Computational Methods for Fluid Dynamics.* Springer Verlag New York, third edition, 2002.

[20] C-J Chen; S-Y Jaw. *Fundamentals of Turbulence Modelling.* Taylor and Francis, Washington, D.C., 1998.

[21] P.R. Spalart; S.R. Allmaras. A one-equation turbulence model for aerodynamic flows. *AIAA Paper 92-0439*, 1992.

[22] C.G. Speziale; R. Abid; E.C. Anderson. Critical evaluation of two-equation models for near-wall turbulence. *AIAA Journal*, 30(2):324–331, 1992.

[23] L. Davidson. Prediction of the flow around an airfoil using a reynolds stress transport model. *Transactions of the ASME*, 117:50–57, March 1995.

[24] B.S. Baldwin; H. Lomax. Thin layer approximation and algebraic model for separated turbulent flows. In *AIAA 16th Aerospace Sciences Meeting*, number 78-257 in AIAA, Huntsville, Alabama, 1978.

[25] E. Zeidan; N. Djilali. Multiple-time-scale turbulence model computations of flow over a square rib. *AIAA Journal*, 34(3):626–629, 1996.

[26] P. Bradshaw. Turbulence: The chief outstanding difficulty of our subject. *Experiments in Fluids*, 16:203–216, 1994.

[27] S.J. Shamroth; H.J. Gibeling. Navier-stokes solution of the turbulent flowfield about an isolated airfoil. *AIAA Journal*, 18(12):1409–1410, December 1980.

[28] A. Roshko. On the drag and shedding frequency of two-dimensional bluff bodies. Technical Report NACA TN 3169, California Institute of Technology, 1954.

[29] R.D. Blevins. *Flow Induced Vibration.* Van Nostrand Reinhold, New York, second edition, 1990.

[30] N. Gregory; C.L. O'Reilly. Low-speed aerodynamic characteristics of naca 0012 aerofoil section, including the effects of upper surface roughness simulating hoar frost. Technical report, National Physical Laboratory Aerodynamics Division, 1970.

[31] K.B.M.Q. Zaman; D.J. McKinzie; C.L. Rumsey. A natural low-frequency oscillation of the flow over an airfoil near stalling conditions. *Journal of Fluid Mechanics*, 202:403–442, 1989.

[32] R.H. Pletcher; K-H Chen. On solving the compressible navier-stokes equations for unsteady flows at very low mach numbers. *AIAA*, (AIAA 93-3368).

[33] H. Schlichting. *Boundary-Layer Theory.* McGraw-Hill, sixth edition, 1968.

[34] F.M. White. *Fluid Mechanics.* WCB McGraw-Hill, fourth edition, 1999.

[35] U. Piomelli. *Large-eddy and Direct Simulation of Turbulent Flows.* Department of Mechanical Engineering, University of Maryland, University of Maryland, College Park, Maryland USA, 2001.

[36] T.J. Craft; B.E. Launder; K. Suga. Development and application of a cubic eddy-viscosity model of turbulence. *International Journal of Heat and Fluid Flow*, 17:108–115, 1995.

[37] T.J. Craft; B.E. Launder; K. Suga. Prediction of turbulent transitional phenomena with a nonlinear eddy-viscosity model. *International Journal of Heat and Fluid Flow*, 18:15–28, 1997.

[38] I.H. Abbott; A.E Von Doenhoff. *Theory of Wing Sections*. Dover Publications, New York, 1959.

[39] S.E. Rogers; N.L. Wiltberger; D. Kwak. Efficient simulation of incompressible viscous flow over single and multielement airfoils. *Journal of Aircraft*, 1993.

[40] E. Guilmineau; J. Piquet; P. Queutey. Two-dimensional turbulent viscous flow simulation past airfoils at fixed incidence. *Computers & Fluids*, 26(2):135–162, 1997.

[41] C.C. Critzos; H.H. Heyson; R.W. Boswinkle Jr. Aerodynamic characteristics of naca 0012 airfoil section at angles of attack from 0° to 180°. Technical Report NACA TN 3361, Langley Aeronautical Laboratory, 1955.

[42] P.J. Carpenter. Lift and profile-drag characteristics of an naca 0012 airfoil section as derived from measured helicopter-rotor hovering performance. Technical Report NACA TN 4357, Langley Aeronautical Laboratory, 1958.

[43] R. Horn; P.G. Vicente. Comprehensive analysis of turbulent flows around an naca 0012 profile, including dynamics stall effects. *International Journal of Computer Applications in Technology*, 11(3/4/5):230–251, 1998.

Appendix A

Model Definitions

A.1 Conservation of Mass and Momentum

For three dimensional motion, the velocity at a point can be written as a vector where $\hat{\imath}$, $\hat{\jmath}$ and $\hat{k}$ are the unit vectors in the x, y and z directions. The local velocity vector $\vec{U}$ is then defined as shown in equation (A.1) where u,v and w are the velocity components in the x, y and z directions respectively.

$$\vec{U} = u\hat{\imath} + v\hat{\jmath} + w\hat{k} \tag{A.1}$$

The first fundamental law from classical physics used in CFD is the conservation of mass: mass cannot be created or destroyed.

Conservation of mass states that difference between the rate of mass entering and leaving a control volume (cv) is equal to the rate change of mass in the control volume:

Rate of change of mass in cv = inlet mass flow - outlet mass flow

For an infinitesimally small control volume, the conservation of mass can be written as:

$$\frac{\partial \rho}{\partial t} = \frac{\partial}{\partial x}(\rho u) + \frac{\partial}{\partial y}(\rho v) + \frac{\partial}{\partial z}(\rho w) \tag{A.2}$$

Using the definition of the gradient operator,

$$\nabla = \hat{i}\frac{\partial}{\partial x} + \hat{j}\frac{\partial}{\partial y} + \hat{k}\frac{\partial}{\partial z}$$

the equation of continuity can be re-written in compact form:

$$\frac{\partial \rho}{\partial t} - \nabla \cdot \rho\vec{U} = 0 \tag{A.3}$$

Equation (A.3) is valid for unsteady, compressible flows. For the steady state, incompressible case where $\frac{\partial \rho}{\partial t} = 0$, continuity reduces to equation (A.4):

$$\nabla \cdot \rho\vec{U} = 0 \tag{A.4}$$

The second fundamental law is Newton's Second Law, $\vec{F} = m\vec{a}$, which states that the *net* force acting on an object is equal to the object's mass multiplied by its acceleration. $\vec{F}$ and $\vec{a}$ are vectors. The net force acting on an infinitesimal control volume can be written as:

Net force on control volume = Viscous forces on CV surface + Body forces in CV interior

$$\vec{F}_{net} = \vec{F}_{body} + \vec{F}_{surface}$$

Breaking the surface forces down into the x, y and z directions, they can be written as:

$$\frac{d\vec{F}_x}{dV} = -\frac{\partial P}{\partial x} + \frac{\partial}{\partial x}(\tau_{xx}) + \frac{\partial}{\partial y}(\tau_{yx}) + \frac{\partial}{\partial z}(\tau_{zx}) \tag{A.5}$$

$$\frac{d\vec{F}_y}{dV} = -\frac{\partial P}{\partial y} + \frac{\partial}{\partial x}(\tau_{xy}) + \frac{\partial}{\partial y}(\tau_{yy}) + \frac{\partial}{\partial z}(\tau_{zy}) \tag{A.6}$$

$$\frac{d\vec{F}_z}{dV} = -\frac{\partial P}{\partial z} + \frac{\partial}{\partial x}(\tau_{xz}) + \frac{\partial}{\partial y}(\tau_{yz}) + \frac{\partial}{\partial z}(\tau_{zz}) \tag{A.7}$$

Here the net force $\vec{F} = \vec{F}_x + \vec{F}_y + \vec{F}_z$ is written in terms of the pressures and the viscous forces acting on the control volume. Body forces (gravity) have been neglected as they are not important in this work. The viscous forces are expressed in terms of the viscous force tensor τ_{ij}. Sir George G. Stokes (1819-1903) and C.L.M.H. Navier (1785-1836) proposed the following relationship between the viscous stresses and the viscosity based on the definition of Newtonian fluids where the viscous stress is proportional to the viscosity μ and the velocity gradient $\frac{\partial u}{\partial y}$:

$$\tau_{xx} = 2\mu\frac{\partial u}{\partial x} \qquad \tau_{yy} = 2\mu\frac{\partial v}{\partial y} \qquad \tau_{zz} = 2\mu\frac{\partial w}{\partial z} \tag{A.8}$$

$$\tau_{xy} = \tau_{yx} = \mu\left(\frac{\partial u}{\partial y} + \frac{\partial v}{\partial x}\right) \tag{A.9}$$

$$\tau_{xz} = \tau_{zx} = \mu\left(\frac{\partial w}{\partial x} + \frac{\partial u}{\partial z}\right) \tag{A.10}$$

$$\tau_{yz} = \tau_{zy} = \mu\left(\frac{\partial v}{\partial z} + \frac{\partial w}{\partial y}\right) \tag{A.11}$$

In the case where compressibility is significant, additional terms should be included in eq (A.9) which contain a volume expansion rate and a second coefficient of viscosity [34]. They are not included here as this work deals only with weakly compressible flow where the mach number is less than 0.1 [32]. The viscous stresses can be written in terms of the stress tensor τ_{ij} where the first subscript i indicates the axis which the face on which the stress acts is perpendicular to and the second subscript j indicates the direction the stress acts in on the face. The stress τ_{xy} acts on a face perpendicular to the x axis and is oriented in the y direction. The full three dimensional stress tensor is given as:

$$\tau_{ij} = \begin{pmatrix} \tau_{xx} & \tau_{xy} & \tau_{xz} \\ \tau_{yx} & \tau_{yy} & \tau_{yz} \\ \tau_{zx} & \tau_{zy} & \tau_{zz} \end{pmatrix} \tag{A.12}$$

Combining the constitutive relations for the viscous stresses with the force equations (Newton's Second Law), the Navier-Stokes equations are ([33]):

$$\begin{aligned} \rho\frac{Du}{Dt} = \frac{\partial P}{\partial x} + \frac{\partial}{\partial x}\left[\mu_l\left(2\frac{\partial u}{\partial x} - \frac{2}{3}\nabla\cdot\vec{U}\right)\right] + \\ + \frac{\partial}{\partial y}\left[\mu_l\left(\frac{\partial u}{\partial y} + \frac{\partial v}{\partial x}\right)\right] + \frac{\partial}{\partial z}\left[\mu_l\left(\frac{\partial w}{\partial x} + \frac{\partial u}{\partial z}\right)\right] \end{aligned} \tag{A.13}$$

$$\begin{aligned} \rho\frac{Dv}{Dt} = \frac{\partial P}{\partial y} + \frac{\partial}{\partial y}\left[\mu_l\left(2\frac{\partial v}{\partial z} - \frac{2}{3}\nabla\cdot\vec{U}\right)\right] + \\ + \frac{\partial}{\partial z}\left[\mu_l\left(\frac{\partial v}{\partial z} + \frac{\partial w}{\partial y}\right)\right] + \frac{\partial}{\partial x}\left[\mu_l\left(\frac{\partial u}{\partial y} + \frac{\partial v}{\partial x}\right)\right] \end{aligned} \tag{A.14}$$

$$\begin{aligned}\rho\frac{Dw}{Dt} = \frac{\partial P}{\partial z} + \frac{\partial}{\partial z}\left[\mu_l\left(2\frac{\partial w}{\partial z} - \frac{2}{3}\nabla\cdot\vec{U}\right)\right] + \\ + \frac{\partial}{\partial x}\left[\mu_l\left(\frac{\partial w}{\partial x} + \frac{\partial u}{\partial z}\right)\right] + \frac{\partial}{\partial y}\left[\mu_l\left(\frac{\partial v}{\partial z} + \frac{\partial w}{\partial y}\right)\right]\end{aligned} \tag{A.15}$$

The Navier Stokes equations are a formulation of Newton's second law for fluids where the shear stress in linearly proportional to the strain rate; the constant of proportionality is the laminar viscosity μ. The left hand side represents the mass and acceleration terms ($m\vec{a}$) for the x, y and z directions respectively. The right hand side represents the forces acting on the infinitesimal control volume. These are forces due to pressure and forces due to viscous shear stresses. This is the pure form of the NS equations which applies to unsteady, compressible flows with isotropic properties. Using tensor notation, where repeated subscripts i, j or k imply summation over all values of the repeated subscript, the NS equations can be written in compact form:

$$\rho\frac{Du_i}{Dt} = \frac{\partial P}{\partial x_i} + \frac{\partial}{\partial x_j}\left\{\mu\left(\frac{\partial u_i}{\partial x_j} + \frac{\partial u_j}{\partial x_i} - \frac{2}{3}\delta_{ij}\frac{\partial u_k}{\partial x_k}\right)\right\} \qquad (i,j,k = 1,2,3) \tag{A.16}$$

A.2 Spalart Allmaras Model

The Spalart Allmaras (SA) one equation model solves the Reynolds averaged Navier-Stokes equations, the continuity equation and an additional transport equation for the eddy viscosity. The model is defined [21]:

Reynolds Stress:

$$-\overline{u_i u_j} = 2\nu_t S_{ij}, \qquad S_{ij} = \frac{1}{2}\left(\frac{\partial U_i}{\partial x_j} + \frac{\partial U_j}{\partial x_i}\right) \tag{A.17}$$

Eddy Viscosity:

$$\nu_t = \tilde{\nu} f_{v1}, \qquad f_{v1} = \frac{\chi^3}{\chi^3 + C_{v1}^3}, \qquad \chi \equiv \frac{\tilde{\nu}}{\nu} \tag{A.18}$$

$\tilde{\nu}$ is the working variable in the eddy viscosity transport equation:

$$\begin{aligned} \frac{D\tilde{\nu}}{Dt} &= C_{b1}\left[1 - f_{t2}\right]\tilde{S}\tilde{\nu} + \\ &\quad + \frac{1}{\sigma}\left[\nabla \cdot \left(\left(\nu + \tilde{\nu}\right)\nabla\tilde{\nu}\right) + C_{b2}\left(\nabla\tilde{\nu}\right)^2\right] + \\ &\quad - \left[C_{w1} f_w - \frac{C_{b1}}{\kappa^2} f_{t2}\right]\left[\frac{\tilde{\nu}}{d}\right]^2 + f_{t1}\Delta U^2 \end{aligned} \tag{A.19}$$

S is the vorticity magnitude and d is the distance to the closest wall:

$$\tilde{S} \equiv S = \frac{\tilde{\nu}}{\kappa^2 d^2} f_{v2}, \qquad f_{v2} = 1 - \frac{\chi}{1 + \chi f_{v1}} \tag{A.20}$$

$$f_w = g\left[\frac{1 + C_{w3}^6}{g^6 + C_{w3}^6}\right]^{\frac{1}{6}} \tag{A.21}$$

$$g = r + C_{w2}\left(r^6 - r\right), \qquad r \equiv \frac{\tilde{\nu}}{\tilde{S}\kappa^2 d^2} \tag{A.22}$$

$$f_{t2} = C_{t3}\exp\left(-C_{t4}\chi^2\right) \tag{A.23}$$

constant	value	constant	value
C_{b1}	0.1355	C_{w3}	2
σ	2/3	C_{v1}	7.1
C_{b2}	0.622	C_{t1}	1
κ	0.41	C_{t2}	2
C_{w1}	$C_{b1}/\kappa^2 + (1 + C_{b2})/\sigma$	C_{t3}	1.1
C_{w2}	0.3	C_{t4}	2

Table A.1: Definition of Constants used in Spalart Allmaras Model Equations

$$f_{t1} = C_{t1}\ g_t \exp\left(-C_{t2}\frac{\omega_t^2}{\Delta U^2}\left[d^2 + G_t^2 d_t^2\right]\right), \qquad g_t \equiv \min\left(0.1, \frac{\Delta U}{\omega_t \Delta x}\right) \tag{A.24}$$

f_{t1} is a trip function where d_t is the distance from a field point to the trip which is on the wall; ω_t is the wall vorticity at the trip, ΔU is the difference in velocity between field point and the trip point on the wall. Δx is the grid spacing tangential to the wall at the trip point. The constants in the model are define in Table A.1.

A.3 Speziale $k - \tau$ Model

The Speziale/Abid/Anderson $k - \tau$ two equation model solves the Reynolds averaged Navier-Stokes equations, the continuity equation and two additional transport equations for the turbulent kinetic energy k and the turbulent time scale $\tau \equiv k/\epsilon$ [22]:

$$\tau_{ij} = -\frac{2}{3}k\delta + \nu_t\left(\frac{\partial \overline{u}_i}{\partial x_i} + \frac{\partial \overline{u}_j}{\partial x_i}\right) \tag{A.25}$$

$$\nu_t = C_\mu f_\mu k\tau \tag{A.26}$$

$$\frac{Dk}{Dt} = \tau_{ij}\frac{\partial \overline{u}_i}{\partial x_j} - \frac{k}{\tau} + \frac{\partial}{\partial x_i}\left[\left(\nu + \frac{\nu_t}{\sigma_k}\right)\frac{\partial k}{\partial x_i}\right] \tag{A.27}$$

$$\begin{aligned}\frac{D\tau}{Dt} = {} & (1 - C_{\epsilon 1})\frac{\tau}{k}\tau_{ij}\frac{\partial \overline{u}_i}{\partial x_j} + (C_{\epsilon 2} f_2 - 1) + \\ & + \frac{2}{k}\left(\nu + \frac{\nu_t}{\sigma_{\tau 1}}\right)\frac{\partial k}{\partial x_i}\frac{\partial \tau}{\partial x_i} - \frac{2}{\tau}\left(\nu + \frac{\nu_t}{\sigma_{\tau 2}}\right)\frac{\partial \tau}{\partial x_i}\frac{\partial \tau}{\partial x_i} + \\ & + \frac{\partial}{\partial x_i}\left[\left(\nu + \frac{\nu_t}{\sigma_{\tau 2}}\right)\frac{\partial \tau}{\partial x_i}\right]\end{aligned} \tag{A.28}$$

where

$$C_{\epsilon 2} = 1.83\left[1 - (2/9)\exp\left(-Re_t^2/36\right)\right] \tag{A.29}$$

$$f_2 = \left[1 - \exp\left(-y^+/A_2\right)\right]^2 \tag{A.30}$$

$$f_\nu = \left(1 + 3.45/\sqrt{Re_t}\right)\tanh(y^+/70) \tag{A.31}$$

$Re_t \equiv k^2/\nu\epsilon$ is the turbulence Reynolds number based on the turbulent kinetic energy k, the laminar viscosity ν and the dissipation ϵ.

The constants are set as $C_{\epsilon 1} = 1.44$, $A_2 = 4.9$, $C_\mu = 0.09$ and $\sigma_K = \sigma_{\tau 1} = \sigma_{\tau_2} = 1.36$.

A.4 Adaptive $k - \tau$ Model

The Adaptive $k - \tau$ model is a hybrid model that reduces to a standard two equation model in the limit of coarse grids in steady simulations and approaches a DNS in the limit of very fine grids in unsteady simulations. In addition to the standard two equation model transport equations, transport equations for the unresolved turbulent kinetic energy k' and the unresolved turbulent time scale τ' are used:

$$\frac{\partial(\rho k')}{\partial t} + \frac{\partial(\rho u_i k')}{\partial x_i} = \frac{\partial}{\partial x_i}\left((\mu + \mu_k)\frac{\partial k'}{\partial x_i}\right) + P_k - \rho\frac{k'\left(1 + \frac{\tau'\sqrt{k'}}{L_\Delta}\right)}{\tau'} \tag{A.32}$$

$$\begin{aligned} \frac{\partial(\rho\tau')}{\partial t} + \frac{\partial(\rho u_i\tau')}{\partial t} = {} & \frac{\partial}{\partial x_i}\left((\mu + \mu_\tau)\frac{\partial \tau'}{\partial x_i}\right) + (1 - C_{\varepsilon 1}) \cdot \frac{\tau'}{k'}P_k + \\ & + \rho\left[C_{\varepsilon 2} - \left(1 + \frac{\tau'\sqrt{k'}}{L_\Delta}\right)\right] + \\ & + \frac{2}{k'}(\mu + \mu_\tau)\frac{\partial k'}{\partial x_i}\frac{\partial \tau'}{\partial x_i} - \frac{2}{\tau'}(\mu + \mu_\tau)\frac{\partial \tau'}{\partial x_i}\frac{\partial \tau'}{\partial x_i} + \\ & - 0.06 \cdot S \cdot \tau'^3\left(\frac{\partial^2 u_i}{\partial x_k \partial x_j}\right)^2 \end{aligned} \tag{A.33}$$

The eddy viscosity μ_t is defined as:

$$\mu_t = \rho \cdot C_\mu \cdot f_\mu \cdot k' \cdot \tau' \tag{A.34}$$

Where

$$C_\nu = \frac{0.3}{1+0.35\cdot S^{3/2}}\left[1-\exp\left(-\frac{0.36}{\exp(-0.75\cdot S)}\right)\right] \tag{A.35}$$

$$P_k = -\rho\overline{u_i'u_j'}\frac{\partial u_i}{\partial x_j} \qquad S = \tau'\sqrt{\frac{S_{ij}S_{ij}}{2}} \tag{A.36}$$

$$S_{ij} = \frac{\partial u_i}{\partial x_j} + \frac{\partial u_j}{\partial x_i} - \frac{2}{3}\frac{\partial u_i}{\partial x_i}\delta_{ij} \tag{A.37}$$

$$\Omega_{ij} = \frac{\partial u_i}{\partial x_j} - \frac{\partial u_j}{\partial x_i} \tag{A.38}$$

$$C_{\epsilon 2} = 1.92(1-0.3\mathrm{exp}(-Re_t^2)), \qquad Re_t \equiv \frac{k^2}{\nu\epsilon} \tag{A.39}$$

$$f_\nu = 1-\exp\left[-\left(\frac{Re_t}{90}\right)^{1/2} - \left(\frac{Re_t}{400}\right)^2\right] \tag{A.40}$$

The Reynolds stresses are calculated as shown is equation (A.41) with constants defined in Table A.2.

C_ν	$C_{\epsilon 1}$	C_1	C_2	C_3	C_4	C_5	C_6	C_7
0.09	1.44	-0.1	0.1	0.26	-0.081	0	0.0405	-0.0405

Table A.2: Definition of Constants used in Adaptive $k - \tau$ Model Equations

$$\begin{aligned}
-\rho\overline{u_i'u_j'} \;=\; & \mu_t \cdot S_{ij} - \frac{2}{3}k'\delta_{ij} - C_1\mu_t\tau' \cdot \left(S_{ik}S_{kj} - \frac{1}{3}S_{kl}S_{kl}\delta_{ij}\right) + \\
& - C_2\mu_t\tau'(\Omega_{lk}S_{kj} + \Omega_{jk}S_{kj}) - C_3\mu_t\tau'\left(\Omega_{lk}\Omega_{jk} - \frac{1}{3}\Omega_{kl}\Omega_{kl}\delta_{ij}\right) + \\
& + C_\mu\nu_t\tau'^2 \cdot \left\{C_4\left[S_{kl}\Omega_{lj} + S_{kj}\Omega_{li} - \frac{2}{3}S_{km}\Omega_{lm}\delta_{ij}\right] \cdot S_{kl} + \right. \qquad \text{(A.41)} \\
& + C_5\left[S_{ik}S_{jl} - \frac{1}{3}S_{mk}S_{ml}\delta_{ij}\right]S_{kl} + \\
& \left. + C_6 S_{ij}S_{kl}S_{kl} + C_7 S_{ij}\Omega_{kl}\Omega_{kl}\right\}
\end{aligned}$$

Appendix B

Eddy Viscosity Study

α	$\frac{\mu_t}{\mu}$	C_l	C_d	C_{df}	C_{dp}
0°	10	0.00056	0.00430	0.00086	0.00344
	1	0.00053	0.00349	0.00162	0.00187
	10^{-1}	0.00060	0.00423	0.00174	0.00249
	10^{-2}	0.00051	0.00464	0.00162	0.00302
	10^{-3}	0.00048	0.00476	0.00161	0.00314
	10^{-4}	0.00049	0.00475	0.00161	0.00314
	10^{-5}	0.00052	0.00475	0.00161	0.00314
	10^{-6}	0.00043	0.00475	0.00161	0.00314
	10^{-7}	0.00056	0.00476	0.00161	0.00315
4°	10	0.414	0.00613	0.00081	0.00532
	1	0.443	0.00458	0.00152	0.00306
	10^{-1}	0.430	0.00556	0.00156	0.00400
	10^{-2}	0.422	0.00631	0.00146	0.00484
	10^{-3}	0.421	0.00642	0.00146	0.00496
	10^{-4}	0.421	0.00642	0.00146	0.00496
	10^{-5}	0.421	0.00643	0.00146	0.00497
	10^{-6}	0.421	0.00643	0.00146	0.00497
	10^{-7}	0.421	0.00643	0.00146	0.00497

Table B.1: NACA 0012 Grid airfoil32 Spalart Allmaras Model: Variation of Lift and Drag with Eddy Viscosity Ratio for $Re_c = 3 \times 10^6$

α	$\frac{\mu_t}{\mu}$	C_l	C_d	C_{df}	C_{dp}
0°	1	0.00014	0.00575	0.00347	0.00228
	10^{-1}	0.00017	0.00561	0.00344	0.00218
	10^{-2}	OSC	OSC		
	10^{-3}	OSC	OSC		
	10^{-7}	OSC	OSC		
4°	1	0.435	0.00681	0.00339	0.00343
	10^{-1}	0.439	0.00678	0.00334	0.00344
	10^{-2}	OSC	OSC		
	10^{-3}	OSC	OSC		
	10^{-7}	OSC	OSC		

Table B.2: NACA 0012 Grid airfoil32 Speziale $K-\tau$ Model: Variation of Lift and Drag with Eddy Viscosity Ratio for $Re_c = 3 \times 10^6$